KINEMATIC STUDIES OF EXTENDED ASTRONOMICAL OBJECTS

A thesis
submitted to the M. S. University of Baroda
for the degree of Doctor of Philosophy in Physics

P.Seema
Physical Research Laboratory
Ahmedabad 380009
India

JULY 1994

VELOCITY FIELDS IN HII REGIONS USING HIGH RESOLUTION IMAGING FABRY-PÉROT SPECTROMETER

CERTIFICATE

I Declare that the works presented in this thesis are original and has not formed the basis for the award of any degree or diploma by any University or Institution.

P. Seema

P.Seema
(Author)

Certified by

Prof.B.G.Anandarao
(Guide)
Physical Research Laboratory,
Ahmedabad, India.

Dr. M. S. Shah
(Co Guide)
Department of Physics
M. S. University of Baroda
Baroda, India.

To see a world in a grain of sand,
And heaven in a wild flower:
Hold infinity in the palm of your hand,
And eternity in an hour.
-Blake

Dedicated to my beloved mother
Bhaiyya, Abhaya, Vikas
&
in profound memory of my father

ACKNOWLEDGEMENTS

I take this opportunity to thank all the people who have directly or indirectly contributed to my thesis.

First of all, I express my sincere thanks to Prof. B.G.Anandarao under whose guidance this thesis work has been carried out. It was his ever encouraging attitude and patience that kept me going on at each stage. I have learnt a lot from his vast experience and depth of knowledge. I always admired his ability to express things in a simple form. His sincerety and dedication for work has always been a source of inspiration for me. I am indebted to him for his personnal kindness to me at every stage and the moral support specially at the last stages of the thesis.

I am profoundly thankful to Dr.(Miss) Madhuben Shah who has helped me in different phases of my thesis work.

It has been a valuable experience to be associated with Prof. J.N.Desai. I am grateful for his fruitful comments and suggestions during my assesment reviews. I thank Prof. M.R.Despande for various discussions.

I thank Prof's. R.K.Varma, R.Raghavarao and B.H.Subbaraya for showing interest in my work.

I accord my gratitude to Dr.U.C.Joshi for taking personnel interest in my work and making useful suggestions. It is a pleasure to acknowledge Dr. T.Chandrasekhar and Dr. N.M.Ashok for always been kind and helpful.

I am grateful to Dr.D.P.K.Banerjee for the innumerable discussions I had with him. I express my sincere thanks to him for his help during the observational work of the thesis and also for critically going through the manuscript and making useful suggestions.

I am grateful to Dr.Shishir Deshpande for his enthusiastic help in solving computational problems. I thank Dr.Harish Chandra, Dr.H.O. Vats and Dr.Shyamlal for their help and interest in my work.

I have no words to thank Sam Ragland for not only being the nice person he has always been, but streching his help at every stage. I specially thank him for his invaluable help and all the moral support during the last stages of my thesis work. It will be a memorable experience to have been associated with him.

I had always been benefited by Dr. Sai Iyer's expertise in computer soft-

wares and thank him for being kind enough to make his PC available during the final stages of the work.

I acknowledge Mr. H.I.Pandya's computational assistance during the development of the softwares for the data analysis with full enthusiam and cooperation. I also thank Mrs. S.K.Jani and Mr. A.H.Desai for their kind help. I express my thanks to the electronics & engineering staff of the infrared group. Mr.N.S.Jog., Mr.R.T.Patel , Mr. K.S.B.Manian, Mr. F.M.Pathan and Mr.R.K.Mahadkar need special mention. I thank Mr. V.C.Mathews and Mrs. Karanjgaonkar for typographical help.

I am personnally grateful to the PRL workshop and in particular Mr.P.S. Panchal, Mr. J.A. Panchal and Mr.A. Panchal for their sincere efforts and devotion in the fabrication of the mechanical components of Imaging Fabry-Perot spectrometer. I am grateful to the computer center staff and library staff for their cooperation. I thank Mr. D.R.Ranpura of photographic section for the prompt delivery of the photographic prints as and when required.

I express my thanks to Mr.Poulose for his kind help in typing some part of the thesis. I thank my collegues Abhijeet Chakraborty, Watson, and Muttu Mariappan for their help and cooperation. I am grateful to Venkataramani for the innumerable help provided by him at different stages.

My all the friends at PRL hostel need to be thanked for keeping me cheerful with their company. The association and friendship with Supriyo Chakarborty, Krishan, Gurubaran, Ganguly, Nandita Srivastava, Subrat Sarangi, Jerri, Pallamraju, Prahlad, Manoj, Debashish Majumdar, Himadri, Varun, Tarun, Somesh, Ramachandran, Lambodar mishra, Sushma, Mitakshi, Anshu, Shikha, Manish Naja, Gopal,Gautam, Prabir Patro, Biswa, Santanam, will ever be memorable. I would like to thank Kamesh & family, Dr.Haider & family for their warm hospitality.

I acknowledge the affection and care given to me by my friends Guruprasad and Nishta.

It is the moral support and encouragement of my mother and brothers that kept me going on. I thank my bhabhi for her encouraging letters during the hard times.

Finally, I thank with love my husband, Mac (Dr.S.M.Ahmed), who has been an ideal and source of inspiration for me throughout. Being in the same field gave me an opportunity to discuss and learn a lot from him. It was he , who was always there to share my moments of agony and I owe my gratitude to him for the successful completion of the thesis.

STATEMENT

The work contained in this thesis has been carried out at the Physical Research Laboratory, Ahmedabad under the guidance of Prof.B.G.Anandarao. The work done for the thesis consists of two aspects: (i) instrumentation and (ii) Observations of HII regions and their interpretation. The Imaging Fabry Pérot spectrometer (IFPS) has been designed and built at PRL. A major part of the funds for this work was granted by the DST. The observations of the two HII regions for the thesis work have been made at Gurushikhar observatory, Mt Abu. The thesis is divided into six chapters.

Chapter I contains an overview of HII regions. The introduction, evolution and definition of important physical parameters is discussed. The significance of kinematic studies of the HII regions and the aim and the scope of the present studies are stated in this chapter.

Chapter II is concentrated on the details of the instrument developed to carry out the present work. The author describes here, the design, fabrication and performance of high resolution piezo-scanned Imaging Fabry-Perot Spectrometer and the reasoning for the selection of the present instrument. A brief description of Fabry-Pérot Spectrometer is given. This chapter also provides a brief introduction to different types of detectors used for astronomical observations discussing their merits and demerits. A comparison of their characteristic properties is also given.

Chapter III gives the details of the observations made and the method of analysis. Data reduction softwares developed for the extraction of the kinematic information are discussed here. An estimate of the errors involved in observations and data analysis is given.

Chapter IV presents the kinemaics of the nearest HII region, the Orion nebula and the results obtained from the present analysis. The importance of the new results obtained is discussed and comparison with earlier results is made. Velocity field across the important features *viz bar* ionization front, dark *bay* and the molecular cloud regions is detailed. Velocity field structure across the bar ionization front is obtained for the first time. Certain high veocity flows are found across the nebula, which seem to be new and do not correspond to any of the earlier detected peculiar objects like knots, jets and HH objects. A jet like feature about 1.5 arc min north-west of the trapezium stars is found. Possible interpretation is given for the existence of such features. Iso-velocity contour map is generated and a comparison is made with maps at infrared and radio wavelenghts. A synthetic profile is generated at a particular position on the nebula and compared with the observed profile.

In chapter V, studies on another HII region Trifid Nebula are discussed. This provides complimentary studies to those on Orion nebula in order to check the proposed models on HII regions. An iso-velocity contour map is generated for Trifid nebula. A jet like feature arc min SE of the ionizing star is observed.

Chapter VI is the concluding chapter which summarizes the important results obtained from the present analysis and scope for future studies.

Contents

Chapter 1

AN INTRODUCTION TO HII REGIONS

In astrophysics we come across mainly two types of gaseous nebulae: the planetary nebulae and the HII regions or diffuse nebulae. Diffuse nebulae are relatively irregular and large objects of gas and dust surrounding groups of hot, early type stars. Usually these are associated with regions of recent star formation. In the case of the planetary nebulae, which represent late stages of evolution of intermediate mass stars, one finds at least some sort of symmetrical morphology-spherical or axial. Also these are smaller in extent and the central ionizing sources are hot cores of evolved stars. Here in this thesis we deal with the diffuse nebulae or HII regions associated with star formation complexes in our galaxy.

Observations on these gaseous nebulae date back to medieval period. *Stella nebulosa* was the name given to the first observed six, hazy, luminous

spots on the celestial sphere in Ptolemy's *Almagest.* When viewed through a telescope, these were resolved into star clusters. As the efforts of observations continued, other nebulous objects were discovered. The first gaseous nebula to be discovered was in the constellation of *Orion* by Fabri de Peiresc in the year 1610 AD. Much later during the 18^{th} century, the French astronomer Charles Messier complied a list of 105 nebulous objects- some of which are now known to be external galaxies while the others are either gaseous nebulae or star clusters. Various catalogues published subsequently- the New General Catalogue and the Index catalogue- listed more than 13000 nebulous objects. With the advent of powerful optical telescopes aided with photography, by the turn of this century the spiral nebulae or 'island universes' were found to be a separate class of objects outside our own galaxy (thanks to the Shapley-Curtis debate in 1929). Among the galactic nebulae, those having well-defined disk-like shapes are identified as planetary nebulae and those with irregular shapes and which are found close to the galactic plane are identified as HII regions.

Edwin Hubble made a spectroscopic study of luminous diffuse nebulae in 1922 and found that they ranged from those which show only bright emission lines to those which show only continuum emission. Further, Hubble found that the emission line nebulae are associated with O to B0 type stars while the continuum nebulae, known as reflection nebulae, are just reflecting or scattering the light from cooler stars having insufficient energy to ionize the gas. Thus it was clear that the nature of the nebular emission is determined

by the embedded star(s).

In this chapter, we give an overview of various processes prevalent in HII regions and discuss the motivation for the present work.

1.1 Definition of an HII Region

An HII region is essentially an ionized region surrounding a hot (T = a few $\times 10^4$°K) star. The formation of an ionized region is initiated when a neutral cloud condenses under the influence of gravitational force resulting in the formation of stars. As soon as a massive O or early B type star forms and approaches the main sequence, its ultraviolet radiation ionizes the surrounding cloud resulting in the formation of an HII region. Because of the large abundance of hydrogen in the interstellar medium, the ionized diffuse nebulae came to be known as HII regions. They account for about 10% of the total interstellar gas. They occur in varying sizes, but generally they are found to be of the order of a few parsecs. The temperatures in the HII regions are found to be about 10^4°K which is two orders of magnitudes greater than that of the surrounding neutral regions or HI regions. Typical electron densities of the ionized part of the nebula range from 10^2 to 10^4 cm^{-3}. The HII regions are fairly homogeneous on a global scale. However, locally, there are certain knots, neutral condensations and bright rims observed throughout the ionized region. The masses of the HII regions are found to be of the order of 10^2 to $10^4 M_\odot$, where $M_\odot$ is the mass of the sun. Internal motions in the

gas are found to be of the order of 10 km/s (Osterbrock, 1974).

The nearly spherical region of ionized material surrounding the 'hot star' is termed as *Strömgren* sphere after Bent Strömgren who was the first to show in 1939 that there exists a definite boundary between HI and HII regions. The cloud cannot be ionized indefinitely due to the recombination of ions and electrons taking place continuously within the ionized region and the inverse-square effect of the geometric dilution ($W = R^2/4S^2$, where W is the dilution; R, the radius of and S the distance from the star). The thickness of the boundary is roughly equal to the mean free path of the ionizing radiation $\lambda_i \sim (N_H \alpha)^{-1}$; where N_H is the number density of atomic hydrogen and α is its photoionization cross section. It is found that the mean free path λ_i is very small (($\approx 10^{-2}$ pc, (Osterbrock, 1974)) compared to the distance from the center of the ionizing star and therefore beyond the resolving limit of the largest earth-based telescopes. Therefore the HI-HII interface is considered as a discontinuity (Kaplan, 1966). Some of the important parameters which signify HII regions are discussed in the following sections:

1.2 Strömgren radius

The radius of the Strömgren sphere is determined by equating the number of Lyman continuum photons (with $\lambda < 912$ Å) emitted by a star in one second to the number of recombinations into hydrogen atoms. Assuming that each of the former produces an electron and ion pair, and all of them

are absorbed in the HII region, we can write,

$$4\pi R_*^2 N_{LC} = \frac{4}{3}\pi r_o^3 n_e n_p \alpha(T) \tag{1.1}$$

where n_e, n_p are the number of electrons and protons respectively per unit volume, R_* is the radius of the star, N_{LC}, the number of Lyman quanta emitted per square centimetre of surface of the ionizing star and $\alpha(T)$, the recombination coefficient to all states of the hydrogen atom. From this eqation, the Strömgren radius r is given as:

$$r_o = \left[\frac{3R_*^2 N_{LC}}{n_e n_p \alpha(T)}\right]^{\frac{1}{3}} \tag{1.2}$$

One can infer from this equation that for a given star, the radius of an HII region is larger, the lesser the density is. Furthermore, the radius decreases as the temperature of the star decreases (i.e., for the stars of later spectral types) because the factor N_{LC} decreases. Strömgren radius for different spectral types is given in Table 1.1 (adapted from Mathews and O'Dell, 1969). In the foregoing treatment we have assumed that the collisional ionization is negligible (electron impact). The different parameters in the table are defined as follows: T_* is the star temperature, L_e is the star luminosity, T_2 is the temperature in the HII region, R_{si} is the radius of the 'initial' and R_{sf} the radius of the 'final' Strömgren sphere, t_{si} and t_{sf} are the times required for sound to cross the initial and final Strömgren spheres respectively.

Table 1.1: Properties of Central Stars and Strömgren Spheres

$M/M_\odot$	T_* K	$L_e/10^5 L_\odot$	t_{on} 10^4 yr	t_{form} 10^4 yr	T_2 K	R_{si} pc	t_{si} 10^4 yr	R_{sf} pc	t_{sf} 10^4 yr
30	42000	1.320	02.2	4.2	7700	13.0	85	370	25.0
						0.60	3.9	17	1.1
20	35100	0.501	02.8	6.2	7400	8.5	56	238	16.0
						0.39	2.6	11	0.75
11	27400	0.095	05.8	12.6	7000	4.0	27	110	7.7
						0.18	1.2	4.8	0.34
6	20200	0.014	15.7	35.5	6500	1.7	24	44	3.2
						0.08	0.57	2.0	0.15

Note: In the last four columns, upper value for $n_e = 10\ cm^{-3}$; lower values for $n_e = 10^3 cm^{-3}$.

1.3 Emission Measure

The optical emission lines are some of the most observable physical attributes in the HII regions. The intensity of the hydrogen emission lines depends upon the number of excited atoms or on the number of recombinations which is equal to $n_e n_p = n_e^2$ when $\alpha(T)$ is held constant for a given stellar temperature. Therefore, the intensity of radiation is determined (Kaplan, 1966) by the integral, called emission measure (ME), of $n_e n_p$ along the line of sight written as follows,

$$ME = \int_0^{2r_o} n_e n_p dr \approx 2 r_o n_e^2 \ (pc/cm^6) \tag{1.3}$$

In the case of the collisionally excited forbidden lines from ions of oxygen or nitrogen, for instance, the rate of energy emission is proportional to the rate of collisions or to the product of the number densities of electrons and ions in question. The number density n is proportional to n_e if the abundance of the element and its state of ionization is fixed; thus, the intensity of forbidden lines is also proportional to the emission measure. Thus whether the given HII region is observable or not depends on its emission measure and of course on the sensitivity of the instrument. For Orion nebula, the nearest of all the HII regions, the ME is $\sim 10^7 pc/cm^6$.

Table 1.2: Ionization Potential of certain ions prominent in HII region

Atom	Stage of Ionization		
	I (eV)	II (eV)	III (eV)
H	13.598		
C	11.260	24.383	47.887
N	14.534	29.601	47.448
O	13.618	35.11	54.934
S	10.360	23.3	34.83

1.4 Stratification of ionization

Kaler (1967) has shown that there exists a significant velocity stratification along the line of sight in the case of the nearby HII region, the Orion nebula. Singly ionized ions such as S^+, Fe^+, having low ionization potentials (Table 1.2) have low negative velocities with respect to the Trapezium stars whereas there is a sharp change in velocities of ions requiring conditions of higher excitation such as S^{+++}, O^{++} and Ne^{++}. The ions N^+ and O^+ are found at intermediate velocities.

1.5 Ionization processes in HII regions

It is important to know the ionization processes taking place in the interstellar medium. The central star(s) provides a copious source of energetic

ultraviolet photons by which neutral atoms can get ionized. Besides this photoionization process, it is also possible that collisional ionization plays a significant role. Specially in regions where high velocity jets and shock fronts are found the gas undergoes compression and it is likely that collisions contribute to ionization. It is important to know how far out the photon flux from the star can reach the surrounding medium and what are the other factors contributing to ionization farther out.

1. Photoionization: It is one of the main ionization mechanisms in which the ultraviolet radiation from the exciting star (with threshold wavelength $\lambda < 912$ Å) ionize the diffuse cloud. There is an ionization equilibrium maintained throughout the nebula by a balance between photoionization and recombination of electrons with ions. The ionization equilibrium equation for any two successive stages of ionization i and $i+1$ of any element X may be written as (Osterbrock, 1974)

$$N\left(X^{+i+1}\right) \int_{\nu_i}^{\infty} \frac{4\pi J_\nu}{h\nu} a_\nu(x^{+i}) d\nu = N\left(x^{+i}\right) n_e \, \alpha_G\left(x^{+i+1}, T\right) \qquad (1.4)$$

where $n\left(x^{+i}\right)$ and $n\left(x^{+i+1}\right)$ are the number densities of the two successive stages of ionization; $a_\nu(x^{+i})$ is the photoionization cross section from the ground level of x^i with the threshold ν_i; and $\alpha_G\left(x^{+i+1}, T\right)$ is the recombination coefficient of the ground level of x^{+i+1}, to all levels of x^{+i}.

The equation of transfer for radiation with frequency $\nu > \nu_o$ is given as

$$\frac{dI_\nu}{ds} = -N_{H_o}\, a_\nu\, I_\nu + J_\nu. \tag{1.5}$$

where I_ν is the specific intensity of radiation and J_ν is the local emission coefficient (in energy units per unit volume per unit time per unit solid angle per unit frequency) for ionizing radiation.

2. Collisional Ionization: In the outer regions of the HII regions, there are very few stellar ultra-violet photons left that are capable of ionizing the hydrogen atoms as most of them get absorbed inside the HII region itself. However, hydrogen atom can still be ionized in these regions by collisions with energetic particles of various types, e.g., electrons and protons. Ionization by energetic thermal electrons is important at temperatures of about 10^4°K. Cosmic ray protons ($\epsilon \sim$ a few million eV) and x-rays ($\epsilon \sim$ 200 eV) can also penetrate diffuse clouds and ionize the hydrogen atoms there.

   Ionization by collisions becomes important even for heavier atoms when the temperature is greater than 10^4°K. The high random velocities result in dissociation of molecules and hence reactions of ions with molecules can be neglected. The fraction of atoms in different charge states becomes independent of electron density n_e. Therefore, values of ionization fraction can be computed (Spitzer, 1972) for different atoms, e.g., O, N at temperatures between 10^5-10^6°K.

3. Charge exchange reactions: It is another important atomic process which determines the ionization equilibrium of certain light elements particularly at the outer boundaries of the nebulae and in HI regions. For example, let us consider an ionization process (Osterbrock, 1974) in the case of neutral oxygen, having a charge exchange reaction with a proton,

$$O^o\,(^3P) \;+\; H^+ \;\rightarrow\; O^+\,(^4S) \;+\; H^o\,(^2S)\;, \tag{1.6}$$

and the inverse reaction

$$O^+\,(^4S) \;+\; H^o\,(^2S) \;\rightarrow\; O^o\,(^3P) \;+\; H^+\;. \tag{1.7}$$

Charge exchange process dominates at the outer edge of the nebula because of the high density of H^o.

1.6 Evolution of HII region

When a hot star(of luminosity L $\sim 10^{38}$ ergs sec^{-1}) is switched on inside a neutral cloud of low density, a radiation wave called *ionization front* moves radially outwards, ionizing the material in a radius given by the eqn. 1.2. In the beginning of this process, the pressure inside the HII region becomes greater than that of the surrounding HI region resulting in the expansion of the ionized material outwards compressing the neutral gas ahead. However, since the velocity in the neutral gas is small ($\sim$ 1 km/s) compared to that of the expanding ionized gas ($\sim$ 13 km/s), the pile up of neutral gas ahead of the expanding HII region begins with a strong shockwave.

As the shockwave moves compressing the surrounding neutral gas, the density of the latter rises and a pressure balance is attained at the ionization front. This configuration consisting of a shockwave followed by a region of compressed HI and an ionized interior grows in radius and moves out through the neutral cloud as the central star approaches the main sequence. When the ionizing star leaves the main sequence, the HII region will recombine and the expanding compressed HI shells will move out into the interstellar medium, contributing their kinetic energy to the motions there. Thus, the study of the HII regions is an important tool in the understanding of the gas dynamic processes taking place in the interstellar medium.

The early evolution of an HII region depends critically on two parameters viz. t_{on} and t_{form}, where t_{on} is the time required by the star (O or early B), approaching the main sequence to attain its full ionizing photon luminosity and t_{form} is the time required for the star to form the initial Strömgren sphere. The time t_{on} is actually the time taken by the star to reach the effective temperature at the main sequence phase (T_*) from the value at the pre-mainsequence contraction- say 10^{4°K. The time t_{form} is a measure of the nebular response time to the stellar ionizing radiation. It can be approximated to the recombination time scale of the gas. Some of the typical values of t_{on} and t_{form} are given in Table 1.1 for different stars.

Fig. 1.1 shows important domains in the age versus zero-age main sequence (ZAMS) mass of evolving stars. Numerical calculations (Bertout, 1984; Larson, 1972, 1973; Woodward, 1978; Yorke, 1985) have shown that

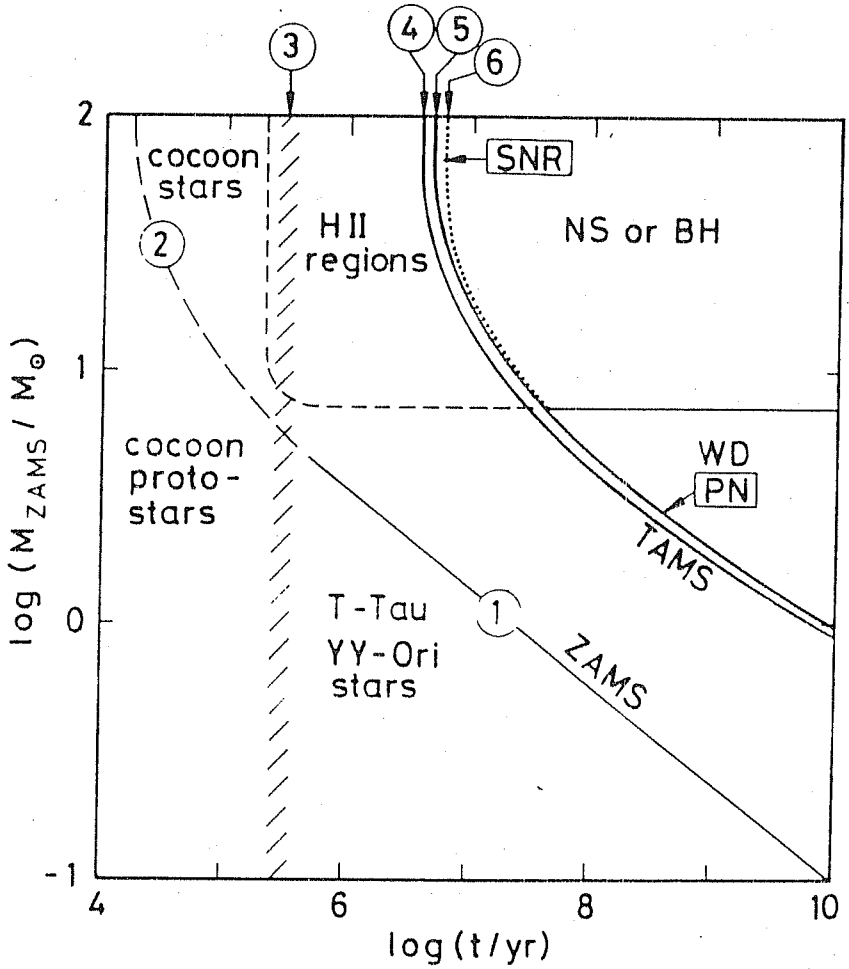

Figure 1.1: Important domains in the mass versus age plane during stellar evolution (adapted from Yorke, 1986).

for the first 10^5 years a cocoon protostar continues to accrete material from the envelope. For protostars more massive than $3 - 5M_\odot$ hydrogen burning begins (curve 2) before accretion phase ends (curve 3). These are identified as *cocoon* stars. During the accretion phase, the protostar is not visible optically. Low mass stars ($M < 3M_\odot$), e.g., YY Orionis and T Tauri, are visible optically before they reach main sequence (curve 1). If the protostar is massive enough ($M > M_\odot$), there is formation of HII regions during advanced stages of accretion .

1.7 Emission line spectrum in a diffuse nebula

The emission spectra in a diffuse nebula is dominated by collisionally excited 'forbidden' lines such as [OIII] 4363 Å, 4959 Å, 5007 Å, [NII] 6548 Å, 6583 Å, [OII] 3726 Å, 3729 Å and permitted recombination lines of Balmer series of hydrogen, HeI 5876 Å, and HeII 4686 Å, and weak lines of carbon. Ultraviolet photons from the central hot star with energies greater than the ionization potential of hydrogen (13.6 eV) photoionize the hydrogen atoms (being most abundant) and the so liberated electrons carry off with them the excess energy in the form of kinetic energy. This results in the net heating of the HII region. The capture of an electron by a protron in a bound state occurs to excited levels and the decay of the atom to lower levels by radiative transitions results in the emission of line photons. Recombination of

H^+ gives rise to optical as well as radio recombination lines such as H 109α at 6cm. The inelastic collisions between the thermal electrons and the ions results in raising incompletely ionized atoms (viz., singly, doubly or triply ionized) like oxygen, nitrogen, sulphur, neon etc. to an excited level with only a small difference in energy from ground state. This leads to the overall cooling of the HII region, providing a thermostatic mechanism to keep the temperature of the region around 10^4°K. Such low lying energy levels are known as metastable states, since the atom does not have any permitted electric dipole radiative transitions from these states. For example, let us consider the energy level diagram of O^{++} and N^+ (Fig. 1.2). The lowest energy level contains fine structure with energy differences between levels of $\sim$ 0.01 eV. There are no allowed transitions between these levels in terms of electric dipole transitions, but either electric quadrupole or magnetic dipole transitions can take place. The probabilities of these transitions are low ($\sim$ 1 sec^{-1}) compared to those for electric dipole radiation (10^8 sec^{-1}). Radiative transition from these excited levels results in the emission of a forbidden line, which is not possible under normal terrestrial conditions. At the low densities ($n_e \leq 10^4 cm^{-3}$) of the nebulae, collisional de-excitation, the reverse process to the collisional excitation is not possible.

1.7.1 Continuum emission

The nebular spectrum in the visible is predominantly composed of strong emission lines. At radio and infrared regions however, the continuum radia-

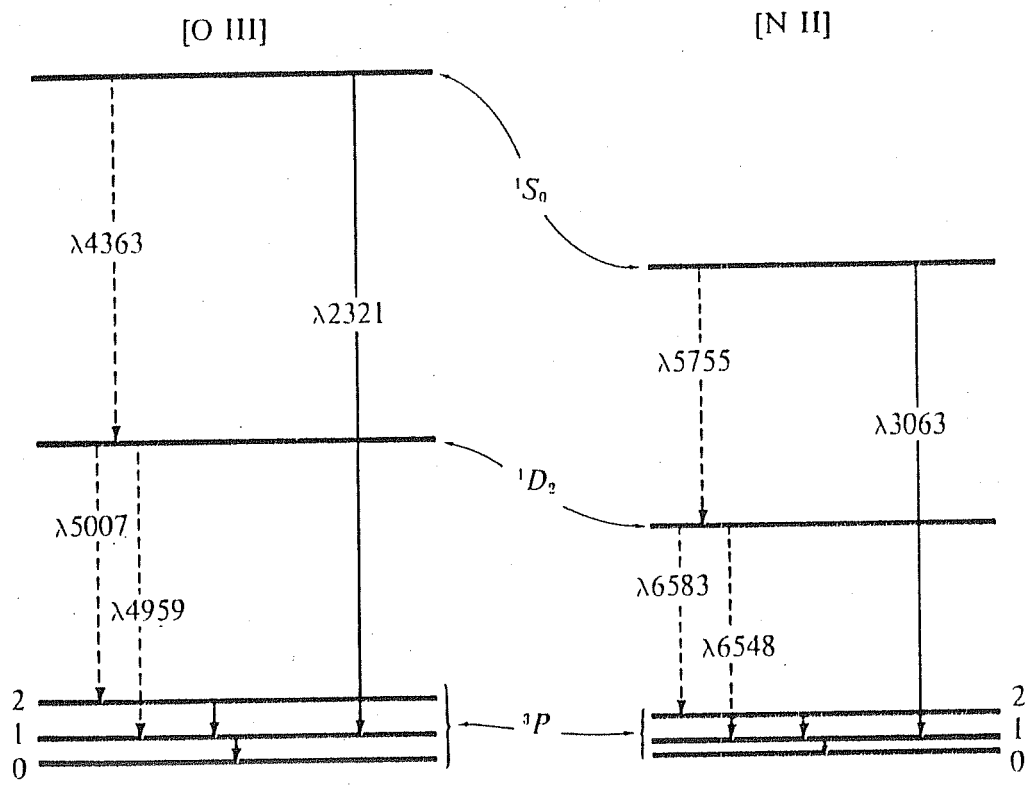

Figure 1.2: Energy level diagram for [OIII] and [NII] forbidden line transitions (adapted from Osterbrock, 1974).

tion becomes important in the nebular emission spectrum. The main source of continuum emission is the *free-free* radiation or Bremstrahlung radiation from the thermal electrons. The electrons encounter protons or other ions at a temperature of 10^4°K in the HII regions and are accelerated due to the coulomb attraction between the charged particles. These accelerated electrons produce free-free emission in the continuum spectrum. At high temperatures, the free-free radiation could be significant in the x-ray, optical and infrared wavelengths. However, this may occur predominantly in supernovae remnants. Emission lines of H, He and some other elements are found to be superimposed on the continuum spectrum.

1.7.2 Infra-red Emission

In the infrared region, especially beyond $10\mu m$ or so, a more important source of continuum emission is dust grains than the free-free radiations. The dust surrounding the hot star gets heated up and reradiates all the absorbed radiation in the infrared region. Since the extinction varies inversely with wavelength ($E = c\lambda^{-1}$), the advantage of the studies in infrared is that it can probe the areas which are obscured by dust and are not accessible in the optical region.

1.8 Determination of temperature in the nebulae

The fact that the intensity of a forbidden line is a function of electron density and electron temperature may be used to determine these parameters from ratios of intensity of properly selected forbidden lines. The temperature in a nebula can be determined by measuring the ratio of the intensities of two emission lines of a single ion from two levels with different excitation energies. For example, the ions like [OIII] and [NII] have emission lines occurring from different energy levels having different excitation energies; e.g., [OIII] 4363 Å occurs from D level while [OIII] 4959 Å and [OIII] 5007 Å occur from S level (Fig. 1.2). The collisional excitation to D level requires an electron energy of 5.35 eV where as to S level requires 2.5 eV giving a difference of 2.85 eV in excitation energy between the two levels. Therefore the ratio of these lines strongly depends on the electron temperature. So, the measurement of the line strengths emitted from these levels will give the temperature. By considering the different transition probabilities of line emission from the energy levels, it is shown that the ratio of line intensities are given as follows (Osterbrock, 1974):

$$\frac{I(4959+5007)}{I(4363)} = \frac{8.32\,exp\,[(3.29\times10^{4})/T]}{1+(4.5\times10^{-4}n_e/T^{\frac{1}{2}})} \tag{1.8}$$

where T is the temperature, n_e is the electron density and I, the intensity of the line under consideration. Therefore, assuming that the nebula is isothermal and has sufficiently low density, this equation can be used to

determine the temperature of the nebula. Temperature determinations can also be made from optical continuum and radio-continuum measurements (Osterbrock, 1974).

1.9 Shock waves in the Interstellar Medium

Whenever there is a sudden injection of matter and energy into the interstellar medium either due to the outflows from young stellar objects (YSOs), stellar winds from OB stars and the expansion of their HII regions, red giant outflows, planetary nebulae ejection, Wolf-Rayet winds and supernova explosion, it results in supersonic motions and hence generation of shock waves in the interstellar medium. The shocks affect the interstellar dynamics by triggering the formation of a star or terminating the growth of a protostar by driving away the gas. Therefore the study of shock waves serves as a powerful diagnostic tool for the understanding of the underlying energetic phenomenon occurring in the interstellar medium. They help in the study of gas dynamics by heating the gas and causing it to radiate.

As the shock propagates, several physical processes are in action: (i) the heating and ionization of the gas ahead of the shock by the radiation or fast particles; (ii) acceleration, compression and heating of the gas by the shock front; (iii) collisional excitation, ionization, recombination, dissociation and molecule formation in the post-shock region; and (iv) absorption and re-emission of the radiation from the gas in regions downstream. Broadly the

shocks are classified into two categories: (i) radiative shocks in which the electron column density N passing through the shock is greater than N_{col} which characterises the post-shock cooling region and (ii) non-radiative in which N_{col} is larger than N. Further, if the dissipative processes occurring in the shock front are due to turbulent electric and magnetic fields rather than collisions in the plasma, then such shocks are called collisionless shocks. We shall deal here with the radiative collisional shocks as these are relevant for the HII regions.

The radiative shocks can further be classified into two types (Hollenbach, 1982): (i) J shocks created due to a pressure disturbance across which the physical parameters viz., temperature, density and flow velocity of the gas suffer a virtually discontinuous jump in a distance short compared to the radiative length. The shock velocities in the case of J shocks are $v_s \geq 40$–50 km/s. This type of shocks are supposed to dissociate cooling molecules and ionize the gas.

(ii)The second type of shocks known as C shocks occur at relatively low velocities. This type of shock depends on the existence of magnetic field. The molecules are not dissociated in the case of C shocks. Typical velocities in the C shocks are $v_s \leq$40-50 km/s.

1.9.1 Theory of shock waves

The detailed theory of shock waves can be found in the literature (Kaplan, 1966; Osterbrock, 1974). Some of the important characteristics of the shock front and the ionization front are discussed briefly here. It is known that when a hot star (OB) ionizes the surrounding gas, the expansion of the gas into the neutral regions begins with a strong shock wave and a discontinuity is set up at the HI–HII interface. Discontinuities are the surfaces where the velocity and the thermodynamic gas parameters undergo abrupt changes. At the shock front considered, there is a flow of gas through the discontinuities but the degree of ionization does not change. The momentum, mass and energy conservation conditions across the front are defined respectively as follows:

$$p_o + \rho_o\, v_o^2 = p_1 + \rho_1\, v_1^2 \tag{1.9}$$

$$\rho_o v_o = \rho_1 v_1 \tag{1.10}$$

$$\frac{1}{2}v_o^2 + \frac{\gamma}{\gamma-1}(p_o/\rho_o) = \frac{1}{2}v_1^2 + \frac{\gamma}{\gamma-1}(p_1/\rho_1) \tag{1.11}$$

where subscripts 0 and 1 denote the physical parameters (ρ, density; p, pressure and v, velocity) ahead of and behind the shock respectively. γ is the ratio of specific heats. These conditions are known as *Rankine-Hugoniot* jump

conditions for the discontinuities at the shock front. To a first approximation, the temperature in the nebula is fixed by radiative processes and the shock front is considered isothermal. Therefore eq. 1.11 with γ =1 becomes,

$$p_o\rho_1 = p_1\rho_o = kT/\mu m_H \tag{1.12}$$

where μ is mean molecular weight, m_H is the mass of hydrogen atom and k is the Boltzmann's constant.

1.10 Ionization front

As mentioned earlier, the UV photon flux emanating from a hot central star triggers an ionization front which runs through the surrounding neutral medium (HI region) supersonically leaving behind an ionized hydrogen (HII) region. As a result of this there develops a temperature and pressure difference between the ionized and neutral media and the hot gas expands. As this expansion velocity usually exceeds the sound velocity in the HI region, a shock front is generated which moves out. The ionization front can be treated as a shock front. The thickness of the front is greater than the mean free path of the photon. Generally ionization fronts are associated with peculiar motions of the gas. The shock front jump conditions as given by the eqns. 1.9, 1.10, 1.11 are applicable across the ionization front as well. The flow of a gas through the ionization front depends on flux of ionizing photons that are arriving at the front. The velocity of sound c_o ahead of the front is

given as

$$c_o = \sqrt{\gamma p_o/\rho_o} = \sqrt{\gamma k T_o/\mu_o m_H} \tag{1.13}$$

and behind,

$$c_1 = \sqrt{\gamma p_1/\rho_1} = \sqrt{\gamma k T_1/\mu_1 m_H} \tag{1.14}$$

The Mach number is defined as the ratio of the speed of the shock ahead of the front to the speed of sound in the gas.

$$M = v_o/c_o \tag{1.15}$$

then the ratio of the densities is given as

$$\rho_1/\rho_o = \frac{(\gamma+1)M^2}{(\gamma-1)M^2+2} \tag{1.16}$$

Considering eqn. 1.12 for the isothermal sound speed with γ =1 and solving for densities, we get,

$$\frac{\rho_1}{\rho_o} = \frac{c_o^2 + v_o^2 \pm [(c_o^2+v_o^2) - 4c_1^2 v_o^2]^{1/2}}{2c_1^2} \tag{1.17}$$

Therefore, there should be two allowed values of the ionization front velocities in HII regions

$$v_o \geq c_1 + \sqrt{c_1^2 - c_o^2} \equiv v_R \approx 2c_1 \tag{1.18}$$

$$v_o \leq c_1 - \sqrt{c_1^2 - c_o^2} \equiv v_D \approx c_o^2/2c_1, \tag{1.19}$$

where v_R is for a *R - critical front*, R stands for rare or *low density* gas and v_D is for a *D - critical front* where D stands for the dense or high density gas. It is found that R type fronts move supersonically into the undisturbed gas ahead of it, whereas D type front move subsonically.

Behaviour of R and D type fronts in the expanding HII region

When an early type star is switched on in a neutral cloud, an R type ionization front moves supersonically into the neutral gas. The temperature gradient between the ionized and neutral medium sets up an expansion of the ionized gas. A shock front close to the ionization front forms as the expansion velocity exceeds the sound speed in the neutral medium. The ionizing flux decreases after some distance due to geometrical dilution and also to some extent due to radiative recombinations. After this time, the R type front changes into a D critical front and moves rather subsonically. At this point, the shock front breaks off from the ionization front. After some point the shock front weakens and ionization front continues to expand with a large density gradient. This model of the expanding HII regions is depicted in the Fig. 1.3 (Osterbrock, 1974). It is clear from the foregoing discussion, that kinematic observations are essential in order to understand the actual velocity structure across the shock features in the diffuse nebulae and for a comparison with the theoritical models which will help in understanding the evolution of an HII region.

1.11 Jets and Herbig-Haro (HH) objects

These objects were first discovered by Herbig (1948) and Haro (1952) and are tiny almost semi-stellar nebulae often in groups, situated in HII region molecular cloud complexes. It is quite logical to assume that they seem to

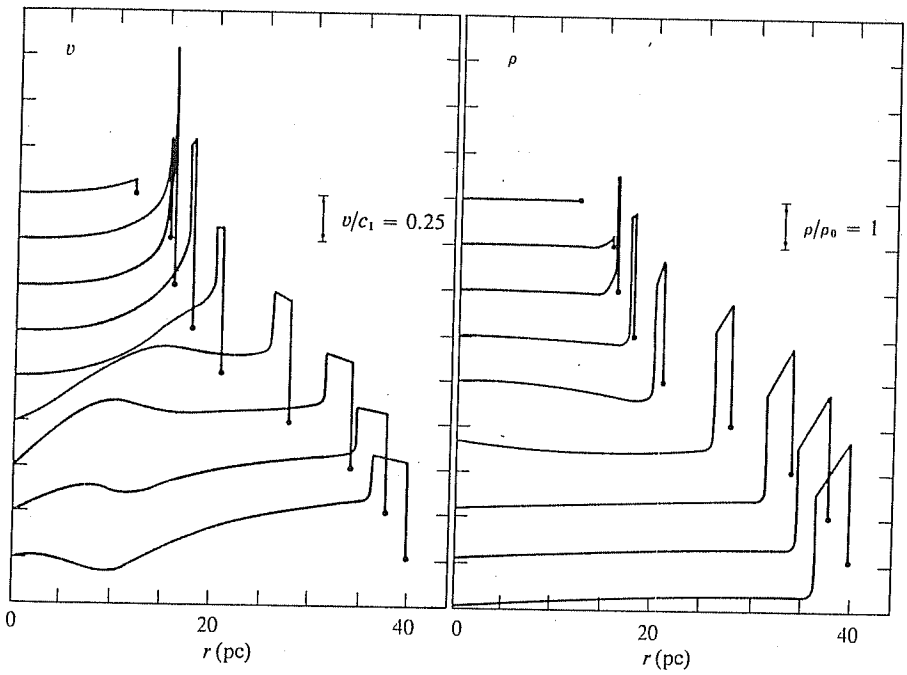

Figure 1.3: Model of expanding HII region with initial $N_H = 6.4cm^{-3}$ and v=0, around an O7 star that is turned on at t=0. Left-hand side shows v/c_1 and right-hand shows ρ_o/ρ_1, both as functions of r in pc. Successive time steps shown are 2.2×10^4 yr, 7.8×10^4 yr, 9.0×10^4 yr, 1.8×10^5 yr, 3.6×10^5 yr, 9×10^5 yr, 1.4×10^6 yr, 1.8×10^6, and 2×10^6 yr from top to bottom. Each curve is displaced downward by $v/c_1 = 0.25$ and by $\rho/\rho_o = 1$ from the previous one (adapted from Osterbrock, 1974).

be related to the process of star formation. Spectroscopic studies of HH objects revealed that these objects represent radiative shocks resulting from the interaction of a supersonic stellar wind from an embedded protostellar source with the surrounding medium (Schwarz, 1975). In a typical HH object, permitted and forbidden emission from neutral atoms (e.g., OI [OI], [CI], [NI]) and from ions of low excitation energy (e.g., CaII, [CaII], MgII, [FeII], SII) are found to be much stronger than in common photo-ionized nebulae. They are characterized by radial velocities of the order of 100 km/s (Schwarz and Dopita, 1980).

1.12 Turbulence

The significance of turbulence in astrophysical plasmas was first pointed out by Rosseland (1929) and later reviewed by Chandrasekhar (1949). The signature of turbulence in astrophysical nebulae is revealed in the emission lines. The width of an emission line profile, to a first approximation is made up of (i) the thermal width which is due to the Maxwellian distribution of the velocities of the atoms or ions in the gas at a given temperature and (ii) expansion or rotation of the gas (neglecting the natural width). But the observations of radial velocities in HII regions showed that even after accounting for these widths there was an excess which was randomly distributed across the regions. This excess width was attributed to the presence of turbulence in the gas motions.

1.12.1 Introduction

An irregular or disordered state of a fluid may be referred to as *turbulence.* Turbulence is characterised by the presence of random fluctuations of physical parameters of a fluid (like density, temperature, velocity) in temporal and spatial scales, much shorter than the dynamical scales of the fluid. The analysis of turbulence is based on the postulate of the existence of a range of scale sizes of turbulent motion. Energy is being continually passed from larger to smaller scale motions. A lower limit is eventually reached when the energy has been passed down to fluctuations that are too small to permit the formation of still smaller scales. At this point the energy is directly converted into random motions of molecules by viscous forces and gets thermalised. These different scale sizes are termed as eddies. The average properties of small-scale components (molecules) of any turbulent motion are determined uniquely by (i) the kinematic viscosity of the fluid, $\nu{=}\eta/\rho$, where η is the coefficient of viscosity and ρ, the mass density of the fluid and (ii) the average rate of dissipation of energy per unit mass of the fluid, ϵ. The energy acquired by the largest eddies is conveyed without dissipation to progressively smaller and smaller eddies until the smallest scales of molecules are reached whence the energy is dissipated into heat by the viscosity of the fluid. How and from where the largest eddies acquire the energy are the questions which are yet to be answered. Turbulence, being a heating agent, if present, could play a significant role in the star formation processes and hence needs a great attention. Turbulence is usually characterised by condition for its occurrence

as follows:

$$R_l = \frac{l v_l}{\nu} >> 1 \tag{1.20}$$

where, l is the scale size, v_l is turbulent eddy velocity at this scale and ν is the kinematic viscosity. This characteristic number R_l called *Reynolds number*, is simply the ratio of turbulent to viscous motions. If it is greater than unity, then the turbulent motions cannot be damped out by viscosity. It was pointed out by Rosseland (1929) that in the case of astrophysical objects the length scale l and hence the Reynolds number are very large leading to the possibility of the existence of turbulence in them. In HI region where $\nu = 10^{23} cm^2/\text{sec}$, v_l = 10 km/s and l=10 pc, R_l is $\approx$ 300. In HII regions, R is found to be still larger, implying that the gas motions there are possibly in turbulent state (Kaplan and Pikelner, 1966). Mathematical formulation for the study of turbulence was first given by Kolmolgorov (1941).

1.12.2 Kolmogorov's prescription of turbulence

The standard Kolmogorov model describes a statistical treatment of turbulence in an isotropic, homogeneous and incompressible fluid, where the energy spectrum of the turbulence is determined only by the rate of kinetic energy dissipation ϵ and the kinematic viscosity ν. When $R_l >> 1$, the spectrum depends only on ϵ and the energy is transferred in a dissipationless manner into the smaller and smaller elements called turbulent eddies until it reaches the intrinsic molecular scale whereon dissipation occurs.

With these assumptions, Kolmogorov had shown that the energy spectrum ϵ (k) is given by

$$\epsilon(k) \propto \epsilon^{2/3} k^{-5/3} \tag{1.21}$$

where k is the wave number ($\sim l^{-1}$) and ϵ is the energy per unit mass.

Assuming that the energy transfer occurs from the largest to the smallest eddies, and that the largest eddy of size l_{max} exists for a time $t_{l_{max}}$, we have

$$t_{lmax} = l_{max}/v_{lmax} \tag{1.22}$$

where v_{lmax} is the velocity of the eddy of size l_{max}. Now the rate of kinetic energy tranfer from this eddy to the next one is,

$$\epsilon_{max} \propto v_{lmax}^2/t_{lmax} \approx v_{lmax}^3/l_{max} \tag{1.23}$$

As we have assumed that the energy is transferred in a dissipationless condition, we have ϵ , a constant throughout this process. Therefore,

$$\epsilon_{max} \propto v_{l_{max}}^3/l_{max} = v_l^3/l = constant \tag{1.24}$$

for all values $l_{min} < l < l_{max}$ or

$$v_l^3 \propto l \qquad or \qquad v_l \propto l^{1/3} \tag{1.25}$$

Thus, a correlation must exist between v_l and l in the diffuse nebulae, if there are turbulent motions, in which the slope of v versus l is ~ 0.33. If the energy is dissipated in shock waves, there will be reduction in ϵ during transition to smaller scale motions and therefore the slope becomes still steeper, i.e., $v \sim l$ (Kaplan & Pikelner, 1966). Thus it becomes important also to know whether the turbulent velocities are subsonic or supersonic. Furthermore, the assumption that the fluid is incompressible (spatial invariance of density) is quite drastic and is largely unrealistic in astrophysical plasmas.

1.12.3 Observational determination of Turbulence

Eventhough turbulence manifests itself in several physical parameters characterising the nebulae, it is the radial velocity that can be determined most accurately and hence it has been one of the major endeavours of the spectropists to measure and understand the random radial velocities in the nebulae. In principle, one can estimate the turbulence by analysing the observed widths of the emission lines or their Doppler shifts (giving radial velocities). The excess broadening in the line width (Δv) in comparison with the thermal motions and other large scale motions like expansion/rotation can be attributed to the presence of random motions (turbulence) in the interstellar medium. It was shown by Larson (1981) that there exists a relationship between the turbulent dispersion and of the eddies of scale size l of the form $\Delta v \propto l^{\alpha}$, with $\alpha = 0.8$ in order that the gas be turbulent. But, this method suffers from a drawback, in the sense that the linewidth is just a measure

of the range of line-of-sight velocities and a longer line of sight through the nebula can be thought of as sampling larger number of fluctuations. Therefore, it is not possible to apply corrections appropriately for gradients and fluctations in the velocities along the line of sight and a better method was required in order to make a statistical study of turbulence. Since the random motions in the fluid characterize the statistical order in the flow, two statistical functions are defined for the study of turbulence (Scalo, 1984):

(i)Correlation function: $< D(r) = v(r')v(r'') >$, which is the averaged product of velocity components with respect to a large number of paired points at r' and r'', so that the vector $r' - r''$ is constant.

(ii)Structure function: $B(r) =< |v(r') - v(r'')|^2 >$, which is formed by taking the average of the square of the difference between the velocity at the paired points r' and r''. Based on Kolmogorov's model one can show that $B(r) \propto r^{2/3}$.

Out of these two, the structure function which takes the differences in velocities is more reliable because of the aforementioned depth of the line of sight arguments. Using these several ways, there have been a number of attempts to determine the nature of turbulence in HII regions (O'Dell, 1986; O'Dell & Castañeda, 1987; O'Dell et al, 1987; Roy & Joncas, 1985, Castañeda, 1988, O'Dell, 1993). The results, however, have not been conclusive.

1.13 Models for expansion of HII regions

Several empirical and theoretical models have been put forward in the past to explain the observed large scale velocity flow from nearby HII regions.

1.13.1 Spherical model

According to this model the gas expands uniformly in all directions in a spherical cloud centred around the exciting star. The model predicts blue-shifted velocity components from the front side and red-shifted ones from the backside of the HII region. If the expansion velocities are sufficiently large, one may get a split profile along the line of sight. The observed velocity flow in the Orion nebula, the nearest HII region was interpreted in terms of the spherical model (Wilson et al, 1959). But there was disagreement in two respects: firstly, the radial velocities did not show any systematic trend and secondly there were no red shifted velocities observed from the back of the cloud. With more observations coming up, the picture became more clear and a model proposed by Zuckerman (1973) called 'Blister model' was able to explain the observations more appropriately.

1.13.2 Blister Model

According to this model an HII region is a protrusion off the front edge of a dense parent molecular cloud situated behind the central exciting star

(Fig. 1.4). The ionizing star is supposed to be situated at the edge of the molecular cloud. When the HII region is formed, a large pressure gradient is set up at the HI-HII interface. The nebula is ionization-bounded at the back side (towards the molecular cloud) and density-bounded at the front side. Therefore, the ionized gas expands rapidly towards the observer and is blue-shifted with respect to the molecular cloud and there is no corresponding redshifted velocities from the back half of the cloud. Thus the expanding HII region encounters the low density interstellar medium on outside and the high density molecular cloud on the other and hence the expansion has no spherical symmetry. Observations of Orion nebula at radio wavelengths (Zuckerman, 1973) seem to agree with the proposed model. Observations at millimeter wavelength of molecules CN and H_2 (Kutner and Maddeus, 1971, Kutner et al. 1971) had already revealed that the molecular cloud is located behind the HII region.

1.13.3 Champagne Model

To start with, the model assumes a main sequence O star with its Strömgren sphere placed inside and near the edge of a molecular cloud as shown in the Fig. 1.5 (Tenorio-Tagle, 1979). At this stage, the HII region is not observed optically. As the star forms its Strömgren sphere, ionizing the surrounding material a pressure gradient is set up at the HI-HII interface and this will result in the formation of an ionization front. The ionization front rushes into the interstellar medium whereas a rarefaction wave moves towards the star.

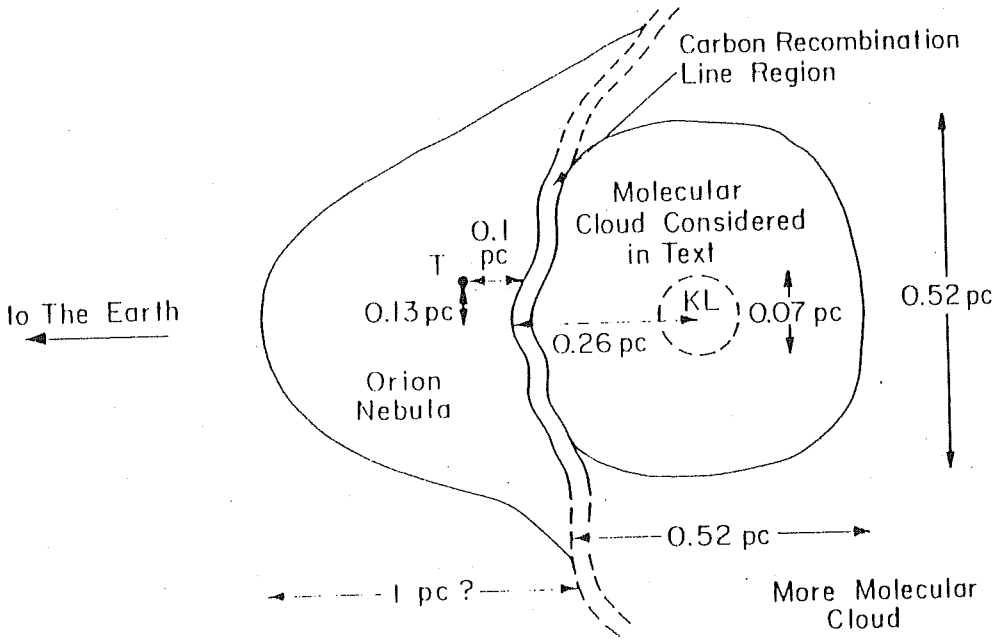

Figure 1.4: Blister model (adapted from Zuckerman et al, 1973).

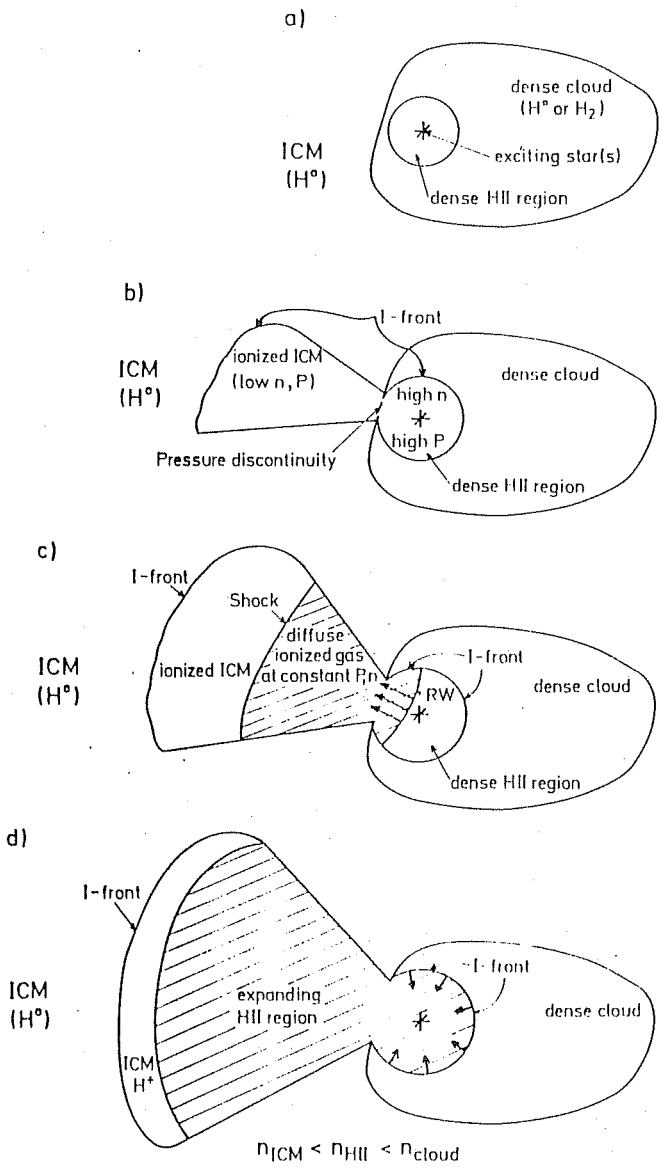

Figure 1.5: Champagne model (adapted from Tenorio-Tagle, 1979) depicting various evolutionary stages (from (a) to (d)) of a HII region.

The ionized material flowing behind the shock wave will be spread over a very extended region producing an observable ionized nebula. The situation resembles that of a shock tube when the pressure is suddenly released. Detailed hydrodynamical computations have been made (Tenorio-Tagle, 1979, 1982) based on this model to find the distribution of velocity, density and temperature of the gas.

1.13.4 Stellar wind bubble model

According to this model, the principal ionizing star forms a cup-shaped cavity of ionized gas as it moves into the neutral cloud (Fig. 1.6). It was proposed that the bubble could be created due to the radiation pressure from the star. The bubble obstructs the flow of gas from behind the star and therefore the gas flow gets deflected at larger angles to the line of sight and the radial velocities at the centre are more red-shifted. (Pankonin et al, 1979). They made a study of the velocity structure in the Orion nebula by observing the H76α radio recombination line. Their observations showed the presence of a maxima around 30$''$ west of the principal ionizing star θ^1 C Ori. General velocity pattern showed blue-shifted velocities at the outer regions and red-shifted velocities at the center. An interpretation of the observed characteristics was made by putting forward a stellar wind bubble model.

Essentially these different models are manifestations of different stages of evolution of an HII region. The Blister model represents a stage prior to

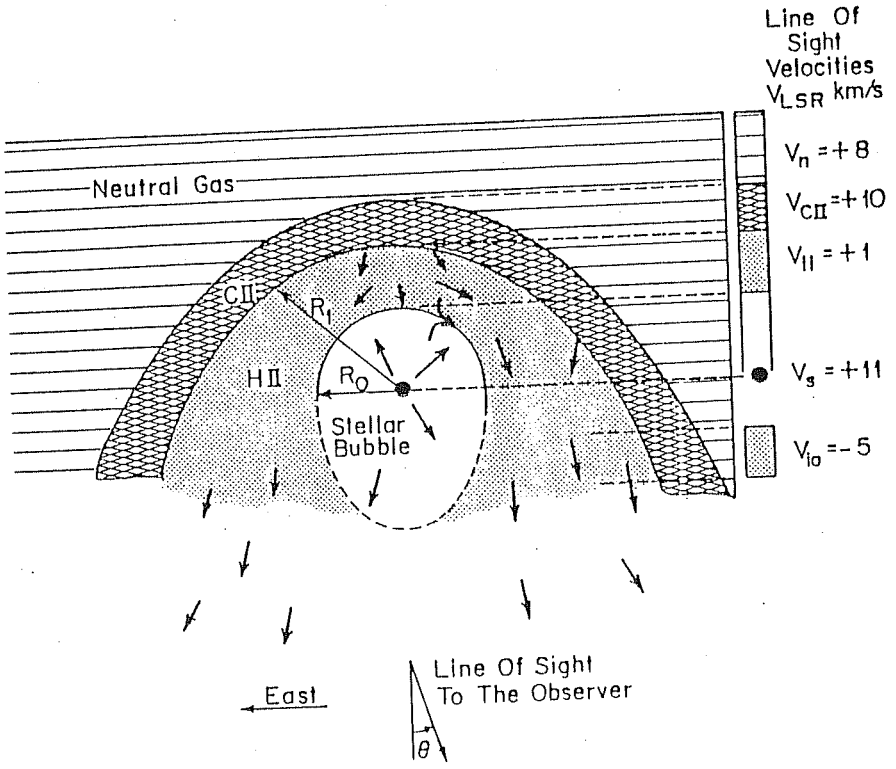

Figure 1.6: Stellar wind bubble model (adapted from Pankonin et al, 1979).

the champagne model and the Stellar wind bubble model is perhaps a stage prior to the former. From the velocity field structure it is possible to identify presently at what stage a particular HII region is.

1.14 Motivation for the present work

A survey of the studies made in the past on several nearby HII regions reveals that the observations were restricted either to the brighter portions of the objects or were concentrated on fine scale structure like knots, jets (Wilson etal, 1959, Meaburn, 1981) and discovery of Herbig-Haro objects (Canto et al, 1981). For example, in the case of Orion nebula, the nearest HII region, few studies have been made to present a global view of the velocity structure in the nebula (e.g., Balick et al, 1974). Observations were made only on limited regions around the ionizing stars using slit spectroscopy which has the limitation of having information only along the length of the slit eventhough data were obtained in several position angles. Some studies were made over a wide region ($30'$) of the nebula (Hanel, 1987) but the spatial resolution was very low ($1'$). Recent observations by Castaneda were made at high spectral ($\sim$ 1 km/s) and spatial resolution ($1''$) with modern panoramic detector like CCD behind a slit spectrograph at several position angles. But his observations were confined to about 2 arc minutes in diameter around θ^1 Ori and θ^2 Ori which could not allow for global study of velocity structure across the nebula. Furthermore, recently Hubble Space Telescope (HST)

with its wide field camera has discovered several interesting features in the Orion nebula, like jets, knots etc around which there are no velocity field measurements made so far. No doubt, the velocity field maps will help in understanding the features better. Therefore, there was a need to make a velocity field study over an extended region in some nearby HII regions with reasonably good spectral and spatial resolution in order to study the velocity field not only near the central ionizing star but around other regions containing interesting features like ionization fronts etc. This necessitates the building of a viable high resolution spectrometer with imaging capabilities which utilises a modern digital panoramic detector rather than conventional photographic plates.

1.15 Aim and scope of the present study

Having been motivated thus, we set the following aims for the present study: (i) design and construction of a high-resolution imaging Fabry-Perot spectrometer that utilizes a photon-counting detector; (ii) To generate a velocity field map over a much larger region across the nearby HII regions namely, the Orion and the Trifid nebulae; (iii) Try and construct a comprehensive picture of the global velocity structure across these HII regions as well as understand some localized features and turbulence keeping in view of the recent observations made by several other workers using ground-based as well as satellite-based instrumentation in different spectral regions.

Chapter 2

THE IMAGING FABRY-PÉROT SPECTROMETER (IFPS)

History of Fabry-Pérot spectrometer dates back to the late 19th century, when it was invented and used to calibrate the length of standard metre with the Cadmium line by Fabry and Pérot (1899). It was, however, Buisson and Fabry (1914) who first initiated the use of Fabry-Pérot spectrometers in astronomical studies, by making observations on the Orion Nebula.

With the technological developments in the following decades, capabilities of Fabry-Pérot spectrometer received a boost and it has found a wide-ranging applications in astronomy. It has become an important tool to extract kinematic information in extended astronomical sources like HII regions, Planetary nebulae and galaxies as well as comets and solar corona. The concentric

fringe system from a Fabry-Pérot étalon has a unique advantage for obtaining spectroscopic images as each point on any circular fringe corresponds to a spatial position on the sky. This advantage combined with the facility of wavelength scanning of the étalon is quite useful in the spectroscopy of extended sources. One can also use the étalon for obtaining emission line profiles over a limited spatial region (especially for point sources or in cases when a two-dimensional detector is unavailable) by selecting only the central fringe and scanning in wavelength.

Studies were carried out both in central fringe scanning mode using photoelectric techniques (e.g. Foukal, 1969) as well as in the two-dimensional interferometric mode for spatial information using essentially unaided or aided (with image intensifier tubes) photographic techniques (Courtés, 1960; Monnet, 1971; Tully, 1974; de Vaucouleurs and Pence, 1980). Recent developments in the two-dimensional digital panoramic detectors such as Charge-Coupled Devices(CCD), Imaging Photon Counting Systems (IPCS), Imaging Photon Detector (IPD) have brought a resurgence in the field of astronomy. These imaging detectors combined with the servo-controlled piezo-étalons (in which the étalon gap is created by spacers made of piezoelectric materials) have led to the development of Imaging Fabry-Pérot spectrometer systems - TAURUS (Atherton et al, 1982), CIGALE (Boulesteix et al, 1983), HIFI (Bland and Tully, 1989). We have designed and constructed one such Imaging Fabry-Pérot Spectrometer (IFPS) using Imaging Photon Detector (IPD). The following sections will give the details about the Fabry-Pérot Spectrom-

eter (FPS) and the fabrication, performance and important characteristics of the IFPS.

2.1 Theory and Definition of FPS

Detailed theory and practice of the Fabry-Pérot spectrometer is discussed in the excellent books by Born and Wolf (1970), Meaburn (1976), Hernandez (1986) and Vaughan (1989). Some of the important and relevant features for its selection for the present studies will be discussed in this section.

A Fabry-Pérot étalon essentially consists of a set of nearly perfectly flat (λ /100) parallel plates with their internal surfaces coated for high reflectivity ($\geq$ 90%) in a given range of wavelengths. An incident monochromatic beam of light of wavelength λ from an extended source when passed through the étalon would undergo multiple internal reflections. The emerging beams in transmission would then give rise to a set of concentric circular fringes of maxima when there occurs constructive interference with the following condition:

$$2\mu t cos\theta = n\lambda \tag{2.1}$$

where μ is the refractive index of the medium between the plates of the étalon, t the gap between them, θ the angle of incidence, and n the order of interference. Each point on the fringe corresponds to a specific region in the extended object on the sky. The resulting transmission pattern is a train of periodic pulses each of which can be given by what is known as the Airy

function

$$A(\lambda) = \left\{1 + \left[\frac{4R}{(1-R)^2} sin^2\left(\frac{2\pi\mu t cos\theta}{\lambda}\right)\right]\right\}^{-1} \tag{2.2}$$

where R is the reflectivity of the coatings. The following are some of the most important parameters that characterize the FPS.

1. Free Spectral Range: The period of the Airy function is known as the free spectral range (FSR) of the FP which gives the range in wavelength between two successive maxima and can be defined from eqn. 2.1 as

$$\Delta\lambda = \frac{\lambda^2}{2\mu t} \tag{2.3}$$

2. The full-width at half maximum: The full-width at half maximum (FWHM) of the peak defines the resolving power of the instrument and for high reflectivity it is given as (eqn. 2.2),

$$\delta\lambda = \Delta\lambda \frac{(1-R)}{\pi\sqrt{R}} \tag{2.4}$$

As is clear, a large value of the reflectivity R assures a small $\delta\lambda$ and hence a high resolution.

3. Finesse: The ratio of FSR to FWHM defines the finesse of the Fabry-Pérot spectrometer. The coefficient of reflective finesse is given as

$$N_R = \frac{\Delta\lambda}{\delta\lambda} = \frac{\pi\sqrt{R}}{1-R} \tag{2.5}$$

Finesse, in general, represents the number of interfering beams or the number of resolvable spectral elements in one FSR. A large finesse is assured if the reflectivity is greater than 90%.

4. Contrast: The contrast C is defined as the ratio of the transmission at the maximum of a passband to the transmission at the minimum between passbands

$$C = \left[\frac{1+R}{1-R}\right]^2 \tag{2.6}$$

This is a crucial parameter especially when continuum from the source becomes significant. Here too, a large R generates a large C.

5. Resolving Power: Two profiles of equally intense lines separated by $\delta\lambda$ are said to be resolved if the intensity in the dip of the resultant profile is 83% of the peak intensity (which is in close agreement with the Rayleigh criterion for resolving two closeby spectral lines).

The resolving power of FP étalon is given as:

$$R_p = \frac{\lambda}{\delta\lambda} = nN_R \tag{2.7}$$

In practice, there are deviations from perfect parallelism and flatness of plates of Fabry-Pérot combining with the fact that we use a finite aperture size resulting in the broadening of the instrument function and hence deteriorating the resolving power. Therefore, the instrument function is a convolution of Airy function $A(\lambda)$, aperture function $F(\lambda)$ and defect function $D(\lambda)$

$$I(\lambda) = A(\lambda) * F(\lambda) * D(\lambda) \tag{2.8}$$

Let us now examine briefly various defects contributing to the deterioration of the parallelism.

1. Plate defects: The plate defects are generally caused due to three factors (Atherton et al, 1982) as described in the following:

   (i) Curvature effect: The plates in general, could have a curvature and hence be bow shaped in parts with a maximum excursion from the plane surface of δt, then the finesse due to this effect is

$$N_{DC} = \frac{\lambda}{2\delta t} \tag{2.9}$$

   (ii) Broadening due to surface irregularities or microtopographic polishing errors is assumed to follow a Gaussian distribution and the corresponding finesse is,

$$N_{DG} = \frac{\lambda}{\delta t_G \times 4.7} \tag{2.10}$$

   (ii) The finesse corresponding to broadening due to departure from parallelism (for a wedge shaped gap) is given by:

$$N_{DP} = \frac{\lambda}{\delta t_p \times \sqrt{3}} \tag{2.11}$$

   Combining the above three, the effective defect finesse N_D is given by:

$$\frac{1}{N_D^2} = \frac{1}{N_{DC}^2} + \frac{1}{N_{DG}^2} + \frac{1}{N_{DP}^2} \tag{2.12}$$

2. Effect of finite aperture: The use of finite aperture results in the broadening of the instrument function which is defined as a rectangular function given as :

$$N_A = \frac{2\pi}{n\Omega} \tag{2.13}$$

   where Ω is the solid angle subtended at the FPS.

Therefore the total effective finesse is given as follows:

$$\frac{1}{N_E} = \left[\frac{1}{N_D^2} + \frac{1}{N_R^2} + \frac{1}{N_A^2}\right]^{1/2} \tag{2.14}$$

If N_R is greater than N_D, the result is that of a series of FPS's arranged parallelly transmitting at slightly different wavelengths which results in a considerable reduction in the transmission at a particular wavelength though the bandwidth is narrower. Similarly, if N_D is increased, thereby increasing the amount of incident flux, there will be a decrease in N_A and the width of the transmission profile is broadened. The optimum product (bandwidth $\times$ flux) will be obtained when

$$N_R \sim N_A \sim N_D \tag{2.15}$$

2.1.1 Merits

1. Firstly, the Fabry-Pérot spectrometer has large light gathering power. It was shown by Jacquinot (1954) that the flux F transmitted by any optical system is the product of the luminance L at the entrance aperture and the throughput α of the system. The luminance is defined as the intensity per unit area at the entrance slit and the throughput is the product of the solid angle Ω of the entrance slit subtended at the collimator, the collimator area S, and the spectrometer transmittance τ.

   Jacquinot, by comparing luminosity-resolution product of different dispersive elements, found that for a specified resolution, the solid-angle

subtended at the FPS is much larger (as also for Michelson interferometer) than that in other dispersive elements such as grating and prism. Therefore, the quantity L $\times R_p$, which is a figure of merit (for any dispersive element), is found to be

$$L \times R_p = 2\pi S\tau R_p \tag{2.16}$$

and it was found that

$$(L \times R_p)_{FP} \approx 35(L \times R_p)_{Echelle} \tag{2.17}$$

$$\approx 30 \quad to\, 100(L \times R_p)_{Grating} \tag{2.18}$$

$$\approx 300 \quad to\, 1500(L \times R_p)_{Prism} \tag{2.19}$$

2. Secondly, observations with Imaging Fabry-Pérot spectrometer (IFPS) allow two-dimensional mapping of the velocity fields in astronomical objects, an advantage over slit spectroscopy which limits observations only along the length of the slit. Therefore imaging of the source in a single narrow spectral element can be obtained.

3. Thirdly, scanning of the Fabry-Pérot in wavelength results in the expansion/contraction of the fringes thereby covering the entire field of view of the object and providing accurate line profiles almost at each spatial element.

2.1.2 De-merits

1. The main constraint with Fabry-Pérot spectrometer is its limited free

spectral range which is to be selected depending on the width of the line of interest in the astronomical objects.

2. The Fabry-Pérot spectrometer has one more disadvantage of its ill-defined instrumental profile, particularly in the wings, caused due to the continuum leakage.

2.2 Design and Fabrication of IFPS

The following section describes the optical lay-out of the IFPS, the detector used and the data acquisition system.

2.2.1 Choice of the étalon parameters

One of our main criteria in designing the IFPS has been to map reasonably large regions in extended sources. The details of the Fabry-Pérot étalons to be used are given in Table 2.1. The number of fringes that can be obtained for each étalon type as permitted by the optics chosen is listed in Table 2.2. The FSR of the étalon is selected to be large enough so as to cover the velocity structure of the envisaged source. In the case of HII regions, the Doppler velocities are at maximum $\sim$ 100 km/s. Therefore the étalon is chosen with FSR of $\sim$ 180 km/s (ET2) which is adequate for the present work. The effective finesse is $\sim$ 30, giving a resolving power of 5×10^4 at λ =5007 Å (Table 2.1).

Table 2.1: Parameters of Fabry-Pérot Étalons for use with the IFPS

Etalon	FSR (Å/km s^{-1})	Resolving[a] Power(R_p)	Wavelength Region(Å)	Velocity Resolution (Å/km s $^{-1}$)	Etalon type
ET1 PET 85	4.3/196.6	4.5×10^4	6000-7000	0.146/6.6	PZ[b]
ET2 PET 50	3.0/179.7	5.0×10^4	4500-5500	0.100/6.0	PZ
ET3 PET 28	22.2/1014.8	8.9×10^3	6000-7000	0.737/33.7	PZ
ET4 PET 28	10.2/466.2	1.9×10^4	6000-7000	0.345/15.8	PZ
ET5 OET 45	11.9/544.0	6.0×10^3	6000-7000	1.094/50.0	OC[c]
ET6 OET 20	21.5/982.8	9.0×10^3	4400-8400	0.171/32.8	OC

[a]The values given in the table are computed using $\lambda = 6563$ Å except for ET2 for which $\lambda = 5007$ Å.

[b]Piezo-electrically scanned.

[c]Optically contacted.

Table 2.2: The number of fringes for each étalon type that can be imaged on IPD at a given scanning step

Etalon	Peak wavelength (Å)	number of fringes
ET 50	5007	~ 5
ET 85	6563	~ 4
ET 28	6563	~ 2
ET 28	6563	~ 1

2.2.2 Optical system

A schematic lay-out of the instrument is shown in Fig 2.1. The Cassegrain beam from a telescope (1.21 or 2.3m, f/13; 35cm, f/11) first passes through a field aperture which isolates the desired region of the astronomical object under investigation. The field aperture consists of an iris diaphragm which can be set anywhere between 1.4 and 18 mm, whereby the field of view can be estimated from the plate factor values of 50″, 13″ and 6.8″/mm , for the 35 cm, 1.21 and 2.34 m telescopes, respectively. Object acquisition, centring and focusing in the field aperture is facilitated by both a pre-aperture, large field-of-view eyepiece, and also a second post-aperture eyepiece (with a smaller field-of-view). A flip mirror allows the light from a spectral lamp to enter the instrument for taking frames for calibration and evaluation of instrument performance, as well as to view the object in the eyepiece. The beam is then collimated by an achromatic lens of focal length 120 mm and after pre-filtering by a suitable image-quality interference filter, centred on any chosen spectral line of emission, passes through the étalon. The camera lens of focal length 120 mm images the fringes onto the detector (IPD) kept at its focal plane with a beam of f/6.7. Another aperture near the detector acts as a baffle to avoid ghost images. Also a provision has been made to tilt the FP étalon in order to throw the ghost images out of the detector's area. The design and selection of the various optical elements have been made in such a way as to minimize the vignetting effects even for the largest aperture to be used, viz. 18 mm. In designing the IFPS, it is seen that the angular

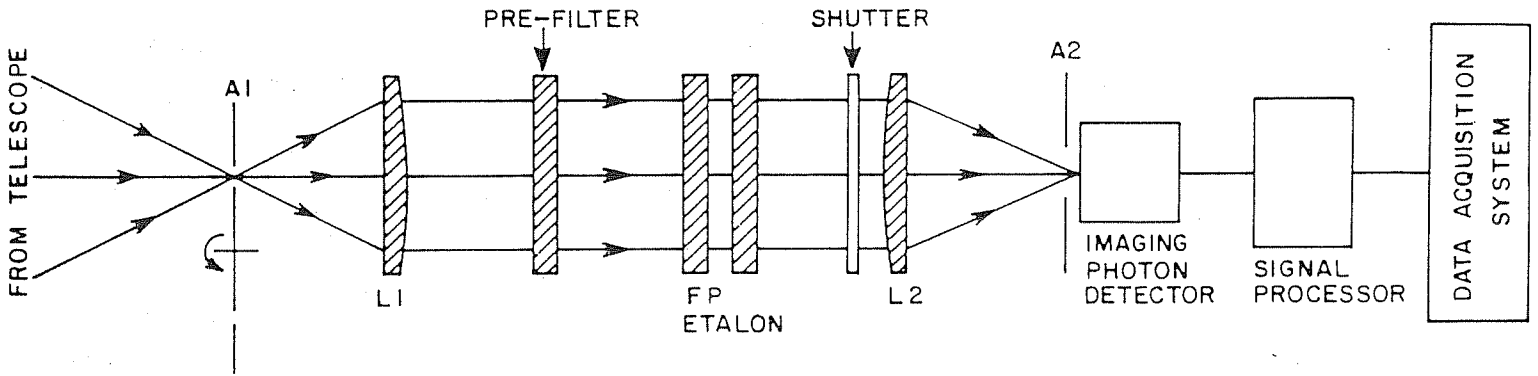

Figure 2.1: Schematic layout of Imaging Fabry-Pérot Spectrometer (IFPS).

Table 2.3: Width (FWHM) of interference fringes as imaged on the IPD covering at least one pixel (for ET2 PET 50).

Order	θ(degrees)	number of pixels
1661	1.63	2.2
1660	2.58	1.4
1659	3.26	1.2
1658	3.81	1.0

dispersion (variation of λ with θ) across an off-axis pixel (at the maximum angle from the normal) should not exceed $\delta\lambda$. This can be justified from Table 2.3 which shows that the fringe width $\delta\lambda$ of the interferogram covers at least one pixel, thus,

$$(\delta\lambda)_\theta = \frac{\lambda p}{f_{cam}} \tan\theta \leq \delta\lambda \tag{2.20}$$

where p is the size of the pixel and f_{cam} is the focal length of the camera imaging lens.

2.2.3 Scanning the IFPS

As mentioned earlier, the real advantage of the FPS comes about in terms of scanning the étalon so as to sample larger regions of the object which are not covered in a single interferogram and thus line profiles from each spatial point of the object can be obtained accurately. This becomes possible in the case of digital panoramic detectors because of their higher sensitivity and

ease in recording the data.

Before the development of piezo-étalons, scanning was done by changing the refractive index of the gas between the plates (pressure scanning). This method of scanning is rather cumbersome and has the limitations due to the dynamic range available in the gas pressure, restricting the scanning range to be less than 20 Å (Atherton et al, 1982). Also, there is a possibility of leakage of gas through the FP chamber at high pressure. With the development of piezo-electric étalons, scanning was made possible by changing the étalon spacing and maintaining the plate parallelism using servo-controlled capacitance micrometry (Jones and Richards, 1973). Earlier on, feedback systems utilized light beams for detecting the errors in the signals, which restricted the observations to only bright sources.

The étalon is piezo-electrically scanned and servo-controlled using the CS-100 servo control unit supplied by the Queensgate Instrument, U.K. The CS-100 system utilizes the principle of capacitance micrometry developed by Jones and Richards (1973) which allows pico-metre displacements to be detected. The interferometer plates are held apart by three piezo-electric transducers. The étalons are connected with five capacitors formed by evaporating gold pads onto one of the interferometer plates and fused silica pillars optically contacted to the étalon base plate. These five capacitors are mounted on one of the étalon plates in such a way that two pairs form two mutually perpendicular axes and the fifth one serves as reference. The capacitance micrometers sense variations in parallelism and departures from required

spacing. The CS-100 system receives the error signal from the capacitance micrometers and sends back appropriate voltage to the piezo-transducers for maintaining the parallelism. Thus, CS-100 system utilizes a closed-loop feedback system and maintains parallelism to better than $\lambda/2000$; correcting errors in typically less than 0.3 ms (Atherton et al, 1982). Piezo-electric transducer sensitivity is 2.4 nm/V.

The scanning steps, step-sizes and integration times are controlled by a personal computer interfaced (RS 232) with the CS-100 by using a software developed by us. The step number is a function of plate spacing and can be varied in the order of 1, 2, 3 ... depending on the requirement of the observations. To scan one order in wavelength, the plate gap is required to be changed by $\lambda/2$ i.e., the gap should be changed by 2500 Å at the wavelength of 5000 Å or by 512 steps of step size 1. The smallest increment of plate separation adjustments is 0.5 nm or 1/500 of a Fabry-Pérot order at a wavelength of 5000 Å (CS-100 manual). The full drive available for the piezo-electric transducers is $\pm$ 750V (1800nm).

2.2.4 Interference filters

Image quality interference filters were used for the present observations. They are different from the ordinary filters in the sense that they are a single component system in which coatings are deposited on a single surface to eliminate any ghost or multiple imaging. Both exterior surfaces are anti-

Table 2.4: Characteristics of the interference filter used

Type	Image quality Interference filter (Spectro Film Inc.)
Size	Circular (dia = 2 inch)
Peak transmission wavelength	5010 Å
FWHM	20 Å at 20°C for [OIII] 5007 Å
Temperature Coefficient	0.15 Å red shift/°C
Peak transmission	40-50%

reflection coated. The filter bandwidths are chosen to be greater than the FSR of the FPS. Details of the interference filters used are given in Table 2.4.

2.3 Detectors

The efficiency or capability of any detector is governed by its characteristic properties, viz. the quantum efficiency, the dynamic range and the spectral response (Kitchin, 1991).

Until the 17th century the unaided human eye served the purpose of a detector. It is capable of covering the optical range from 4000 Å to 7000 Å. The eye is supposed to be able to resolve angles of one minute of arc but is incapable of storing or making a permanent record of the image. There were instances, thus, of astronomers recording sketches of the eye-witnessed pictures of celestial objects that are bright and large in angular size. In the late

19th century, the art of photography was developed and became the chief detection as well as data acquisition system in astronomy. A photographic film consists of an emulsion of silver halide (mainly bromide) crystals in gelatin, deposited on a plane glass plate or a celluloid sheet in a thin uniform layer. The interaction of the infalling light photons and the emulsion results in the production and accumulation of silver ions where ever the light was incident on the emulsion. Photographic plates are found to be sensitive in the whole of the optical spectrum except in the infrared region beyond 12000 Å. Because of its capability of integrating over a long time, it had proved to be a useful tool for the studies of weak astronomical sources. But a major limitation of photographic plates is its low sensitivity and the complex method involved while analyzing the signal, since the data is not accessible immediately for analysis. The photographic plate is to be processed first and the density is recorded by using a microdensitometer which is then related to the transmittance according to the relation D = −logT, where D, is the density of silver ions formed on irradiation by photons, and T is the transmission of the film. Each plate requires a characteristic curve of density verses logE (transmittance × exposure time) which gives the required conversion factor from density to intensity. Therefore the analysis procedure becomes quite complex.

With the development of technology, photoelectric detectors called photomultiplier tubes (PMTs) were manufactured. The photomultiplier tube exploits the principle of photoelectric effect. When the electromagnetic ra-

diation is incident on a negatively charged electrode (the cathode), photoelectrons are liberated which are then accelerated to a positively charged electrode (the anode). The amplification of the signal in the PMT is achieved by means of electron multipliers called dynodes. Dynodes are given progressively higher positive potentials and are arranged in such a fashion that the electrons leaving one dynode are directed towards the next. Successive multiplications will therefore result in an exponential growth in the signal. The gain in the signal is in the range of 10^6 to 10^8.

The quantum efficiency of the PMTs varies from ultraviolet to far-red and at best it is 20% at 5000 Å. But, the shortcoming of a PMT is that it can sample only an integrated small portion of the sky at a time. Therefore, extended objects such as Planetary nebulae, HII regions and galaxies must be sampled part by part, requiring large amounts of telescope times.

With the aim to combine the spatial recording ability of the photographic plate and the reasonably good quantum efficiency of PMT's, Image Intensifiers were developed. An Image Intensifier is a vacuum tube with two electrodes, a negatively charged electrode, the cathode and a positively charged electrode, the anode. The cathode and anode are kept close together to preserve the spatial resolution. The photoelectrons liberated by the photocathode are accelerated to the anode following paths that are approximately straight lines. The anode is made of a fluorescent material in order to produce visible output. In order to increase the elctron gain, Microchannel Plates (MCPs) are incorporated in the Image Intensifiers. MCPs comprise

Table 2.5: Comparison of the characteristic properties of different detectors

Characteristic property	Photographic plate	PMT	CCD	IPD
Quantum efficiency (visible range)	1%	10-20%	20-70%	10-20%
Dynamic range	~ 100	$\sim 10^6$	$\sim 10^4$	$\sim 10^{5a}$
Spectral response(μm)	0.3-0.7	0.2-1.0	0.4-1.1	0.2-1.0

[a]This is true provided number of counts in each pixel do not exceed 100/s.

of millions of miniature PMTs arranged in two-dimensional array.

Recent developments in the microelectronic technology has led to the advent of digital panoramic two dimensional detectors like charge coupled devices (CCDs) and imaging photon counting detectors (IPCS & IPDs). The spectral response, quantum efficiency and sensitivity of different light detectors are compared in the Table 2.5. In what follows, we give details of an imaging photon-counting detector that is used in our IFPS.

2.3.1 Introduction to Imaging Photon Detector (IPD)

The imaging photon detector (IPD) is a two dimensional sensor capable of detecting a single photoelectron. It consists of a S-20 photocathode, a stack of three microchannel plates and a position sensitive resistive anode. A schematic layout of IPD is shown in Fig. 2.2.

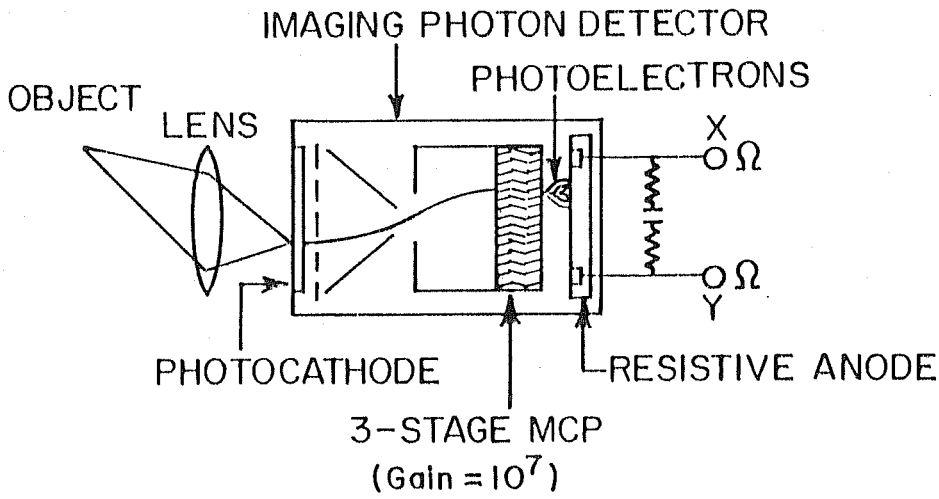

Figure 2.2: A schematic layout of Imaging Photon Detector (from Tsuchiya et al, 1985).

The IPD system comprises of (i) Detector unit and (ii) Processing electronics.

Principle of operation

Photoelectrons released from the photocathode are drawn to the microchannel plates (MCP) by means of the electric field applied across the gap. The cathode is proximity focussed to the MCP. On entering one of the microchannels, a primary photoelectron strikes the channel wall, liberating a shower of secondary electrons which are all accelerated down the channel, hitting the wall and producing further secondary electrons in the process.

The electron gain achieved is up to 10^7 electrons per event. The electrons are drawn by a weak electric field to the resistive anode. The resistive anode has four arc-terminating resistors at the four corners which create the effect of an infinite sheet (for details, Lampton et al, 1979) as shown in Fig. 2.3. When a charge cloud strikes the anode, a fraction of the charge leaves from each of the four corners connected to the virtual earth. The pulses are amplified by fast preamplifiers, shaped and buffered and fed to the processing unit. The electronic processor unit analyzes the signals from the resistive anode and gives the X,Y information along with a strobe pulse to an image acquisition and processing system which can be set to an integration time of our choice. The position of photon event is determined as a function of the amount of

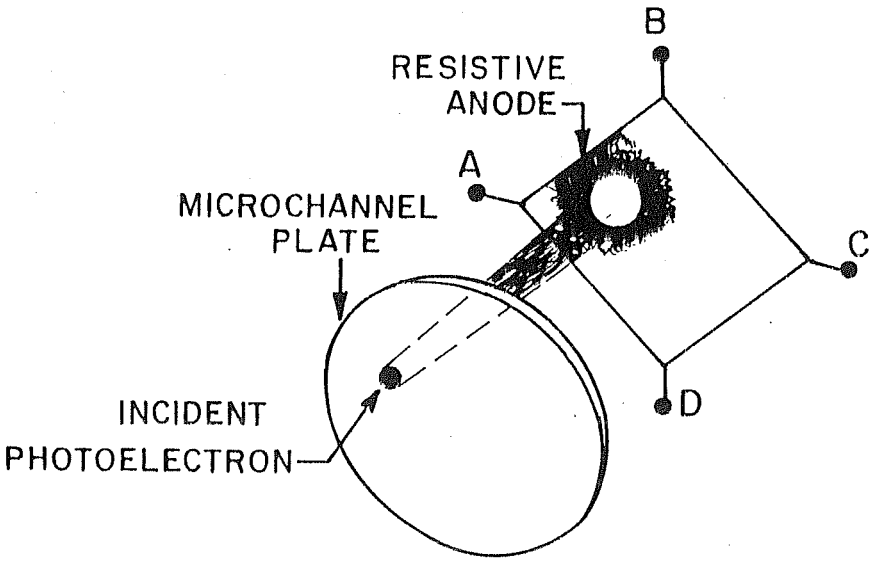

Figure 2.3: A resistive anode (from Lampton, 1981).

current measured at the four corners of the electrodes (I_1 through I_4):

$$X = \frac{I_1 + I_3}{I_1 + I_2 + I_3 + I_4}$$

$$Y = \frac{I_2 + I_4}{I_1 + I_2 + I_3 + I_4}$$

Characteristic features

The limitations on the detector are that there is a dead time of about 7 μs during which the electronic unit analyses the signals and hence no second signal would be allowed. This restricts the count rate to about 1.4×10^5 counts/s on the entire detector. Also, the conductivity of the microchannels limits the maximum counts in a given area of around 60μm to about 100 counts/s. Since IPD, in our case, is used only after a filter and FP in the optical system, this limitation (of maximum count rate) does not affect the observations. There is an uncertainty in the centroiding of an event at the resistive anode which gives rise to the concept of a circle of least confusion and thereby also defines a pixel size for the IPD. Using a chromium positive test target (ruled with different sets of line pairs per mm), we have estimated the pixel size to be about 60μm. For this pixel size, there would be 9×10^4 pixels (300×300 in circular array) associated with the IPD. These characteristic features are summerised in the Table 2.6. The spectral response curve of IPD is shown in Fig. 2.4. Fig. 2.5 shows the resolution versus illuminance for IPD in comparison with a CCD.

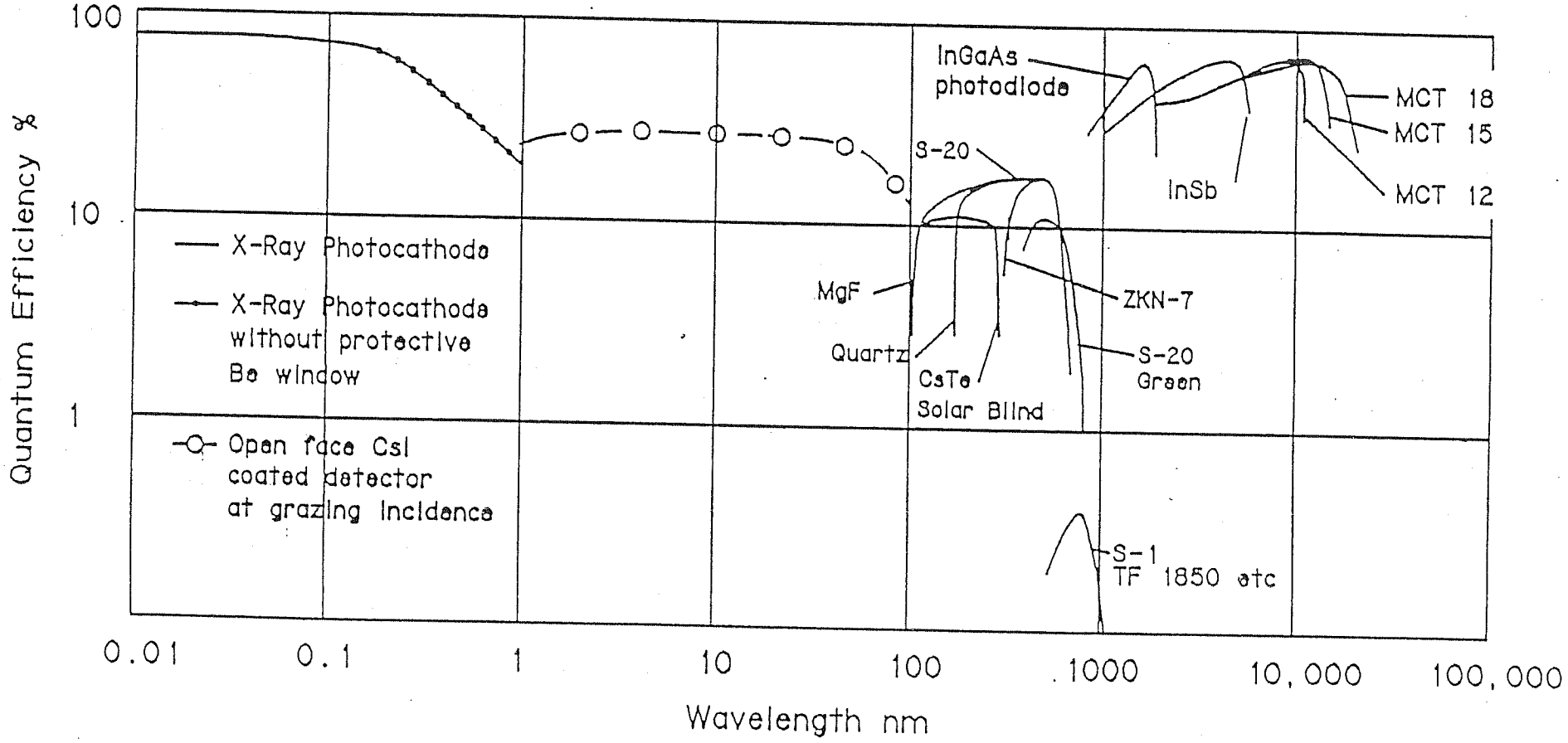

Figure 2.4: Spectral response curve of IPD (marked S-20).

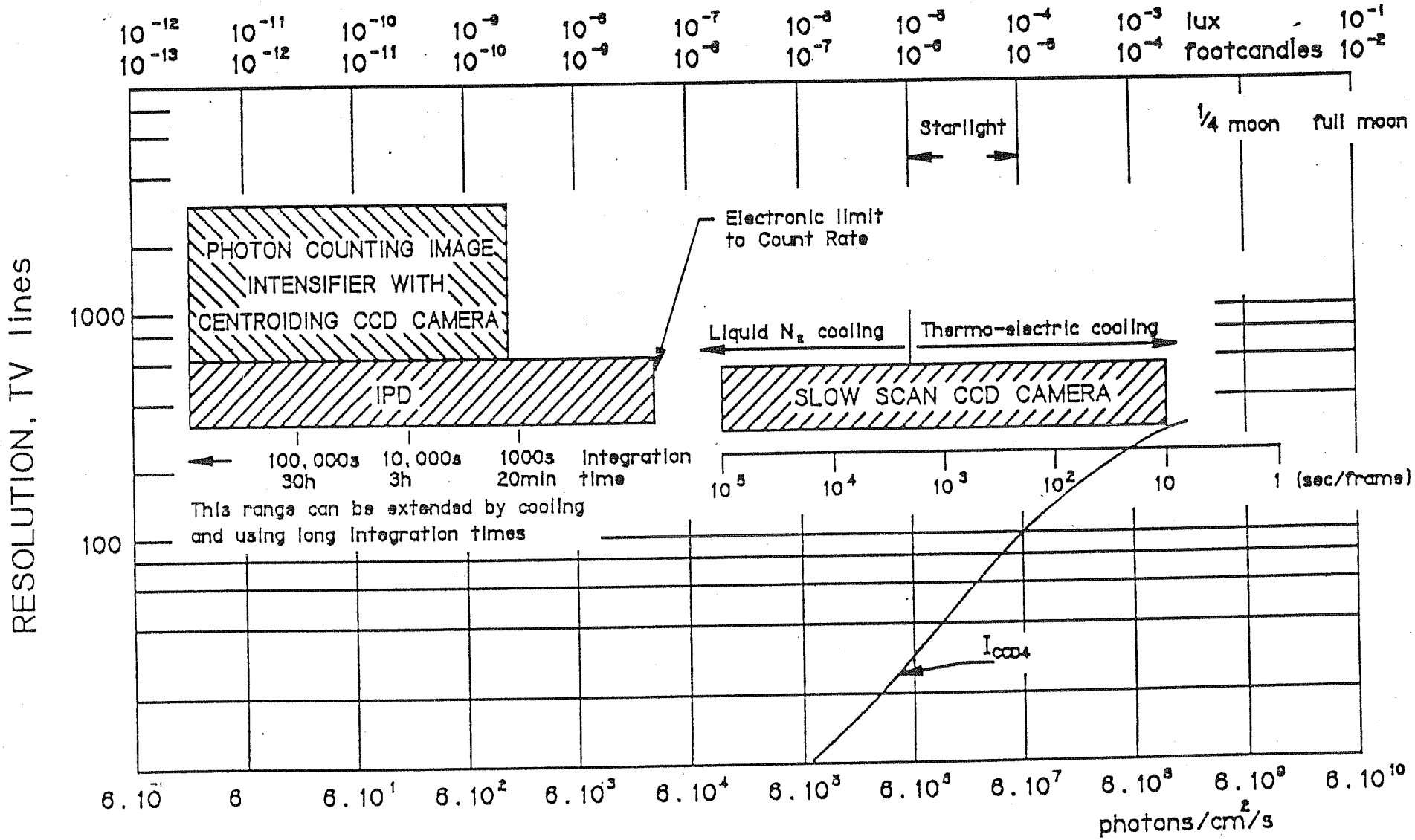

Figure 2.5: Resolution versus illuminance for IPD & CCD

Table 2.6: Characteristics of the IPD

Photocathode	S-20
Active Diameter	18 mm
Quantum efficiency at 5000 Å	18%
Resolution	60μm
Microchannel plate gain	10^7
Maximum Count rate	10^5 events/s
Dark noise at 20°C	4×10^{-3} counts/s/pixel
Total number of pixels	$300 \times 300(9 \times 10^4)$
Dead time	7×10^{-6} s

The optical design chosen by us permits the following spatial resolution for different telescopes: for an image at the f/13 Cassegrain focus of the 2.34m and 1.2m telescope, we obtain 0.41 arcsec and 0.78 arc sec per pixel respectively, whereas for f/11 Cassegrain focus of the 35cm telescope, each pixel corresponds to about 2.0 arcsec.

Sources of noise and pulse height distribution

The pulse height is actually controlled by the MCP voltage and is set by the upper and lower thresholds. The small noise pulses generated by Johnson noise (within the position sensitive anode itself) and electronic noise (generated in the charge sensitive preamplifiers) are rejected by the lower threshold and large pulses such as those generated by coincident events, ions, cosmic rays etc are cut off by the upper threshold. Fig 2.6 shows a typical pulse

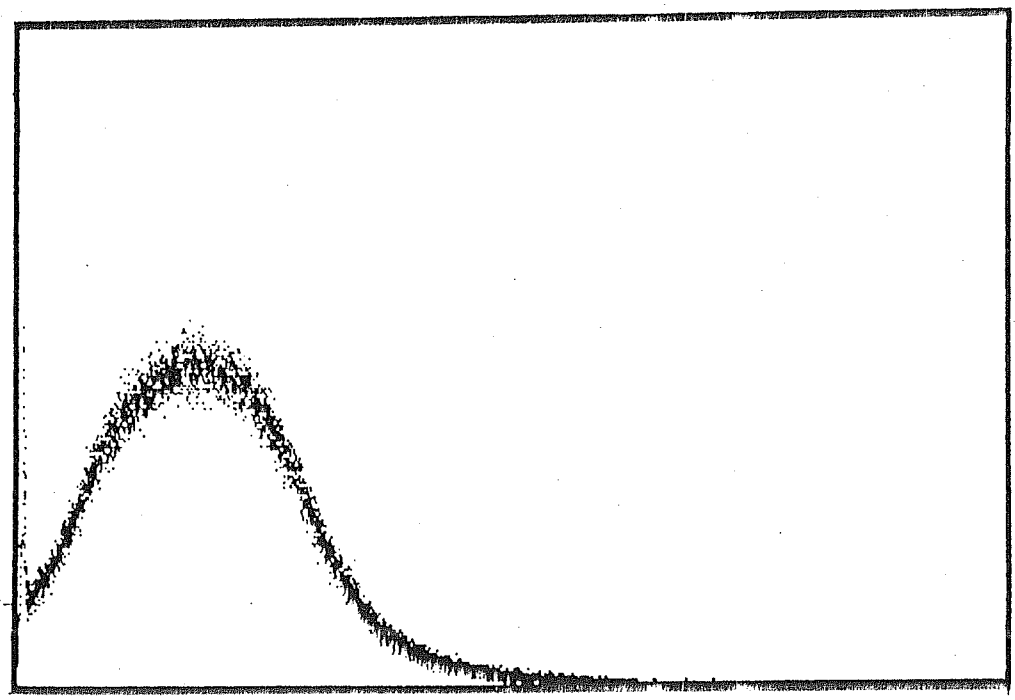

Figure 2.6: Pulse height distribution as obtained for the 18mm IPD in the illuminated condition. The x-axis runs from 0 to 8 V and y-axis shows the number of counts (arbitrary units).

height distribution we have obtained for the 18mm diameter IPD in the detector illuminated condition.

Estimation of Integration times

Theoretical estimates of the integration times required for obtaining reasonably good S/N ratios ($S/N = s \times [t/(s+d)]^{1/2}$, where s and d are source and dark counts per second and t is the time of integration in seconds) for objects of different fluxes in H_α are given in Table 2.7. The transmittivity of the entire instrument is taken to be $\sim 20\%$ and the quantum efficiency of the detector ~ 7 % at $\lambda = 6563$ Å . The fluxes are taken from Kennicutt and Kent (1983) to evaluate the integration time.

A comparison with other types of Imaging detectors

The imaging Fabry-Perot spectrometer 'TAURUS ' developed by Atherton et al (1982) utilises an Imaging Photon-Counting System (IPCS, Boksenberg, 1972) while the recent system developed by Bland and Tully (1989) uses a CCD. IPCS works on a similar principle as IPD except that a videcon tube replaces the resistive anode for position detection (Boksenberg, 1972). IPD is far smaller and lighter compared to IPCS and does not require expensive and clumsy water cooling and focussing solenoid power supplies.

The comparison of IPD with CCD requires comparison of the readout

Table 2.7: Theoretical estimates of integration times for different sources S/N=10 with a 2.3 m telescope using the IFPS

Object NGC	Type	Apparent magnitude	Hα flux (erg cm^{-2} s^{-1} arcsec^{-2})	Integration time (min)
628	Galaxy SA(s)	9.6	9.3×10^{-17}	40
3310	Galaxy SAB(r)	11.2	4.8×10^{-16}	2
3504	Galaxy SAB(s)	10.7	1.4×10^{-16}	25
4736	Galaxy SA(r)	8.1	10.2×10^{-17}	40
4790	Galaxy SB(rs)	12.5	9.5×10^{-17}	40
5055	Galaxy SA(rs)	8.9	10.7×10^{-17}	40
5194	Galaxy SA(s)	8.4	2.2×10^{-16}	8
6853	Planetary Nebula	8.1	1.4×10^{-14}[a]	2

[a]Flux is for the [OIII] 5007 Å line (Barker, 1984) and the integration time is for the brightest portion of a beam $\sim 1'$ only.

noise and the readout time of CCDs with the dark noise and the dead time of the electronics in IPDs respectively. A detailed discussion with respect to this can be found in the literature (Mackay 1986; Jenkins 1987; Bland and Tully 1989). Currently available high resolution CCDs have readout noise of a few electrons per pixel but a readout time of a few tens of seconds (typically 60s). The dark noise in the IPD is typically 4×10^{-3} counts/s/pixel at 20° C, while the dead time is $\sim 7\mu$s. Whereas IPD has limitations on the maximum count rate (due to the dead time) of a few times $\times 10^5$ counts/s and a pixel count rate of a maximum of $\sim$ 100 counts/s (due to the conductivity of microchannels), the CCD is free from such restrictions. Bland and Tully (1989) showed that in order to obtain a $(S/N)_c$ for CCD greater than $(S/N)_p$ for the IPD with the assumptions: (i) all the signal resides in the emission line; (ii)background sky noise is low and (iii) Signal/Noise > 3, the following inequality should be justified,

$$(S/N)_p \leq 2.3\sqrt{1 + (\tau_R/\tau_o)} \tag{2.21}$$

where τ_R is the read out time and τ_o is the exposure time.

From eqn. 2.21, it is clear that for a short readout time CCD seems to be a better choice whereas for a short exposure time photon-counting detectors are more suitable. It therefore appears that the CCD basically scores over the IPD for long exposure times and hence for faint sources in the case of a single interferogram. Also, it is possible to have rapid scanning

in wavelength with photon counting device which will result in averaging the fluctuations in atmospheric transparency. But, for a CCD it is required to integrate for a longer time at each gap spacing till the photon statistics exceed readout noise. Therefore slow scanning only is possible in CCD's allowing observations covering only a few steps (Bland & Tully, 1989). Therefore, for scanning FPS, IPD is still preferred to the CCD.

2.4 Image data Acquisition System

The block diagram of the Image data acquisition system is shown in Fig. 2.7. The IPD sensor outputs A, B, C, D, are connected to the electronics processing unit (supplied by ITL, England). The electronics processing unit generates the X-Y coordinates information, for each photoelectron event detected in digital form, ten bits each of X and Y, together with a strobe pulse. The analog X-Y outputs from the electronics unit are fed to a storage oscilloscope to see the individual events in real time as a check that the detector is operating correctly.

The digital image is acquired and stored by the frame store unit using the IFS216 software (supplied by ITL). The image is displayed on the high resolution VGA monitor. The software enables the setting up of the required integration times for each frame. A micro-processor based computer card is developed by us and fixed in the PC computer for the operation and control of the system as per the requirement of the observations. It has the following

in wavelength with photon counting device which will result in averaging the fluctuations in atmospheric transparency. But, for a CCD it is required to integrate for a longer time at each gap spacing till the photon statistics exceed readout noise. Therefore slow scanning only is possible in CCD's allowing observations covering only a few steps (Bland & Tully, 1989). Therefore, for scanning FPS, IPD is still preferred to the CCD.

2.4 Image data Acquisition System

The block diagram of the Image data acquisition system is shown in Fig. 2.7. The IPD sensor outputs A, B, C, D, are connected to the electronics processing unit (supplied by ITL, England). The electronics processing unit generates the X-Y coordinates information, for each photoelectron event detected in digital form, ten bits each of X and Y, together with a strobe pulse. The analog X-Y outputs from the electronics unit are fed to a storage oscilloscope to see the individual events in real time as a check that the detector is operating correctly.

The digital image is acquired and stored by the frame store unit using the IFS216 software (supplied by ITL). The image is displayed on the high resolution VGA monitor. The software enables the setting up of the required integration times for each frame. A micro-processor based computer card is developed by us and fixed in the PC computer for the operation and control of the system as per the requirement of the observations. It has the following

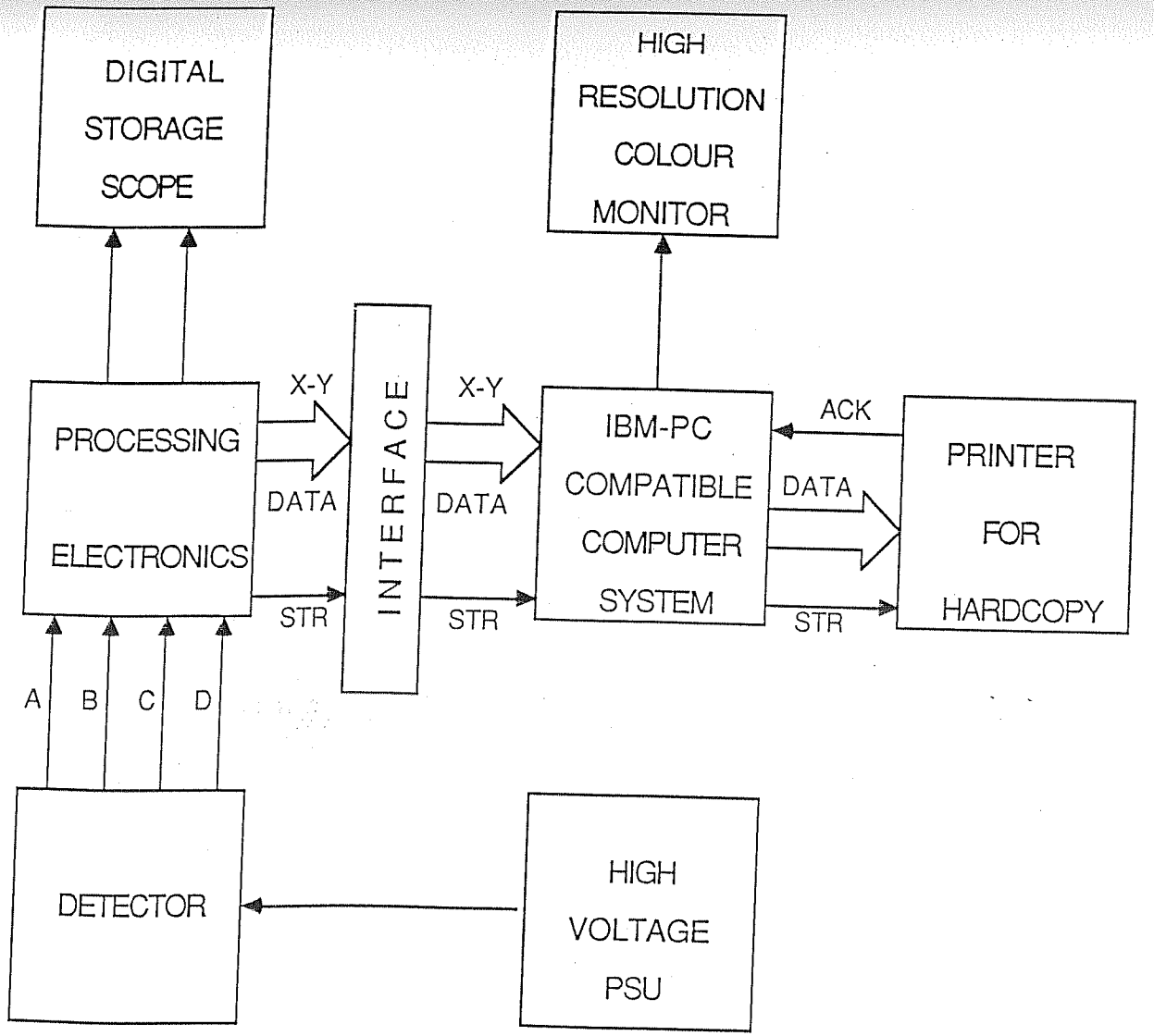

Figure 2.7: Block diagram of Image Data acquisition system

functions:

- Firstly, it inputs the wavelength of interest in order to choose the number of steps required for scanning through one FSR.

- The step size required for scanning of the étalon is given as an input parameter through the terminal.

- Next, it feeds the CS-100 unit with the required value of the step-size and waits for the acquisition of the image at each step.

- Immediately after the acquisition of the image is over, it sets the CS-100 to the next step and again an image is acquired and so on over one FSR.

- After completion of the scan for one FSR, the CS-100 unit is restored to its normal position.

2.5 Instrument Performance

A photograph of the completed IFPS set up in the laboratory with the CS-100 and detector (IPD) system is shown in Fig. 2.8. The performance of the instrument is tested by obtaining interferogram of standard laboratory source using the zinc spectral lamp , ZnI 4684.14 Å in green region and NeI 6598.9 Å in the red region. Fig. 2.9 shows interferogram in the zinc line. A radial scan taken from the centre of the interference fringes gave the instrument profile as shown in Fig. 2.10.

Figure 2.8: IFPS set-up in the laboratory.

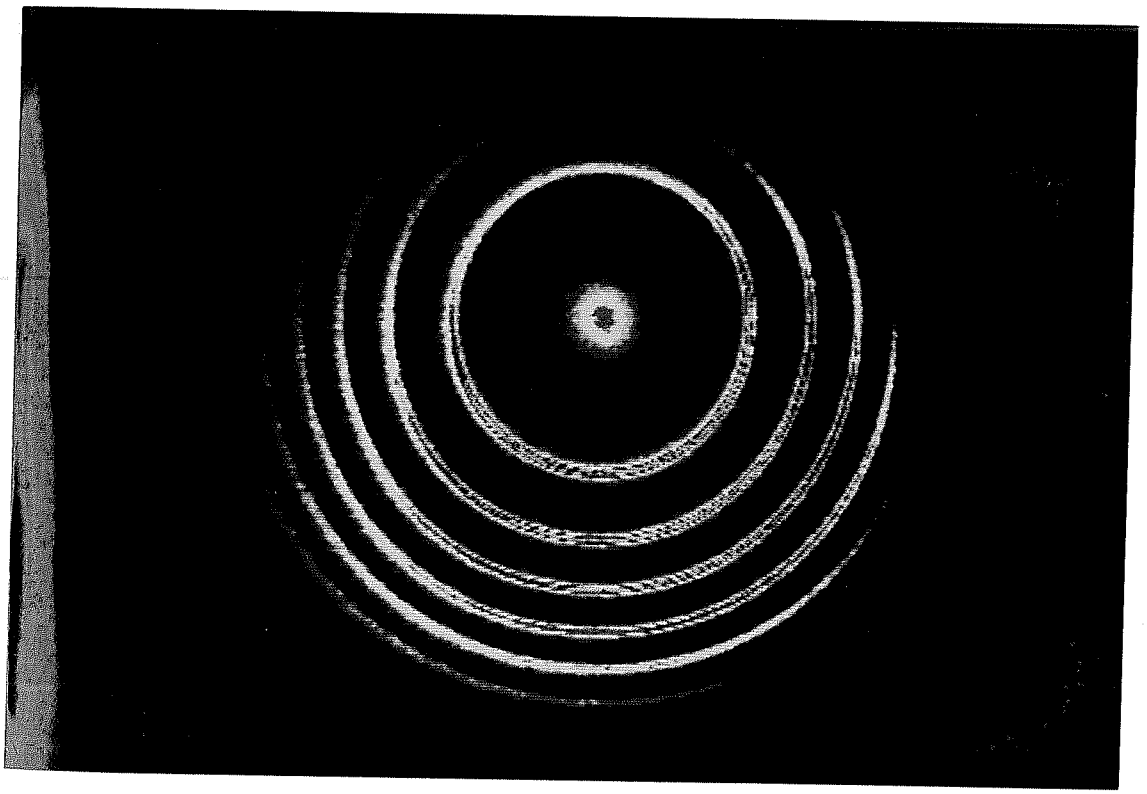

Figure 2.9: Interferogram obtained in Zn I line, λ=4684.14 Å, with integration of 1 minute.

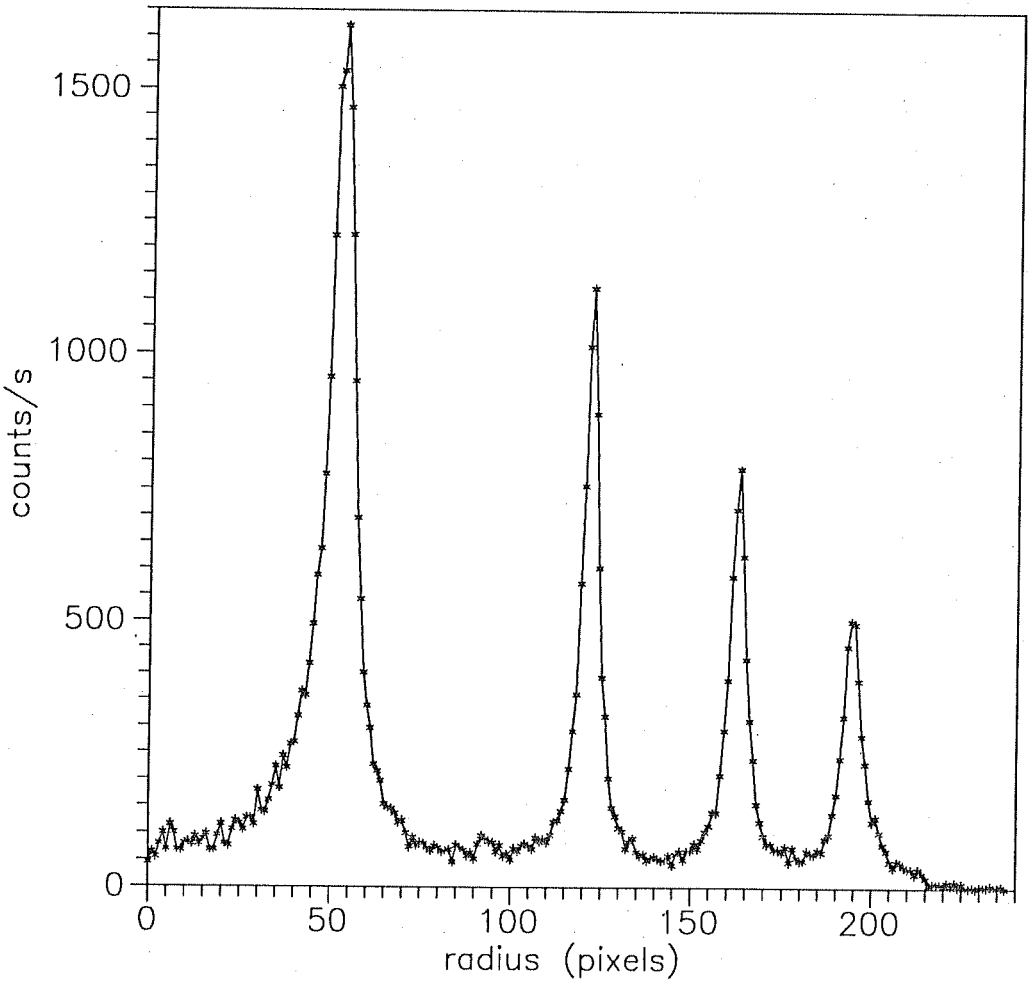

Figure 2.10: Radial scan from the centre of the interference fringes in Zn I line, λ=4684.14 Å

The reflective finesse for λ =5007 Å, with reflectivity of 93% can be calculated from eqn. 2.5 to be 43.3. Considering the quoted plate flatness to be $\lambda/100$, N_{DC} is obtained as 50 from eqn. 2.9. Since the defect due to microtopographic polishing errors is not specified by the manufacturer, the defect finesse, N_{DG} is found to be 21 from eqn. 2.10, considering the error to be $\lambda/100$ and N_{DP} to be 150, plate parallelism being maintained at $\lambda/2000$ (eqn. 2.11).

Therefore, the overall defect finesse from eqn. 2.14 is found to be in the range $21 \leq N_D \leq 50$. The aperture finesse N_A is found to be 195 (eqn. 2.13) by taking solid-angle subtended by the aperture at a pixel to be $\sim 1.938 \times 10^{-5}$ steradians. The effective finesse from eqn. 2.14 is then found to be $\sim$ 32, which is in good agreement with the observed finesse $\sim$ 30 found after deconvolving with the aperture function.

A profile is obtained at a single pixel using Ne I 6598.5 Å line as shown in Fig. 2.11.

Observations made on certain HII regions (viz. Orion and Trifid) and Planetary nebulae (viz. Dumbbell) agree well with the theoretical estimates for the performance of the instrument shown in Table 2.7.

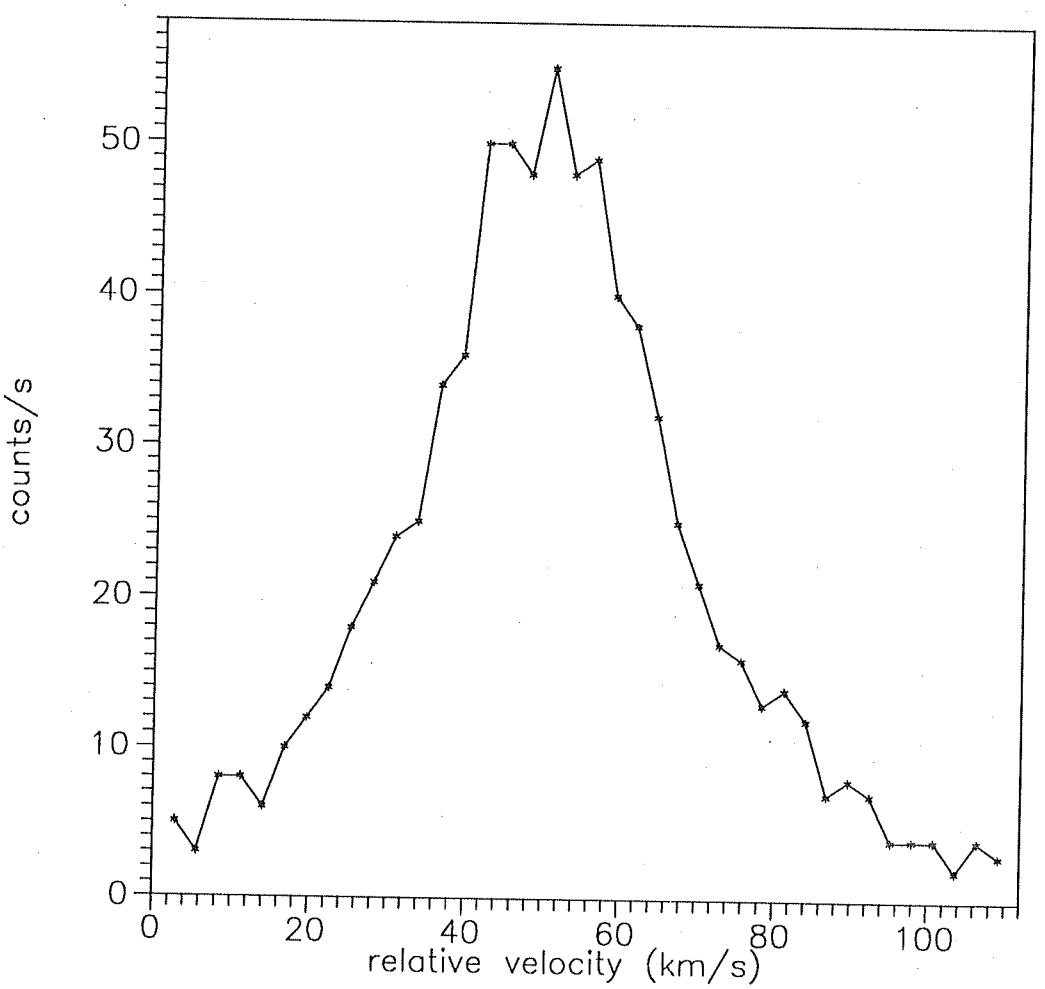

Figure 2.11: Line profile at a single pixel in neon line, λ=6598.5 Å.

Chapter 3

OBSERVATIONS AND DATA ANALYSIS

3.1 Observations

Observations were made on two HII regions, Trifid nebula , ($\alpha(1950) = 17^h58^m9^s$, $\delta(1950) = 23^o2'$) (May 21, 1990) and Orion nebula ($\alpha(1950) = 5^h\,32^m\,54^s$, δ (1950) $= -5^o\,25'$) (February 1 to 5, 1992) at Gurushikhar, Mt.Abu. The instrument, namely, the Imaging Fabry-Perot spectrometer (IFPS) was attached at the $f/11$ Cassegrain focus of the 14" C-14 Celestron telescope. A justification for the use of a small-sized telescope is in order. According to the optical extension conservation principle, the product of the area of the telescope primary and the solid angle subtended at the aperture ($S \times \Omega$) should remain constant. For a small telescope, therefore, the loss in collecting area will be exactly compensated by the increase in the observed

angular field. Since our aim is to make observations of an extended region in the HII regions, this trade off between higher spatial resolution in favour of the large field of view is justified. Besides, the non-availability of sufficient amount of observation time on large telescopes due to weather related problems also force us to forgo the possible spatial resolution permitted by the atmospheric seeing, viz. 1 or 2 arc sec. Table 3.1 gives some physical parameters on some well known HII regions.

The following section gives details of the observations made on the two HII regions and the method of data analysis.

3.1.1 Orion Nebula

Orion Nebula (M42; NGC 1976) is the nearest HII region and as such has attracted the attention of observers in the past as well as in the present. It offers a veritable testing ground for various theoretical mechanisms proposed to understand the physics of HII regions. Interferograms were obtained on the Orion Nebula in the emission line of [OIII] 5007 Å centred around the trapezium stars (θ^1 Ori). Scanning of the etalon ET50 (Table 2.1) is done by changing the plate spacing in equal increments and thirty three interferograms were obtained covering about 1.55 Å, one FSR corresponding to 3 Å. We could not cover the entire FSR due to bad weather. The spectral resolution was 6 km/s with an accuracy of 2 km/s in velocity and spatial resolution was 4 arc sec with a field of view of 10.5 arc min. Interferograms

Table 3.1: Properties of five typical HII regions (adopted from Eric Chaisson and extended)

Name of Nebula	Messier Number	position α h m δ o /	Constellation	m_v†	Diameter arc min(pc)	Distance pc	r_o‡ pc	n_e§ cm^{-3}	Mass $M_\odot$	Electron Temp. K	Turbulent velocity km/s	H_e^+/H^+ %
Orion	M42	05 32.9 -05 25	Orion	4.0	35(5)	460	0.3	2,000	10	9,000	10	9
Trifid	M20	17 58.9 -23 02	Sagittarius	8.5	15(4)	1994	2.5	100	150	8,200	7	10
Lagoon	M8	18 01.6 -24 20	Sagittarius	5.8	25(9)	1074	1.2	400	60	7,500	9	9
Eagle	M16	18 16.0 -13 48	Serpens	6.4	12(6)	2454	3.7	100	600	8,000	12	6
Omega	M17	18 18.0 -16 12	Sagittarius	7.0	20(9)	2147	1.5	800	300	8,700	17	10

†integrated
‡Stromgren Radius
§electron density

were also obtained from a zinc spectral lamp on the ZnI line at the wavelength of 4680.14 Å for calibration purpose in order to (i)check the stability of the instrument during observations and (ii)to obtain the standard radii of the fringes at that line. Fig. 3.1 shows a photograph of Orion Nebula (taken from Shu, 1974).

3.1.2 Trifid Nebula

Trifid nebula (M20; NGC 6514) stands out as the brightest after Orion nebula and the most symmetric HII region observed ever inspite of the three spectacular dust lanes overshadowing its glory. It is classified as an emission and reflection nebula in Sagittarius. A single interferogram was obtained in [OIII] 5007 Å line using an optically contacted etalon with a FSR of 1.25 Å ($\sim$ 75 km/s at 5007 Å). Integration time was 20 minutes. The field of view covered was $\sim 24'$ giving a sky angle of $\sim 4.6''$/pixel on the IPD. Fig. 3.2 shows the Trifid nebula. We could not carry out the scanning at that time as we had used the optically contacted etalon which involves cumbersome pressure scanning. Our attempts later, on large telescopes, using piezo scanned etalons met with little success due to bad weather condition. Nevertheless, the interferogram obtained by us earlier contained considerable information; and to our knowledge it is the first ever interferogram covering such a large region in this nebula.

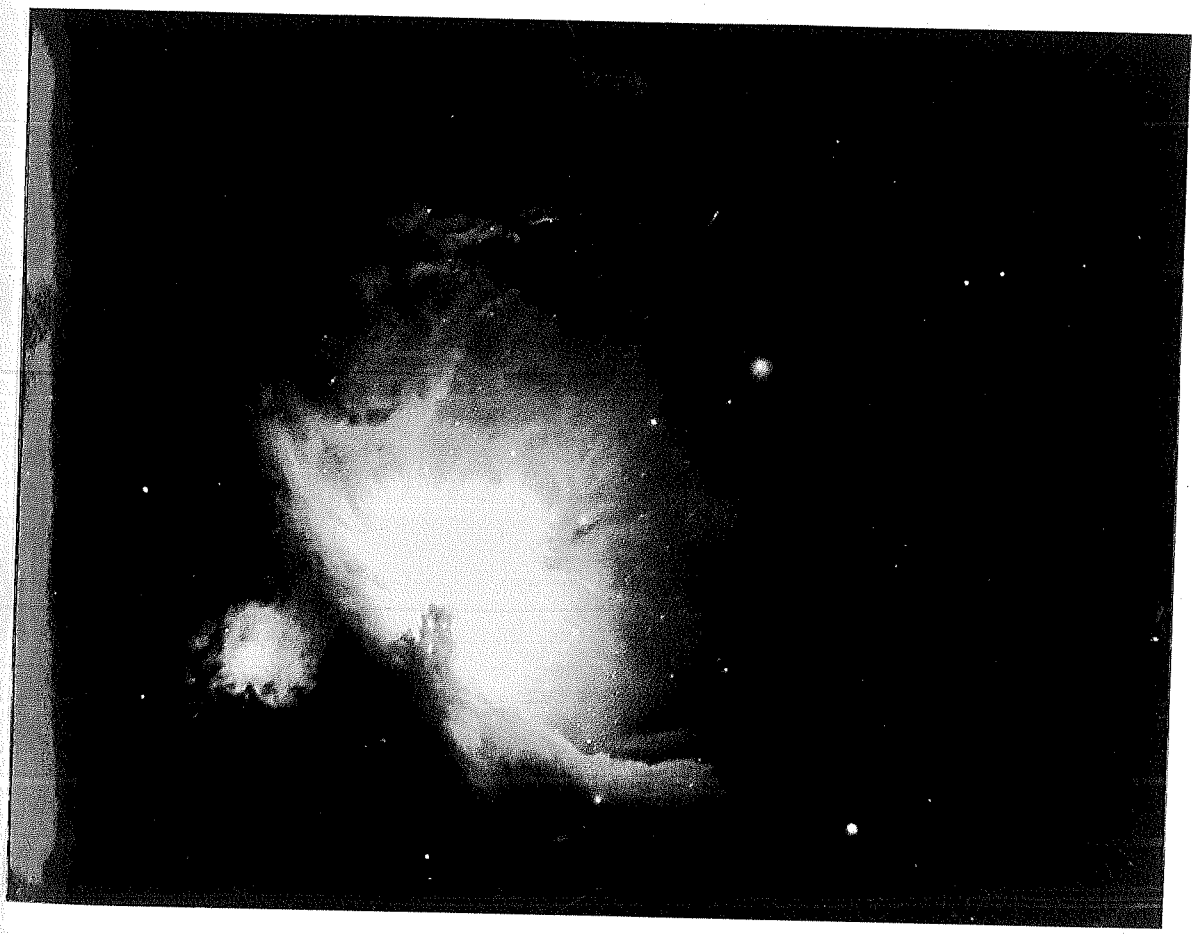

Figure 3.1: The Orion nebula (from Shu, 1974)

Figure 3.2: The Trifid nebula obtained by combining images in blue, green, and red filters (from Rudolph, 1988)

3.2 Data analysis of the FP interferogram images

The imaging data acquired is in digital (binary) form: ten bits of X and ten bits of Y with 512×512 pixels with the intensity at each position given by 16 bits.

3.2.1 Smoothing the data

A set of softwares were written to extract the kinematic information from the interferograms. Firstly the images are smoothed for random statistical noise by using a 3×3 convolution matrix

$$\begin{bmatrix} -1 & -1 & -1 \\ -1 & -1 & -1 \\ -1 & -1 & -1 \end{bmatrix}$$

This process essentially averages the counts of nine pixels in an array of [3 × 3] and assigns the resulting number to the central pixel. The next step in the process of data analysis is to find the exact coordinate of the centre of the standard source interferogram. For this, an approximate centre is obtained by reading the [X,Y] coordinates from the screen of the VGA monitor. A software is developed and used to find the maximum intensity points cutting across the fringes by searching along the radius vectors starting from the approximate centre of the interferogram in all directions (0°to 360°) by adding the data points in a sector of 5° to increase the signal to noise ratio. Using these maximum intensity points, the equation of circle is fitted by the

method of least squares. Thus in the general equation of a circle,

$$x^2 + y^2 + 2gx + 2fy + c = 0$$

where g, f and c are constants, the position $(-g, -f)$ gives the actual centre of the interferogram. The radius of each fringe of the standard interferogram is thus obtained.

3.2.2 Calibration

The purpose of the standard interferogram is to calibrate the fringe constant involving the focal length of the camera or imaging lens f_{cam} and the gap of the etalon, t. Usually these two parameters are supplied by the manufacturer. However, small errors in these might lead to systematic errors in the fringe positions.

From eqn. 2.1, we get for central fringe,

$$2\mu t = n_o \lambda$$

for p^{th} fringe

$$2\mu t cos\theta_p = n_p \lambda$$

Subtracting the two equations, we get

$$2\mu t(1 - cos\theta_p) = (n_o - n_p)\lambda$$

θ being small, we can write this as

$$\mu t\theta_p^2 = (n_o - n_p)\lambda$$

For air gap μ=1; and writing $(n_o - n_p)\lambda$=pλ and $\theta_p = r_p/f_{cam}$

Therefore,

$$tr_p^2/f_{cam}^2 = p\lambda$$

$$r_p^2 = \frac{f_{cam}^2 p\lambda}{t} + c \tag{3.1}$$

where c is a constant which accounts for the fractional order and r_p is the radius of the p^{th} ring. The plot of r_p^2 vs p (Fig. 3.3) gives a straight line with slope or the fringe constant

$$m = \lambda f_{cam}^2/t$$

From this we can obtain,

$$f_{cam} = \sqrt{\frac{t \times m}{\lambda}} \tag{3.2}$$

and the effective focal length of the camera lens can thus be obtained.

The calibration fringes were obtained at three different positions of the etalon spacing, one in the beginning of the scan (step 1), one in the middle (step 15) and one in the end (step 33).

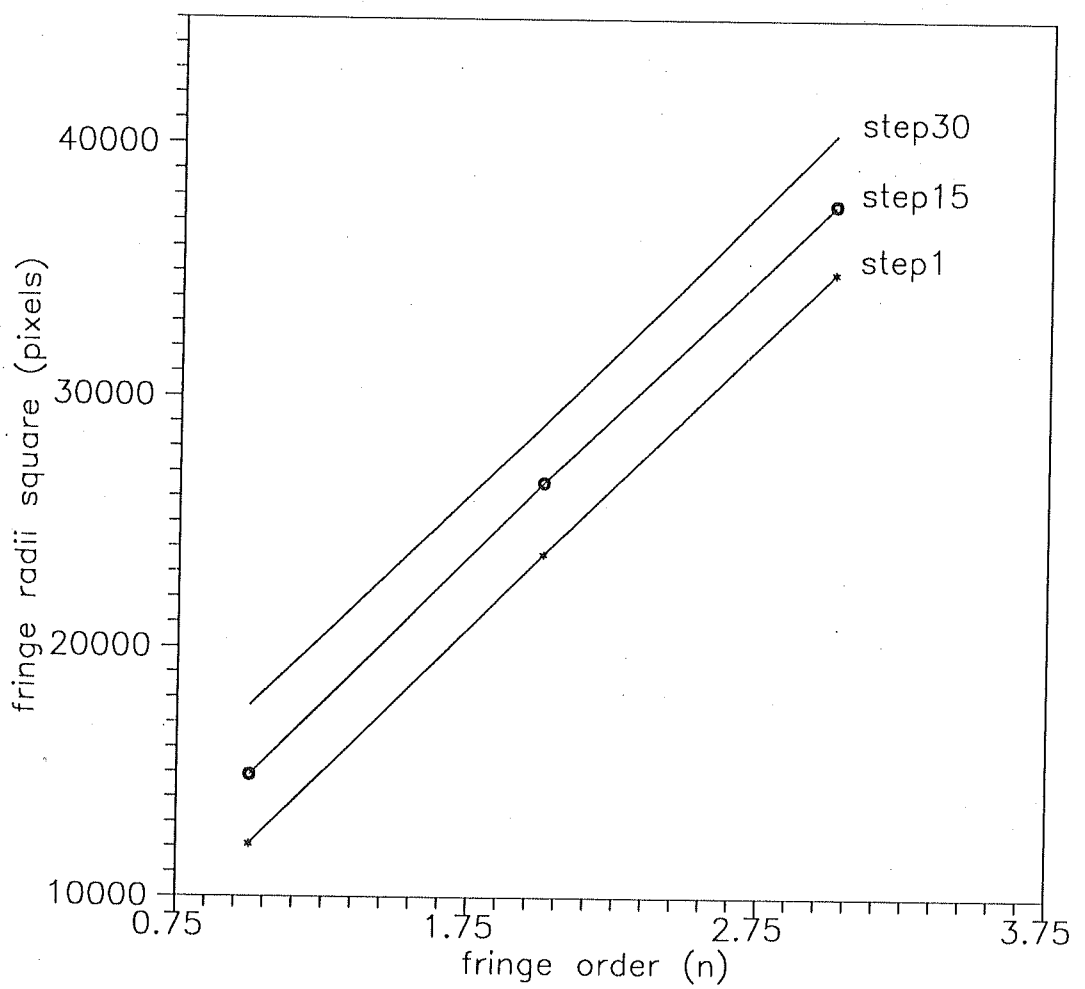

Figure 3.3: Radius square versus order of fringe

The slope m and intercept c at these positions are found from the Fig. 3.3 and used to calibrate the slopes and intercepts of the intermediate fringes. The value of $t(gap)$ at each step is evaluated then. This is done by first finding the number of steps to scan one free spectral range of the etalon. In order to scan the etalon (ET50) by one FSR (3 Å) at λ 5007 Å we need to change the gap t by $\lambda/2$ (=2503.5 Å). This was done in about 64 steps with each step corresponding to a change in t of about 39 Å . Thus after the first stage, the plate separation corresponds to $t = t_o + 39$Å , where t_o is the initial gap. Substituting the values of m, c and t in eqn. 3.1, the corresponding values of radii of fringes are obtained at each value of the gap/separation of the etalon plates.

3.2.3 Determination of line of sight or radial velocities

Any deviation in the line-of-sight or radial velocity at any point on the sky due to the kinematics of the nebula changes the shape and position of the object fringes in comparison to the standard fringes. Thus a redward shift in velocity will result in contraction whereas a blueward shift will result in expansion of the fringes. A software is developed and used to first scan the object interferograms starting from the proper centre radially in all directions and adding the photon counts in a sector of 5^o in order to improve upon the S/N ratio. From the constructive interference condition, for i^{th} fringe,

$$2\mu t cos\theta_i = n\lambda$$

and since $\tan\theta_i \sim \theta_i \sim r_i/f_{cam}$, we get,

$$r_i{}^2 = 2f_{cam}^2 - \frac{f_{cam}^2 n\lambda}{\mu t}$$

The difference of the squares of radii of two adjacent fringes is thus given as

$$r_{i+1}{}^2 - r_i{}^2 = \frac{f^2\lambda}{\mu t}$$

which is a constant. The difference between radii of adjacent fringes corresponds to the free spectral range of the FP. This gives the calibration factor for converting the radii into wavelength units. Since the standard fringes are obtained in the zinc line at $\lambda = 4680.14$ Å, corresponding correction factor is applied for the observed wavelength λ =5007 Å. The shift in wavelength ($\Delta\lambda$) from the standard line is then obtained. Finally from the Doppler shift formula

$$v/c = \Delta\lambda/\lambda$$

the relative radial velocities are calculated.

It should be mentioned here that the radial velocities obtained are not absolute values but are only relative. However, this will not affect the understanding of the internal kinematics of the nebula, since we consider only the difference in the radial velocities on the nebula with reference to a fixed point on it.

Radial velocity profiles are generated for more than 2000 positions on the Orion nebula. In general, the profiles looked asymmetric and broad-

winged which necessitated us to resolve them into the constituent gaussian profiles. The profile at each position is fitted by the appropriate number of gaussians (usually and in most cases two) using a multigaussian fitting package (Anandarao and Suhasini Rao, 1985) to obtain the peak position, FWHM and amplitude of the individual gaussian components of the composite fringe profile at any given position. Quite obviously, any multigaussian fitting software cannot give unique results. However, in some cases atleast, prior information about the object would be of great help in order to check the meaningfulness of the solution. Analysis of the data is done for two types of studies: (i) involving general velocity pattern in which the relative velocities so obtained are mapped to get iso-velocity contour maps. The contours are generated using a readymade software package 'Surfer'available on IBM-PC (Golden softwares) and (ii)statistical analysis to study the fluctuations of velocities in a turbulent H II region. The spatial resolution ($\approx$ 2 pixels) in our observations on Orion nebula is about 4 seconds of arc which corresponds to a distance scale of 0.0087 pc while in the case of Trifid, it is about 9.2 seconds of arc corresponding to 0.0058 pc.

3.2.4 Errors in data reduction

The errors involved are of two types (i) systematic errors and (ii) random errors. The following section gives the details of the errors and their estimates.

Systematic errors

The main source of error is due to the instability of the FP etalons. The plate parallelism of the FP etalons is maintained by the servo-control system which utilizes a ceramic reference capacitor. There is a possibility that the value of the capacitance is changed due to change in any one of the physical environmental parameters, viz. pressure, temperature and humidity. This will be reflected in the line profile of the instrument which shows a drift in the peak position. Therefore, to keep a check on such spurious changes, calibration scans are taken from a standard spectral lamp several times during the course of the observations. It has being verified in the case of central spot scanning method that during a scan of about 3 minutes duration, for one order of sampling with 200 sampling points, the departure was 0.015 km/s (Banerjee, 1990). Further, the FP resolution $\delta\lambda$ is 0.1 Å which corresponds to about 6 km/s. This reflects an error in the profile widths of about 3.3 km/s. The velocity position errors (in radial velocities) corresponds to about 2 km/s.

Random errors

In any photon counting device, the S/N ratio depends on the statistical fluctuations in the incident beam of photons. The Poisson distribution is a good approximation of these fluctuations. Therefore, if g represents the average number of photon events in a unit interval of time, the probability of

observing k counts in that particular time interval is given as (Young, 1974)

$$P_g(k) = \frac{g^k e^{-g}}{k!}$$

The standard deviation (i.e., noise) of this distribution is given as $\sqrt{g}$.

Therefore,

$$S/N = g/\sqrt{g} = \sqrt{g}$$

In the present high-resolution spectroscopic observations, the noise is mainly detector-limited as the sky noise can be neglected in most cases. The dark noise over the entire surface of the detector was found to be about 300 counts/s at 20°C.

Errors in Data reduction

The line profiles are fitted with the appropriate gaussians using the multi-gaussian fitting package. But the solution is not unique and it is possible to make two different fits with a different set of the parameters (amplitudes, position and FWHM). It is found that this will involve basically an error in the estimation of amplitude, peak position, half-width values of about 10%. The searching and locating of the intensity maxima and finding the exact centre of the interferogram by the least square method results in an error of approximately $\pm$ 1 pixel which corresponds to an error in Doppler velocities of $\pm$ 2 km/s.

Chapter 4

VELOCITY FIELD STRUCTURE IN THE ORION NEBULA

4.1 Introduction to the Orion nebula

The Orion Nebula (M42, NGC 1976) is the closest HII region located at a distance of 460pc (Allen, 1973). Embedded in the nebular region are the multiple OB star complexes, θ^1 Ori (Trapezium stars) and θ^2 Ori. The four bright stars in the Trapezium are designated as A, B, C and D in order of right ascension. θ^1 C Ori is supposed to be the principal ionizing source for the nebula with visual magnitude of $\sim$ 5.1 and spectral type O6p. Further, Orion offers maximum surface brightness (emission measure $\sim 8\times10^6$ pc/cm^6, Osterbrock, 1974) and thus providing a good opportunity to study the physical processes taking place in the HII regions in general. Table 4.1

Table 4.1: Ionizing stars in Orion nebula

star	spectral type	T_{eff} K	m_v	radial velocity km/s
θ^1 Ori A	B0.5V	27,000	6.8	24.0
θ^1 Ori B	B3	18,800	8.1	28.0
θ^1 Ori C	O6p	37,500	5.1	33.4
θ^1 Ori D	O9.5V	31,000	6.7	31.0
θ^2 Ori A	O9.5Vp	31,000	5.1	35.6
θ^2 Ori B	B0.5Vp	27,000	6.4	28.5

gives some physical details regarding the prominent stellar sources in Orion.

In this chapter we give details of the results of the observations made on the Orion nebula and discuss the major results obtained. As mentioned earlier, the main aim for the present work has been to understand the velocity field structure over an extended region on the nebula, and to study the velocity field across certain well known features observed in the nebula, viz. the 'bar' ionization front, 'the dark bay' and the molecular cloud region as shown in the Fig 4.1.

Our aim is also to comprehend our results on the velocity field in the light of those on other parameters like density, temperature and intensity obtained using different techniques at different wavelength regions (Infrared: Stacey et al, 1993; Radio: Johnson et al, 1983; and optical: Fischel-Feibelman, 1973, Pogge et al, 1992). Further, the recent optical images of the nebula

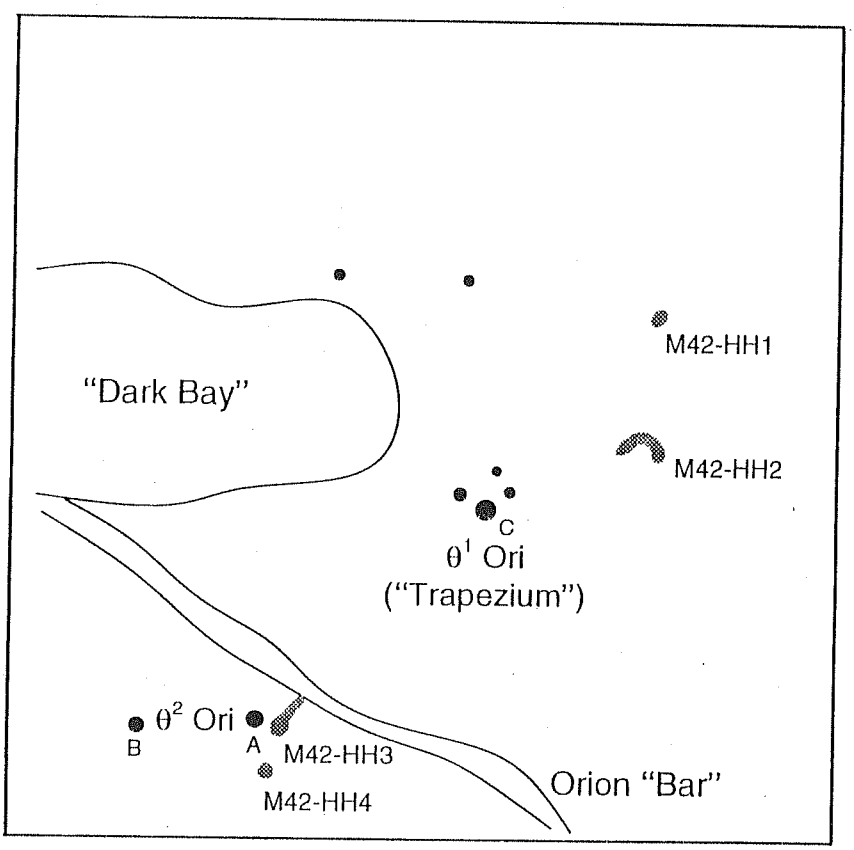

Figure 4.1: A schematic of Orion nebula, M42 showing important features(adapted from Pogge et al, 1992)

obtained by Hubble space telescope (Hester et al, 1991) at the high spatial resolution resolved some more new sources (viz. jets, HH objects) which were not detected in earlier studies due to the lack of adequate resolution. Therefore it is our attempt to understand the kinematics of the gas about these features. In this chapter we discuss in detail the present work with a brief description of the studies made in the past on the Orion nebula.

4.2 Earlier studies

4.2.1 Kinematics

In the past, several studies have been made to determine the radial velocity structure of the brighter portions of the Orion Nebula. The earliest and the most detailed kinematic studies were made by Wilson et al (1959). They observed the emission lines of [OIII] 5007 Å, [OII] 3726 Å and Hγ 4340 Å using multi-slit spectroscopy covering the central bright portion of about $4' \times 4'$ around Trapezium stars. They have shown that there was variation of widths and structures of the lines across the Nebula and also splitting of [OII] and [OIII] lines was observed in certain regions. Spectroscopic observations by Meaburn(1977) also showed splitting of [NII] line in certain regions. More studies made by using Fabry-Pérot Spectrometer (Meaburn 1971; Goudis and Balick 1980; Hippelein and Munch 1983; Smith and Weedman 1970; Dopita et al, 1973; Hanel, 1987) and echelle systems (Fountain el al, 1979; Hufson et al, 1981; Clayton et al, 1985; Meaburn, 1984) showed that the velocity field

structure in the Orion nebula is very complex. Spectroscopic observations were also made at other wavelengths like radio (Pankonin et al 1979, Goudis et al, 1984) and infrared wavelenghs (Stacey et al, 1991; Genzel et al, 1989). As mentioned earlier, these studies did not have adequate spatial or spectral resolution or were limited by the instrument used (i.e., slit spectroscopy). The high spatial and spectral resolution studies made by Castañeda covered only limited regions (along the length of the slit) especially around θ^2 A Ori. In the present studies these problems are overcome by making observations on an extented region with reasonably good spatial and spectral resolution.

4.2.2 Turbulence

von Hoerner (1951) was the first to attempt an interpretation of the random motions observed in Orion in terms of turbulence using the data of Campbell and Moore (1918). His studies showed that the standard Kolmogorov relation for the Structure function, $B(r) \propto r^{\frac{2}{3}}$ was satisfied. Later attempts were made by Courtes (1955) and Pikel'ner and Shain(1954). But the quality of their data did not allow for any definite conclusion.

It was Munch (1958) who then using the data of Wilson et al (1959) studied the turbulent motions of Orion and found that the Kolmogorov relation was not satisfied. He argued that the failure of the Kolmogorov law could be due to the presence of compressibility of the nebular gas. But, some doubts were raised much later (Castañeda, 1988) since the analysis was based on

selecting the maximum intensity values without considering the shape of the line profile or accounting for multiple velocity components which could be possibly present in the profile. Castañeda's recent analysis with high resolution of the structure function for the study of turbulence showed variation with the size parameter in the value of the expected slope (0.66). It was argued that this could be due to the energy source driving the turbulence being input at several scales.

With the large number of well distributed data points obtained in our obervations, a better estimate of the statistical functions can be made for the sudy of turbulent motions.

4.3 Present studies

Fig. 4.2 shows a mosaic of four interferograms on the Orion at different etalon gap spacings. As mentioned earlier a total of 33 interferograms were used in the data analysis. Firstly, the kinematic information in a region was extracted from the observed interferograms as described in section 3.2. Velocity profiles were obtained for about 2000 positions on the nebula. The velocity field was studied in three aspects: (i) General velocity flow due to expansion of the HII region; (ii) High velocity flows associated with different physical processes taking place in the nebula and (iii) Random or turbulent flow. In what follows, we describe our results on these three aspects and discuss their implications.

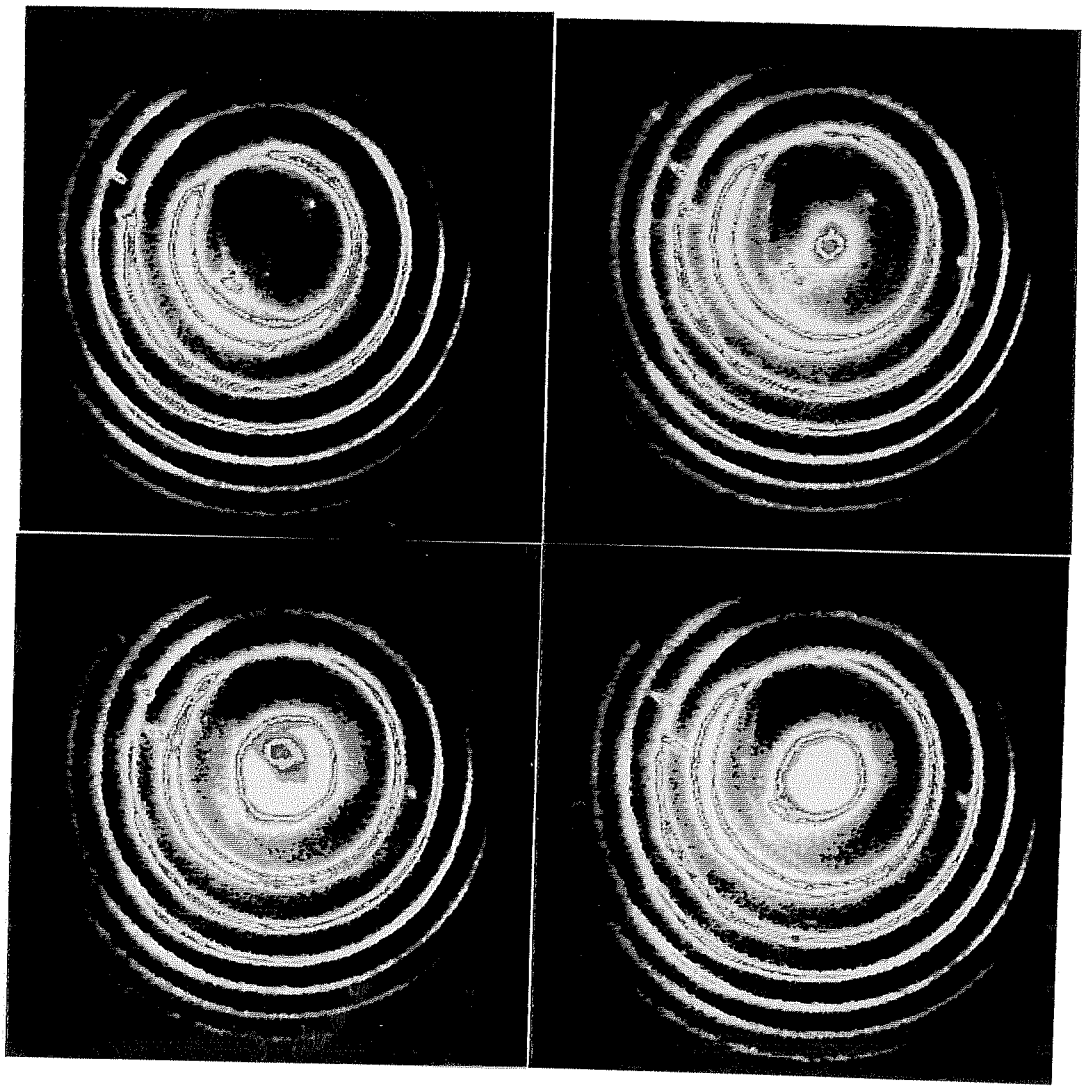

Figure 4.2: A mosaic of four interferograms of the Orion nebula in [OIII] 5007 Å line taken at different increasing étalon spacings. The expansion of the fringe pattern as the étalon is scanned can be noted.

4.4 General velocity flow

4.4.1 Two components

By visual inspection , in general, the profiles are found to be either asymmetric or broad winged. Therefore, in general two gaussians were necessary to fit the profiles: a narrow one and a broad one. In most cases, the FWHM of the narrow component was found to be about 20 ± 3 km/s and that of broad component was about 50 ± 3 km/s. It is seen that the broad component is either blue-shifted or red-shifted with respect to the narrow profile as shown in Figs. 4.3 and 4.4 respectively.

In some positions it matches with the peak of the narrow component as shown in Fig. 4.5. It is also observed that the amplitude of the broad profile varies with respect to the narrow profile, as shown, for instance, in Fig. 4.6 which shows a stronger broad component.

Since profiles can be obtained using the Imaging Fabry-Pérot Spectrometer either by taking radial scans at any spatial point on a given fringe or by scanning the FP etalons over one FSR and obtaining profiles at any given pixel, we have identified more than 100 pixels where the scanning had provided complete profiles. The velocity profiles at these positions were generated and fitted with appropriate gaussians. It was found that here also two gaussian components could be fitted for most of these profiles, an example of which is given in Fig. 4.7. The FWHM of the two components are found to

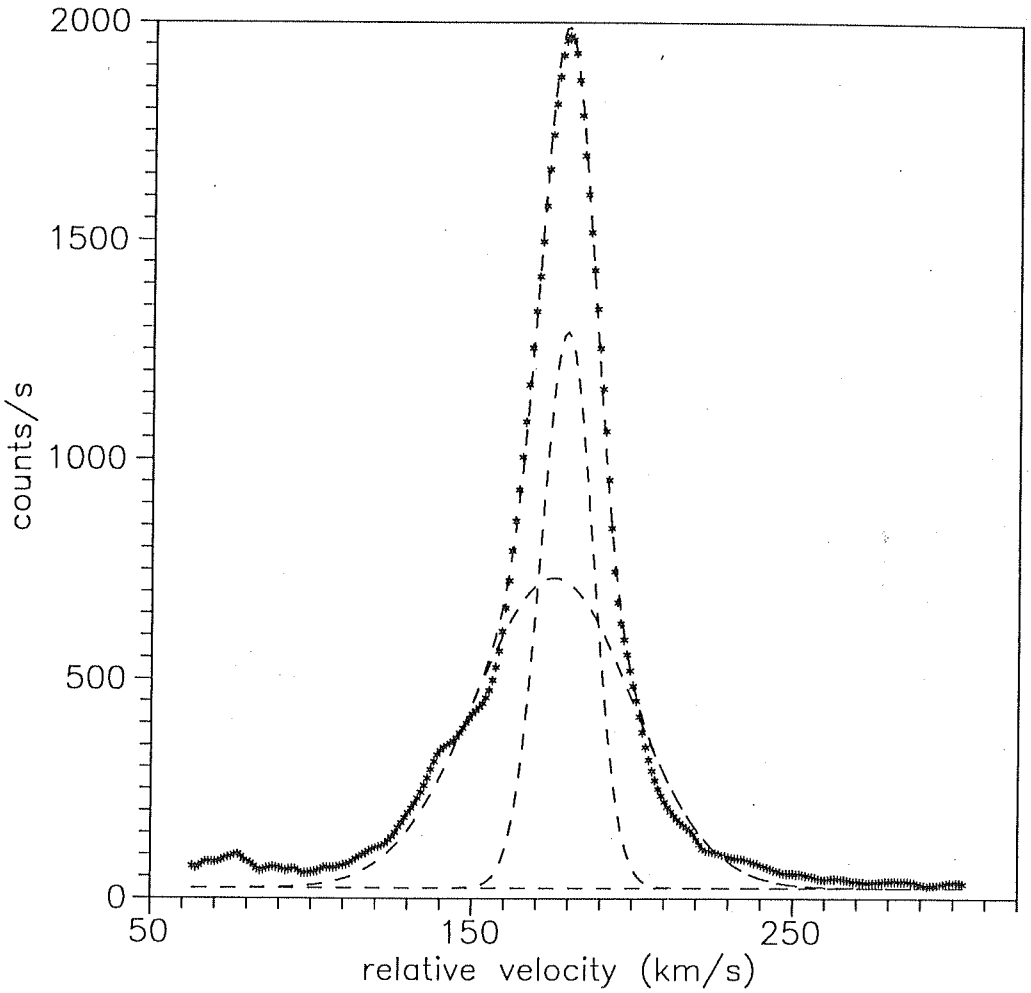

Figure 4.3: Line profile showing asymmetry (data points are denoted by asterisks). The dashed curve going through the asterisks is the composite gaussian fit with the individual gaussians shown by the small dashed curves. The dashed line at the bottom is the continuum level. The broad-component is blue-shifted with respect to the narrow one.

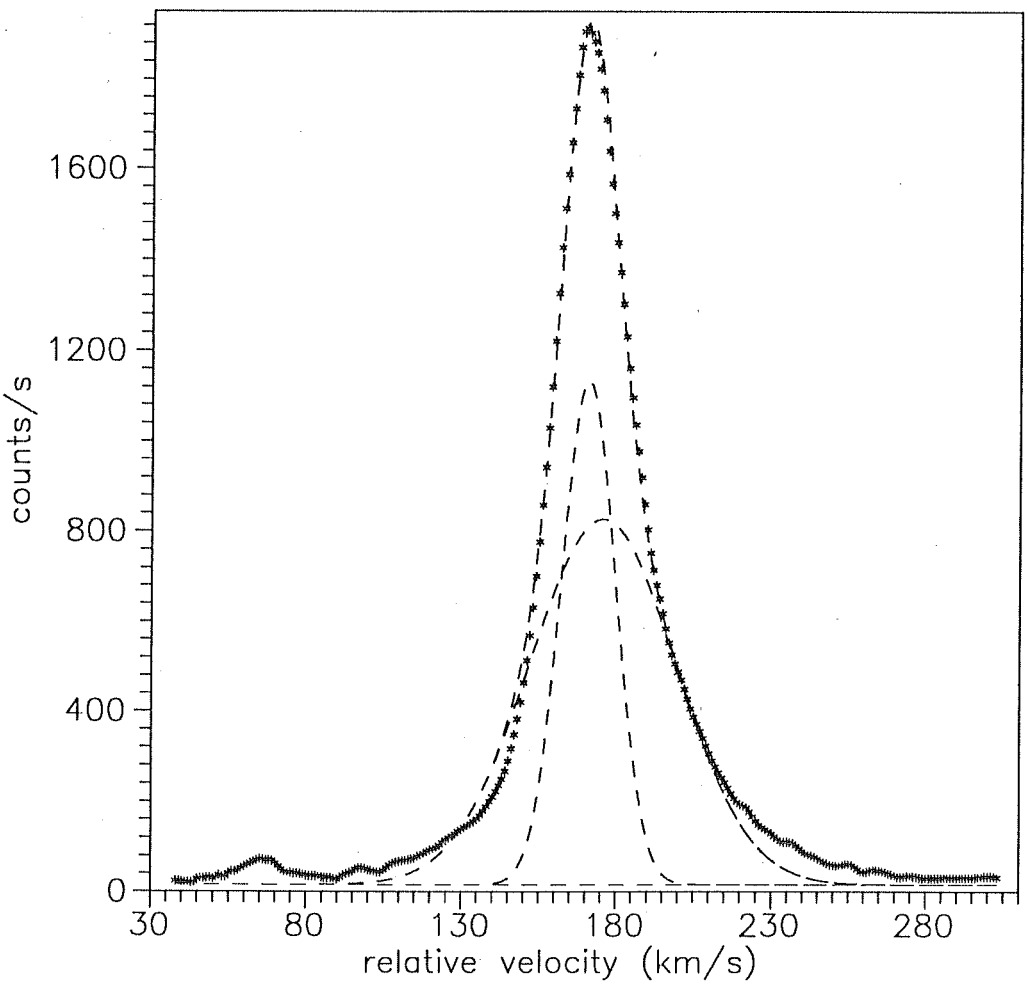

Figure 4.4: Line profile showing asymmetry (data points are denoted by asterisks). The dashed curve going through the asterisks is the composite gaussian fit with the individual gaussians shown by the small dashed curves. The dashed line at the bottom is the continuum level. The broad-component is red- shifted with respect to the narrow one.

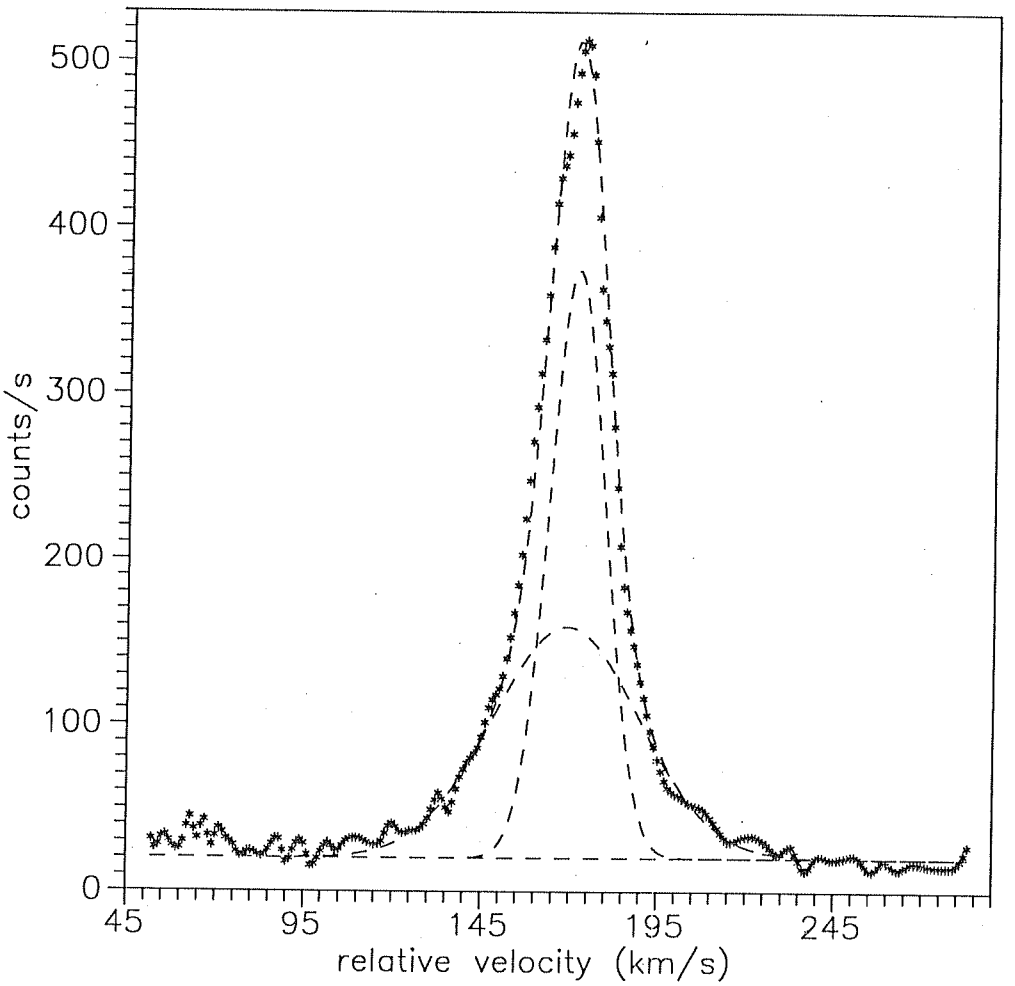

Figure 4.5: Line profile showing broad wings(data points are denoted by asterisks). The dashed curve going through the asterisks is the composite gaussian fit with the individual gaussians shown by the small dashed curves. The dashed line at the bottom is the continuum level. The broad-component and the narrow one have no relative velocity.

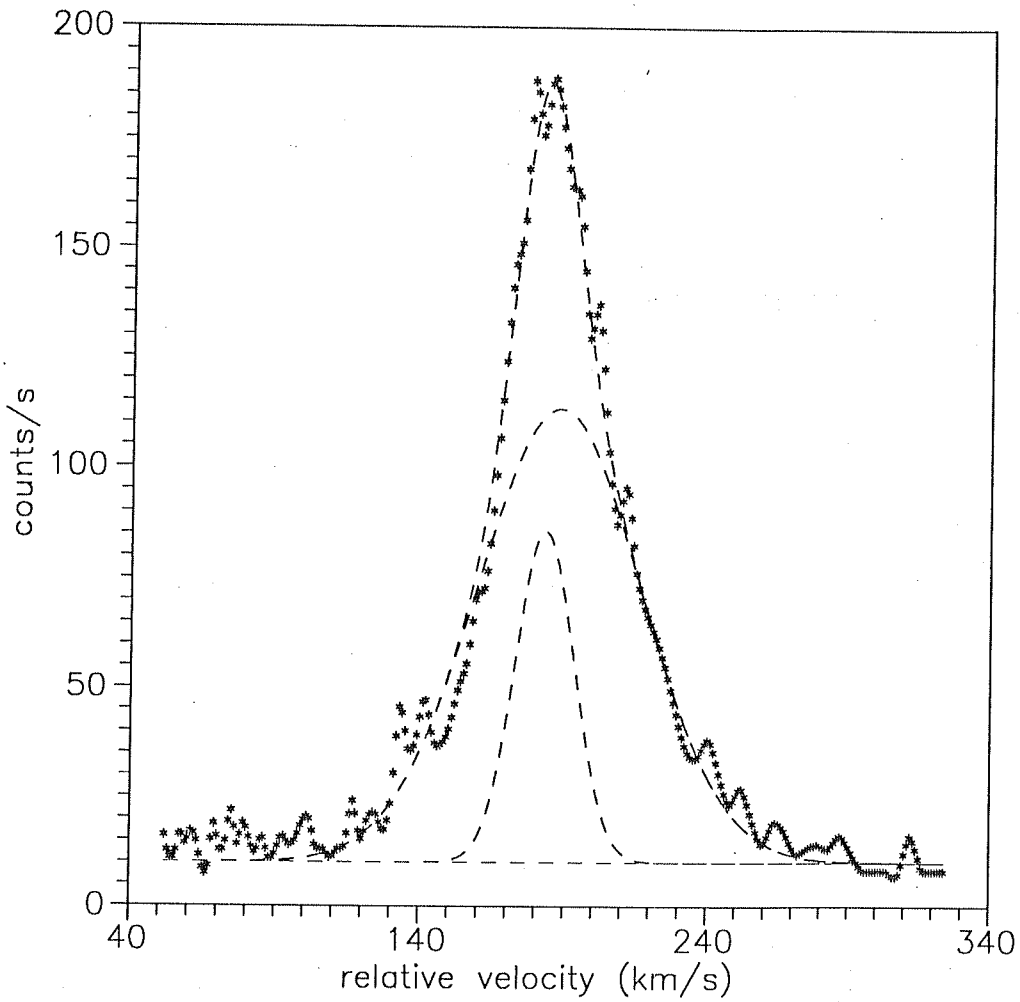

Figure 4.6: Line profile showing broad wings(data points are denoted by asterisks). The dashed curve going through the asterisks is the composite gaussian fit with the individual gaussians shown by the small dashed curves. The dashed line at the bottom is the continuum level. The broad component is stronger then the narrow one.

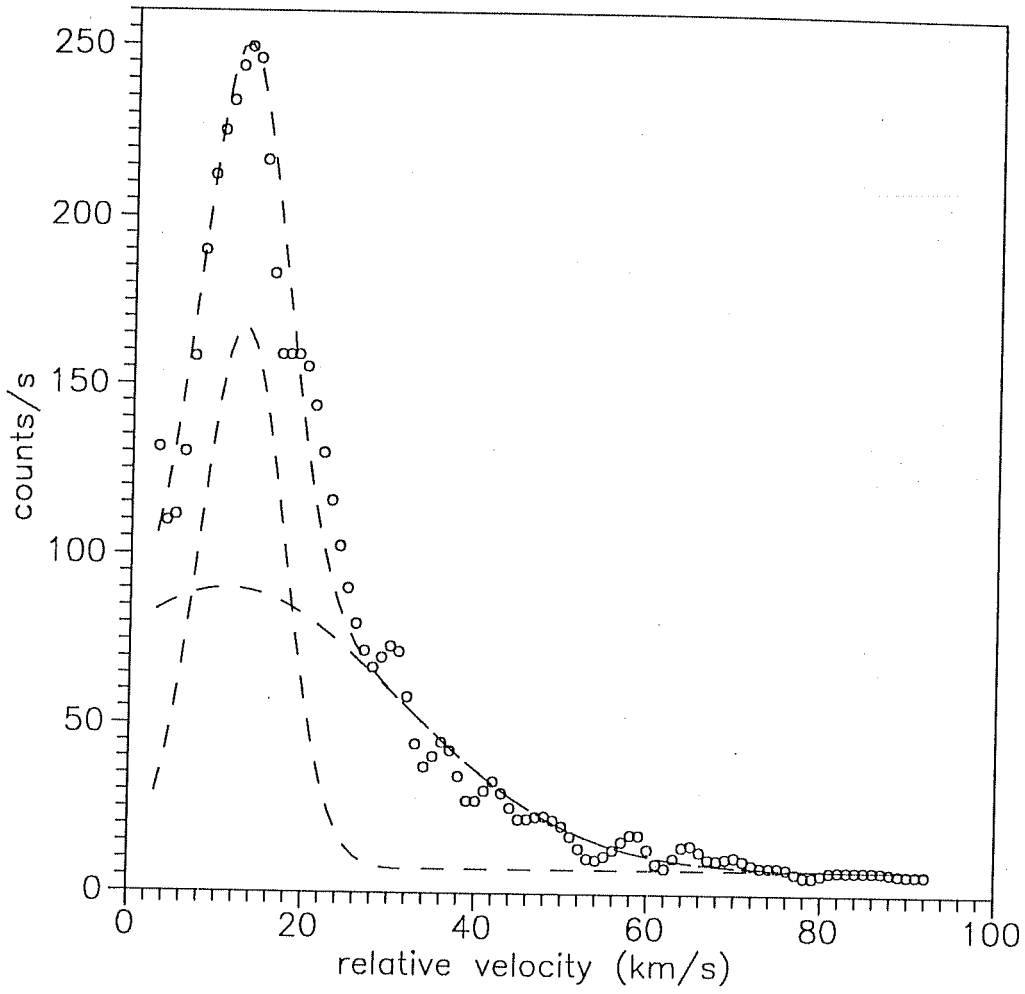

Figure 4.7: Line profile at a single pixel (data points are shown by circles) fitted with two gaussians.

be about (i)15 ± 3 km/s and (ii)50 ±3 km/s at a position (1.8′N, 52″W of Trapezium), showing a very good correspondence with the results obtained from the radial scans.

It should then be seen if these two components actually represent two different flow patterns or these are created artificially. The latter possibility may arise (i)due to the uncertainity in the gaussian fitting procedure (ii)because the gaussian fitting is actually forced and (iii)because of the fact that we did not deconvolve the observed profiles for the instrumental broadening. As mentioned earlier, the uncertainity in the gaussian fitting procedure is about 10% for a good S/N ratio and as such cannot account for the second amplitude by itself; also, the fit was very bad with just one gaussian, implying therefore that there have to be two components to explain the observations. As far as the forcing of the gaussian fit is concerned, the reason lies in the physical aspects of the line profile in the diffuse nebula: the thermal broadening and the turbulence are gaussians and the velocity gradient does not change the profile shape selectively in the wings. The broadening of the wings due to pressure effects is not relevant in the nebular conditions. To check the instrumental broadening the profile at a single pixel was deconvoled and then fitted with gaussians (Fig. 4.8). The fit seems to be quite good implying that it is not the effect of the instrument. Finally, this leaves us with the possibly inevitable result that there, in fact, might be multiple components.

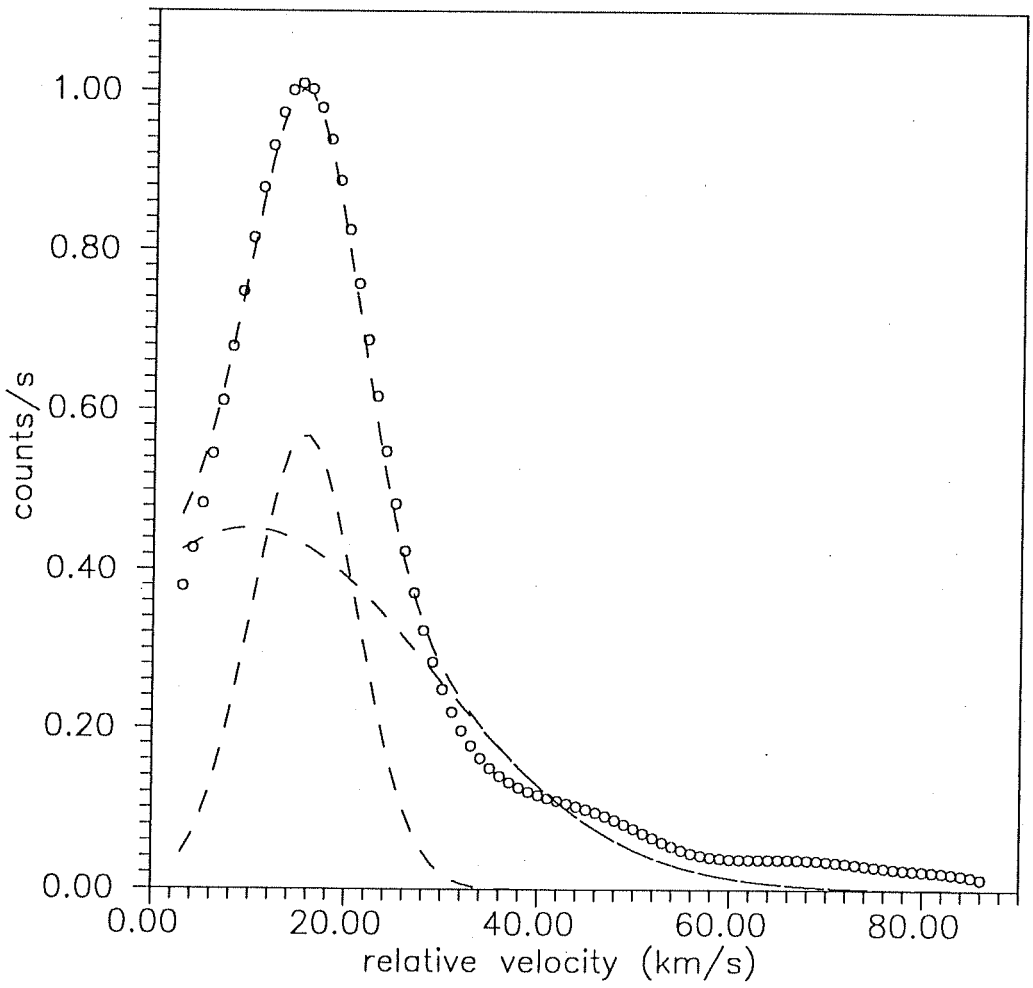

Figure 4.8: Deconvolved profile of the line profile at a single pixel(shown in Fig. 4.7) fitted with two gaussians.

4.4.2 Discussion

In the Orion nebula, according to the broadly accepted model (Balick et al, 1980), θ^1 C Ori ionizes the gas resulting in the formation of a 'core' of ionized gas. The dense neutral cloud situated behind θ^1 C Ori is also ionized by the ultraviolet photons falling on it but the flow of the ionized gas is obstructed in this direction (i.e., the direction of the neutral cloud) due to the dense material and therefore it flows towards the core region thereby mixing with the gas and is dispersed outwards (towards the observer). This will give rise to different 'flows' and the two components could be the result of such flows. It is possible that stellar winds from OB stars can play a significant role in the dynamics. The observational evidence for this was first reviewed by Pottasch (1969). The fast stellar winds from the Trapezium stars could possibly be interacting with the flow of ionized gas coming from the molecular cloud situated behind the Trapezium and the two components could be the result of these interactions along the line of sight. Or it could be the effect of the interaction of neutral condensations with the ionized gas as suggested by Balick et al (1974). The former explanation seems to be plausible since there is evidence for strong stellar wind from θ^1C Ori with terminal velocity of 1650 km/s (Snow and Morton, 1976), and about 500 km/s from θ^1D Ori (IUE observations).

Figs. 4.9 & 4.10 show the iso-velocity contour maps for the two components. Different features of the nebula are also marked on these figures. The

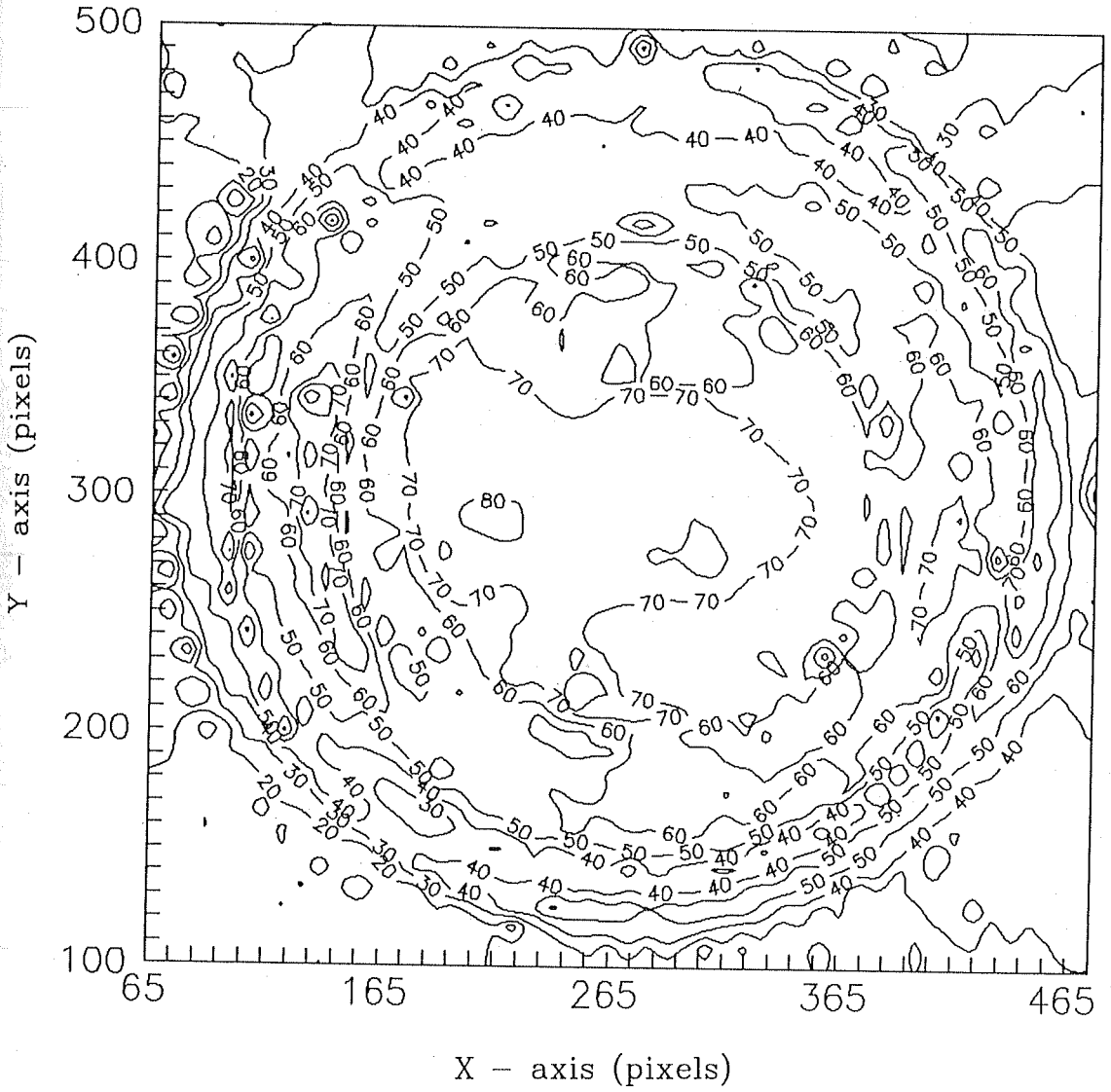

Figure 4.9: Iso-velocity contour map for the narrow component. One pixel corresponds to $\sim 1.23''$ on the sky.

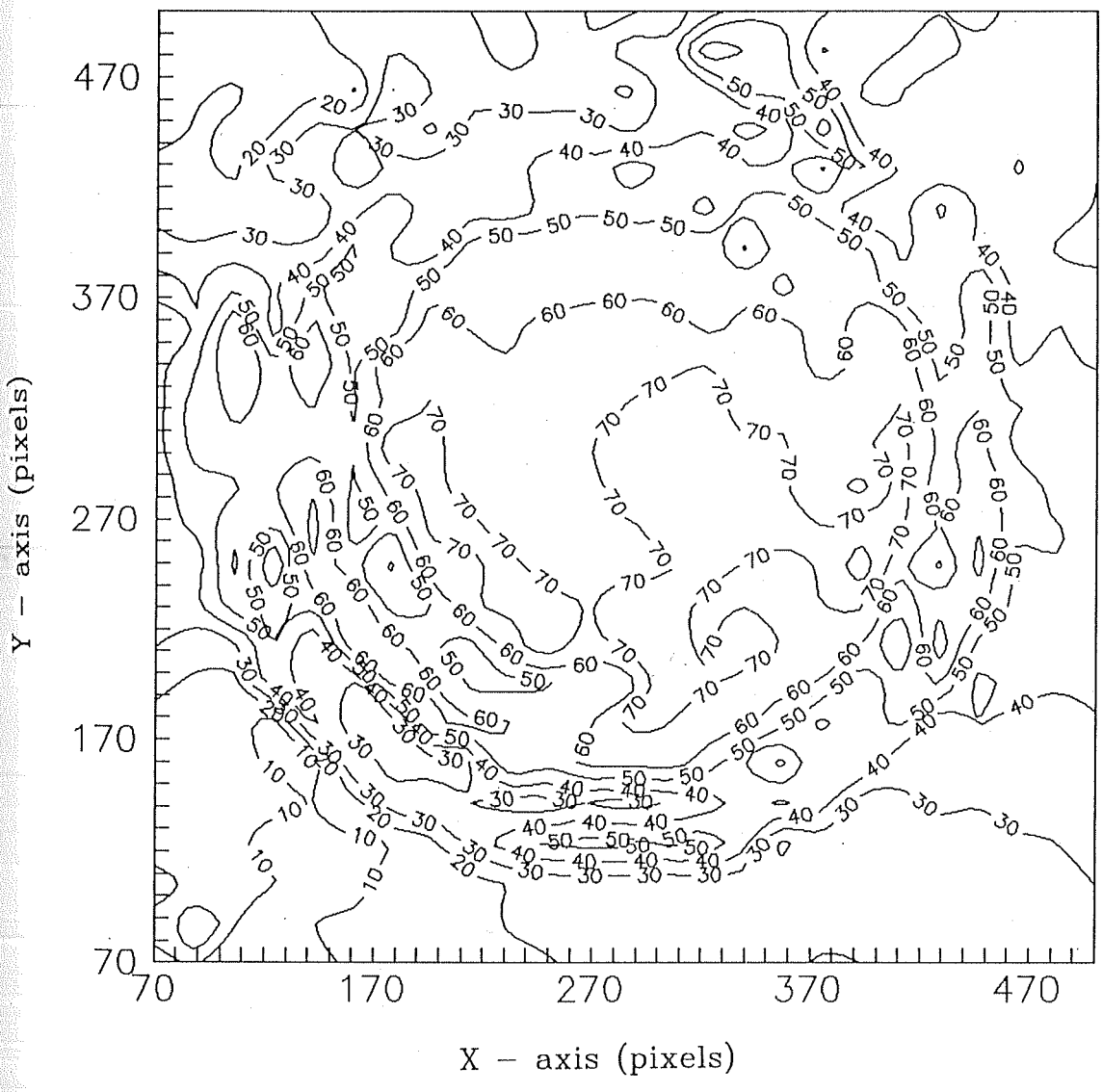

Figure 4.10: Iso-velocity contour map for the broad component. One pixel corresponds to $\sim 1.23''$ on the sky.

iso-velocity contour maps indicate that the general flow is same in both the components except that the velocity field of the narrow component shows certain high velocity flows superimposed on the main flow of the gas. Such flows seem to be absent in the broad component.

Previous studies in Orion gave an indication of line profile asymmetry (Wilson et al, 1959; Smith and Weedman, 1970) and presence of multicomponents in [OIII] 5007 Å line profile (Meaburn, 1984). These studies were followed by Castañeda's (1988) work. His observations were made at higher spectral resolution ($\sim$ 1 km/sec) using a slit spectrograph. He could decompose the profiles into three components having a mean FWHM of (i) 10.02$\pm$ 0.1 km/s, (ii)9.48$\pm$ 0.12 km/s and (iii) 31.26$\pm$ 0.21 km/s. Probably, the narrow component in our study ($FWHM$ $\sim$20 km/s) is the sum of the first two components observed in Castañeda's work which could not be resolved in our observations due perhaps to the lack of adequate spectral resolution. It can be shown, with the assumption that all the components are gaussians and an instrumental FWHM of 6 km/s, that

$$\begin{aligned}(FWHM)_{total} &= [(FWHM)^2_{compl} + (FWHM)^2_{comp2} + (FWHM)^2_{Ins}]^{1/2} \\ &= (10^2 + 9.5^2 + 6^2)^{1/2} \\ &= 16km/s \end{aligned} \tag{4.1}$$

which is in good agreement with the narrow component in our work.

4.4.3 Champagne flow

An examination of the contour map of the component one as shown in Fig. 4.9 indicates that the general velocity flow is blue shifted with respect to the Trapezium stars with a decrease in relative radial velocities outwards (114 km/sec/pc). Therefore, the flow seems to be directed towards the observer in accordance with the champagne model (discussed in section 1.12.3), which simply shows that the ionized material from the hot stars in the nebula situated at an edge of the parent molecular cloud is rushing into the interstellar medium due to the pressure gradient established at the HI-HII interface. This 'flow' which is directed towards the observer is termed as the *main flow* (Balick, 1980) or *champagne flow.* This result is in general agreement with those of the earlier authors (e.g., Castañeda, 1988).

4.4.4 Model Profile

In this section, we describe the model emission line profile constructed for Orion near θ^1 Ori complex and compare it with the observed profile at that position. This is to provide a check on the assumptions made regarding the physical conditions in the nebula as well as to see if champagne flow could produce the observed profiles. As far as we know, this is the first attempt to model the observed velocities assuming a champagne flow in the Orion nebula.

Method

The observed line profile results from the integration along the line of sight of radiation emitted by gas moving with different expansion velocities. The line of sight velocity is the sum total of the effects of (i)thermal broadening represented by the Maxwellian distribution of ion velocities (ii) velocity gradient with respect to the radial distance and (iii)turbulent motions. But it is difficult to delineate these effects. It is, however, possible to generate synthetic profiles by putting in reasonable values representing these effects and compare with the observed profiles. The final synthetic profile is obtained under the following assumptions: (i) Champagne flow is assumed where the flow is directed towards the observer, (ii)the distribution of turbulent flow is assumed to be gaussian in nature, and (iii)a constant temperature is assumed throughout the nebula. Therefore, the intensity of emission for a particular line of sight is given (Osterbrock, 1974) as,

$$I(v) = I_o \int_{-\infty}^{\infty} n_e^2 \, e^{-\left[\frac{[v-v(r)]^2}{(2kT/m)+v_T^2}\right]} dv \qquad (4.2)$$

where I_o is a constant, k is the Boltzmann constant, m is the mass of the ion, v_T the most probable turbulent velocity and n_e is the electron density assumed constant within the HII region. Actually, eqn. 4.2 becomes a triple integral in r, θ and ϕ, where, r represents the radial distance from the central star to any point in the nebula and θ is the angle that the direct line of sight from the central star to the observer makes with the radius vector r and ϕ is the aperture or field of view from the observer. A schematic of the assumed

geometry for the HII region is given in Fig. 4.11.

The final synthetic profile is obtained by evaluating the triple integral and convolving with the instrument profile $G(v)$ as follows,

$$I(v) = \int_{-\infty}^{\infty} G(v' - v) I(v') dv' \tag{4.3}$$

A line profile is generated using this method for [OIII] line 5007 Å at a position corresponding to about 2 arc minutes from θ^1 C Ori with position angle of 346° and a view angle of 4 arc sec corresponding to our spatial resolution. The velocity gradient due to the champagne flow was taken to be 1.73 km/s/pc (from theoretical work, Yorke et al, 1983) and a temperature of 10^{4° K was assumed. The most probable turbulent velocity was assumed to be 9 km/s. This is in agreement with Castañeda's (1988) value for his first component. The model considers the champagne flow and therefore the profile is obtained by integrating the line of sight velocities coming towards the observer with very little contribution of velocities from the back of the Trapezium. The theoretical profile so obtained is compared with the observed one as shown in Fig. 4.12.

Discussion

The profile seems to match reasonably well with the narrow component of our observed profile. It also matches with the first component of Castañeda's (1988). The second component of Castañeda's can still be accomodated

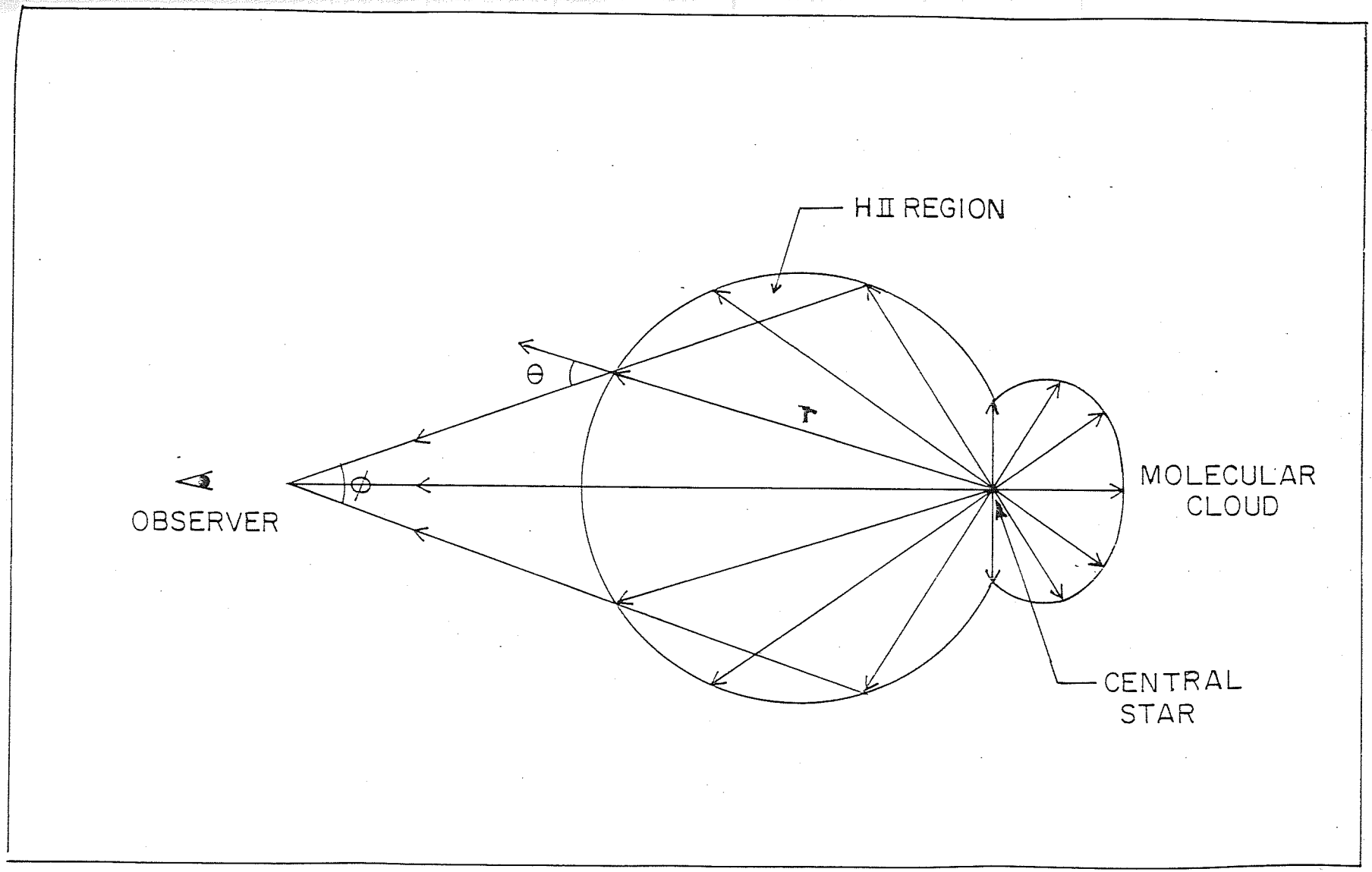

Figure 4.11: Schematic of the assumed geometry for the model profile.

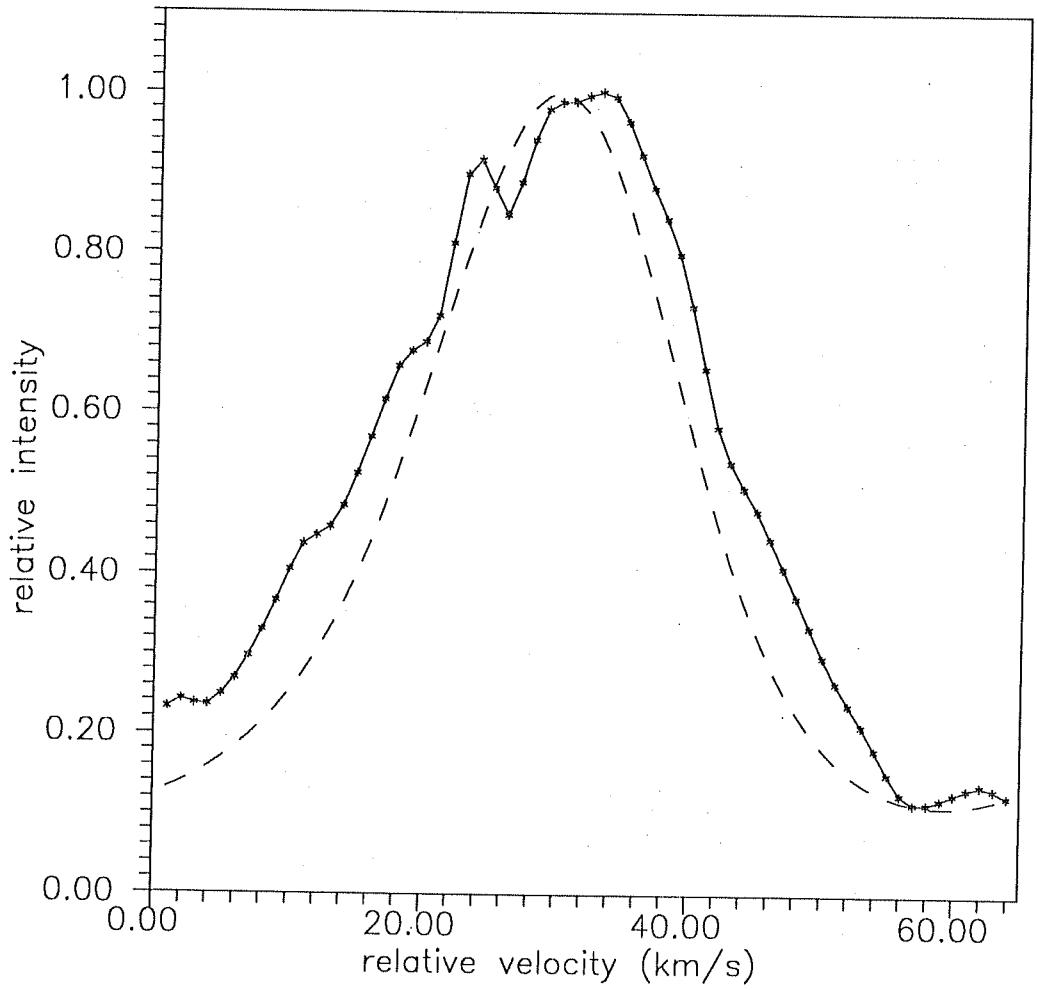

Figure 4.12: Model profile compared with observed profile in [OIII] 5007 Å line in Orion nebula at about $2'$ from θ^1 Ori at a position angle of 346°.

within the accuracy of our results.

As far as the second and broader component is concerned, attributing it to the thermal width alone leads to unduly large temperature and it is difficult to defend it. Alternatively it can be explained by either a large velocity gradient or large scale turbulent flows or both; but, that seems to be improbable. Thus the broader component can be attributed to the interaction of stellar wind with the general flow of the gas. In any case, the champagne flow representing the HII region associated with θ^1 Ori seems unrelated to the broader component.

4.4.5 Axisymmetry

From the Fig. 4.9 it is quite apparent that there is a degree of axi-symmetry in the iso-velocity contours centred about 71″ NE of θ^1C Ori. Some type of symmetry is also reported by Hanel (1986) in the iso-velocity map of [OIII] line, which he finds is not observed in the contour maps of other lines ([NII], $H\alpha$, [SII]). Castañeda's study showed elliptical iso-velocity contours centred about the maxima 7″ NE of θ^1 C Ori. This maxima around θ^1 C Ori could not be located in our map due to lack of data in this region. This symmetry, in general, can be expected in an HII region powered by a single star. From this also it is probably clear that the main ionizing star for the central HII region in Orion is $\theta^1 C$ Ori.

4.4.6 Velocity flow around θ^2 Ori

The HII region around θ^2 Ori is supposed to be physically separate and unconnected from the main HII region around Trapezium (Peimbert, 1982). Some of the studies which favour this argument are: (i) the spectroscopic studies in [NII] line of Orion show that the radial velocities were found to be different around θ^2 Ori when compared to θ^1 Ori (Deharveng, 1973); (ii) the optical linear polarization map due to Pallister et al (1977) shows a centrosymmetric pattern due to the scattering of stellar light by the nebular matter, around the Trapezium (θ^1 Ori) as well as θ^2 Ori. It is observed further that the pattern in the region around θ^2 Ori, is unconnected to that around θ^1 Ori (Pallister etal, 1977); (iii) in the chemical abundance study it is found that the ratio of He^o/He^+ is large in the direction of θ^2 Ori when compared to θ^1 Ori. This implies that there is a lower degree of ionization in the direction of θ^2 A Ori compared to that in the direction of θ^1C Ori indicating that the radiation fields of θ^1C Ori and θ^2 Ori are uncoupled . Also, lack of dust and CO emission to the south-east of the bar and lower extinction in the direction of θ^2A Ori than towards θ^1C Ori suggest that θ^2A Ori is a foreground object relative to the Trapezium stars (Peimbert, 1977). Therefore it was necessary to study the velocity field around θ^2Ori separately.

That the velocity fields around θ^1 and θ^2 Ori are unconnected can be seen from our observations presented as the contour maps in Fig. 4.9, and

Fig. 4.10. Our velocity map showed that there are certain high velocity regions around the stars θ^2 A Ori and θ^2 B Ori (discussed in the following section) but there is no particular well defined velocity pattern around these stars. The interaction of the flow from the HII region associated with θ^1 Ori with that from the HII region associated with θ^2 Ori might have caused a complete disruption of the pattern : the redward components of the θ^2 Ori HII region getting partially or fully cancelled by the blueward components of the flow from θ^1 Ori. This can happen as the two opposing flows cannot seep through each other because the ion mean free path is much smaller than the size of the HII region.

HII region around θ^2 B Ori

A region of particular interest is found in the [OIII]/$H\beta$ map due to Pogge et al (1992), south-east of the bar ionization front centred roughly on the star θ^2 B Ori, where there is a sudden drop in the mean value of [OIII]/Hβ ratio to 1.3 and then a distinct increase to 2.3 about 10″ south-west of θ^2A Ori. It was interpreted to be a region which is being shadowed from the θ^1 C Ori due to the dense absorbing material around the bar. The intensity ratio maps of Pogge et al (1992) show further that the ratios [NII]/$H\alpha$ and [SII]/$H\alpha$ are higher in the region centred on θ^2 Ori. The optical depth map of these authors shows that the extinction is not particularly lower compared to the surrounding regions. This probably suggests that the region has emission particularly from low excitation ions indicative of a weaker

radiation field around θ^2 B Ori, a B0.5 type star (Table 4.1) than that around the Trapezium. Further and more importantly our velocity map shows a velocity field structure different and delinked from that surrounding $\theta^1 C$ Ori. This is also supported by the polarization map (Pallister et al, 1977), where it is found that the centro-symmetric pattern around θ^2 B Ori is unconnected with that of θ^1 C Ori. In view of this we propose an alternative explanation that the region centred on $\theta^2 B$ Ori is actually its associated HII region.

4.4.7 The Orion dark bay

The dark bay feature is located east of the Trapezium stars and at the north edge of the bar ionization front. It is found to be a region of low surface brightness and hence is associated with low emission. It has been verified that the dark bay feature is not a manifestation of the effect of heavy extinction with the help of the radio continuum map at 21 cm (Van der Werf & Goss, 1989), the CO map (Thronson et al, 1986), [CII] 157.7 μm map (Stacey et al, 1992) and the optical extinction map (Pogge et al, 1992). Our results on this region show relatively low velocities ($\sim$ 20-30 km/s) compared to the θ^1 Ori HII region. The low velocities actually suggest an obstructing material to the expanding gas in the HII region.

Table 4.2: High velocity positions with reference to θ^1 Ori

Sl. No.	Position from Trapezium stars (arc minutes)		Relative velocity (km/s)
1.	2.30 S	2.29 E	65
2.	2.20 S	2.60 E	67
3.	2.05 S	1.60 E	53
4.	2.05 S	2.85 E	57
5.	1.20 N	0.05 W	51
6.	3.60 N	0.78 W	50
7.	3.96 N	0.25 W	59
8.	4.60 N	1.80 W	53
9.	4.70 N	0.80 W	69

4.5 High Velocity Flows

Certain localized regions of high velocities (~50 km/s) are found on the iso-velocity map (Fig. 4.9). Some of these regions correspond to identified stellar sources and some others do not. The positions given in Table. 4.2 have a positional accuracy of $\sim$ 4 arc sec. These regions are of the size of a few arc seconds. The table also lists the relative radial velocities. It can be seen that the radial velocities are red-shifted with respect to the general flow, in all the cases. In what follows, we discuss these in detail.

4.5.1 Around identified stellar sources

(i) $\theta^1 C$ Ori and (ii) $\theta^2 B$ Ori. The reason for high velocity around θ^1 C Ori is that the champagne flow is directed towards the observer and hence the flow velocity is maximum around the star and decreases away from it. Further acceleration is possible through other mechanisms, especially by radiation pressure.

Radiation Pressure

When the radiation from a hot star is absorbed by the surrounding dust, it gets heated up and the energy is radiated isotropically in the infrared. The photons carry momentum with them along with the energy. Therefore, when the radiation is absorbed by the dust, the momentum also gets transferred to the dust since the photoabsorption crossection for the dust is larger than that for ions. This results in a force on the dust, which is much greater than the inward force due to gravity, and the dust is rapidly accelerated outwards. The radiation force on the dust particle is given as follows (Osterbrock, 1974):

$$F_{rad} = \pi a^2 \int_0^\infty \frac{L_\nu}{4\pi r^2 c} P_\nu \, d\nu \sim \frac{a^2 L}{4 r^2 c}$$

where P_ν is the efficiency of the particle for radiation pressure, a is the size of the dust particle, L_ν is the luminosity of the star per unit frequncy interval, L, the total luminosity, and r is the distance from the star. The collisions between the dust and the gas will then accelerate the gas outwards

resulting in high velocity flow. Furthermore, there are observations in the optical and infra-red regions showing that there is an anomalous extinction in Orion nebula ($A_v/E(B-V) \sim 5.0$) compared to other diffuse clouds ($A_v/E(B-V) \sim 3.0$)(Johnson, 1968). This anomalous behavior is accounted for by the presence of large dust grains ($\sim 0.1\mu m$) around $\theta^1 C$ Ori (Sorell, 1992). Also, the optical depth $\tau(H\alpha)$ map due to dust derived from the $H\alpha/H\beta$ Balmer decrement by Pogge et al (1992) shows that the reddening of stars in the foreground of Orion is small (E(B-V) = 0.05 mag, Breger et al, 1981), while the reddening toward $\theta^1 C$ Ori is E(B-V) =0.32 mag (Bohlin & Savage, 1981), thus, it was pointed out that most of the additional extinction should arise in the nebula proper. This indicates the presence of large amount of dust around θ^1 C Ori. Therefore, the high velocity flows near the hot stars found in our observations could be partly caused by radiation pressure-driven stellar winds.

4.5.2 Around protostellar sources

Shock excitation

An indication of high velocity flow with a velocity jump of $\sim$ 50 km/s (refer Table 4.2, position 5) around 1.2 arc min NW of Trapezium stars is found to be corresponding to a peak of shocked H_2 emission observed in $2.12\mu m$(Beckwith, 1978, Peak I). Shock excitation of the H_2 was first sug-

gested by Gautier et al (1976) and Kwan and Scoville (1976) to explain the H_2 emission. Several model calculations were made in order to check this possibility (Hollenbach and Shull, 1977; London et al, 1977; Kwan, 1977). The model calculations gave limits to the shock velocities and volume densities. With these values of density and velocity, the minimum pressure required to drive a shock was given as $\sim 3 \times 10^{-7}$ dynes cm^{-2}. Since there was no observed luminosity source which could drive such a shock continuously by applying the required pressure on the molecular cloud, the shock excitation of H_2 was attributed as due to an energetic explosion such as that from a supernova (Beckwith etal, 1976). A feature corresponding to this peak (position 5 in Table 4.2) was also observed in the HST image as a prominent dark cloud followed by a 20″ jet-like feature apparently emanating from a star located at the edge of this cloud (Hester et al, 1991). A corresponding feature was also reported in the [SII] line at this position (Raju et al, 1993).

A jet like feature

There is an interesting feature in the form of a knot like structure observed in the image about 1.5 arc min north west of the Trapezium stars(Fig 4.2). It is found to have a radial velocity of about -11 km/s with respect to the surrounding region and the line profile shows a FWHM of about 90 km/s (Fig 4.13) and there is a split in the line profile showing an expansion velocity of 12 km/s. There is no report of such a feature in the earlier studies in that position. This could possibly be the effect of stellar winds from Trapezium

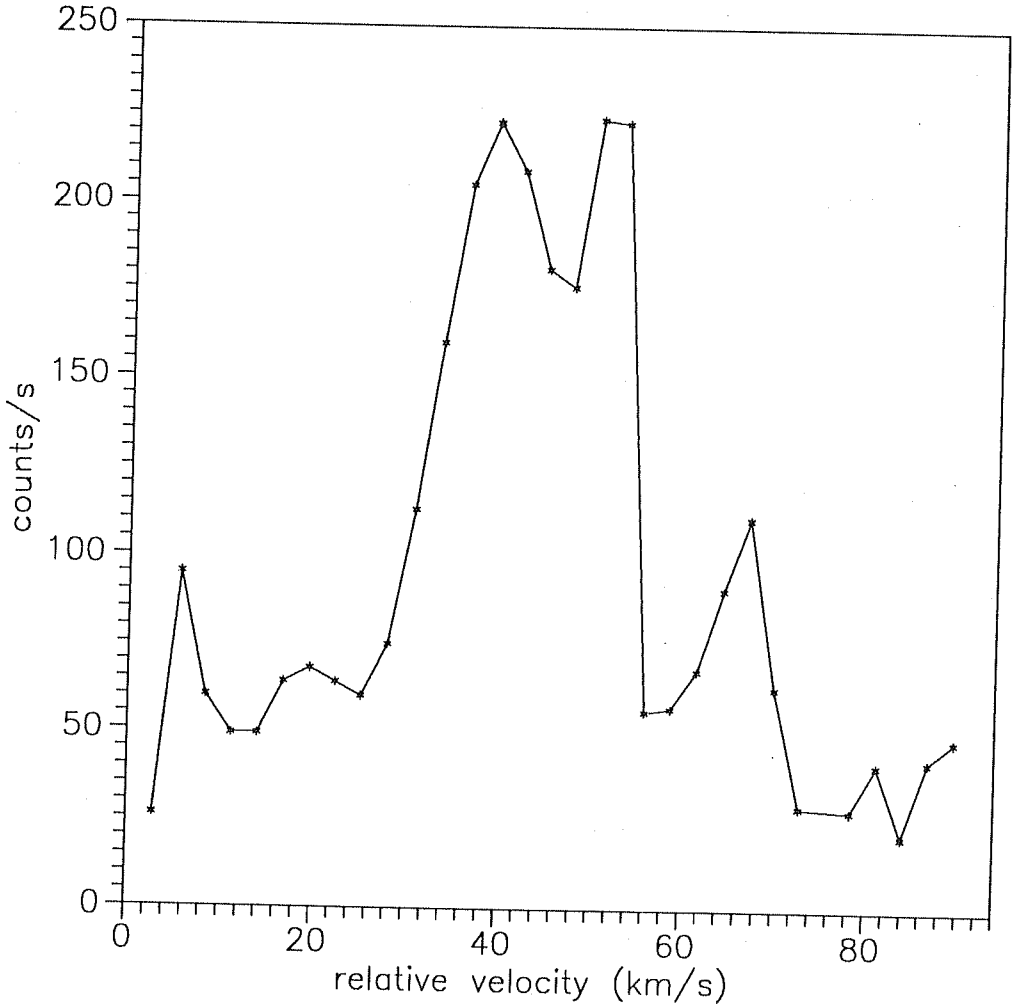

Figure 4.13: A line profile at the jet like feature about 2.3 arc min NW of Trapezium.

ablating a neutral blob. The blob eventually becomes partially ionized due to stellar photon flux or shock compression. These are called partially ionized globules (PIG). PIGs are small dense neutral globules completely covered with ionization fronts with the ionized gas expanding into the low density medium (Dyson, 1968a,b, Kahn 1964). Evidence for the existence of PIGs was found by Dopita et al (1974). The effect of stellar wind on these globules was first modelled by Dyson (1975). The large FWHM found by us also possibly suggests the stellar wind interaction.

Due to the sky projection effect, the exact position of the globule from the central star is difficult to be known, therefore, two possibilities could be considered in order to explain the feature (i) The globule is considered to be situated near the hot star (L=10^{38}ergs/sec). In this case, the velocity observed (-11 km/s) is not the actual velocity but could be the projected velocity along the line of sight (i.e., $v_{actual} = v_{proj}$ /cosθ, θ being the projection angle). In this case, however, ionization effects due to shock (stellar wind) should be seen. We do not find enhanced [OIII]/Hβ (from Pogge et al, 1992) in this region implying less possibility for the globule to exist in the proximity of θ^1 C Ori. (ii)The globule is situated rather far away from the star with the observed velocity being the actual one without much of projection effect. This situation can be explained by considering Dyson's model (1975). He considered the case where the globule is supposed to be situated at a distance of 1 pc from the star and the rate of mass loss from the star is assumed to be $10^{-6} M_{\odot}$/yr. Then the velocities of the shocked structures are

found to be about 10 km/s implying that there is no significant kinematic or ionizing effect of stellar winds on the globule in such a case. The blue-shift in the Doppler velocity indicates that the globule is situated in front of the Trapezium stars.

4.5.3 The molecular cloud region

According to the Blister model (Zuckerman, 1973) , the HII region in Orion is in front of and eating into the molecular cloud behind. The molecular line studies of ^{13}CO (Bally et al, 1991) have shown that the structure of molecular cloud is highly filamentary. The $BN - KL$ (Becklin-Neugebauer-Kleinmann-Low) infrared nebula is found to be the young star forming region located in front of the OMC-1 about $0.1 - 0.2$ pc behind θ^1C Ori. The ultraviolet photons from the Trapezium stars penetrate the molecular cloud and photodissociate the molecules (mainly molecular hydrogen and CO) and photoionize the atoms (carbon and silicon).

Studies in the past showed that the photodissociation regions (regions that are situated outside the HII regions where the molecular hydrogen undergoes photodissociation) exhibit CO rotational lines in millimeter, submillimeter, far-infrared regions as well as CII, [OI] and CI optical lines. The existence of photodissociation region was first unveiled in the optical lines of CI and [OI] (Munch and Taylor, 1971; Hippelein & Munch, 1978; Munch and Hippelein, 1982) and in the radio recombination lines of carbon (Palmer et

al, 1967). Certain high velocity flows are found in our observations overlying the molecular cloud (Positions, 6,7,8 and 9 in Table 4.2). These flows are not associated with any peculiar features (Knots or HH objects) detected earlier (except position 5). The possibility is that there could be an infrared source embedded in the cloud, where star formation is being just initiated by a shock such as a supernova explosion. The hot spots found in the radio ^{12}CO map (Loren, 1979) and other ^{13}CO features (Sugitani, 1986 and references therein) do not correspond to any of these features and hence these must be new sources. Alternatively, this can be explained in terms of partially ionized globules (PIGs). The heliocentric radial velocities of the Trapezium stars (29 km/s) and the molecules embedded in the core of PIGs (26 km/s) suggest that the Trapezium and the PIGs are formed from the same neutral cloud into which the ionization front from θ^1 C Ori is eating into. The model presented by Dopita et al (1974) show that PIGs are formed near to the front and are also moving into the molecular cloud, thus explaining the red-shifted velocities found by us.

4.6 The bar ionization front

The bar represents the ionization front region formed at the HI-HII interface. It serves as a laboratory provided for studying the interaction of the ionized material with the neutral cloud. It is supposed to be situated at about 1.5 arc minutes south-east of the $\theta^1 C$ Ori extending from $\alpha = 5^h 32^m 51^s$ and $\delta =$

$-5°27'30"$ to $\alpha = 5^h33^m03^s$ and $\delta = -5°25'36"$ (Elliot and Meaburn, 1974) and going into the background molecular cloud away from the observer. The optical, radio and infrared observations indicate that the bar is seen almost edge-on (Zuckerman, 1973; Balick et al, 1974). The bar ionization front as observed in the recent images obtained from the Hubble space telescope (Fig. 4.14 as reproduced from O'Dell, 1992) indicates that it is originating from the Trapezium stars and not from θ^2 Ori. This is because the front is slightly but clearly concave towards the side of the Trapezium complex and there is diffuse matter in between the Trapezium and the ionization front with a sharp gradient in density towards the convex side (i.e., the side facing θ^2 Ori).

The Orion bar has been studied extensively in the near infrared continuum (Becklin et al, 1976), far infrared continuum (Werner, 1976; Fazio et al, 1974), near infrared line emission (Hayashi et al, 1985), interstellar infrared emission features (Aitken et al, 1979; Geballe et al, 1989; Roche et al, 1989; Bregman et al, 1989), molecular lines (Omodaka et al, 1987) and in $3.3\mu m$ emission (Sellgren et al, 1990). It was first suggested by Fazio (1974*b*) and Balick (1974) that the infrared emission may be associated with the ionization front. Later, observations at 2 and 10 μm (Becklin et al, 1976) confirmed the existence of the bar. The infrared emission was interpreted to be due to the heated dust near the ionization front. It was also shown (Becklin et al, 1976) that the luminosity sources responsible for this emission were the Trapezium stars.

Figure 4.14: The ionization bar front as revealed by the wide field camera images obtained by the HST (from O'Dell et al, 1993).

4.6.1 Velocity field around the bar ionization front

We have mapped the velocity field near the 'bar' ionization front in the [OIII] 5007 Å line (Fig. 4.9). There seem to be certain localised positions around the bar of the size of a few arc secs where there is a rise in velocity of about 30-40 km/s compared to the surrounding regions. But there is no well defined continuous increase in velocity all along the bar in [OIII] velocity map. This can be explained when we compare our velocity map with the emission-line flux ratio maps of [OIII]/Hβ, [NII]/Hα and [SII]/Hα obtained by Pogge et al (1992). It is clearly seen that the [NII]/Hα and [SII]/Hα maps define the razor sharp feature of the bar. However, in the [OIII]/Hβ map, the structure corresponding to the bar is quite diffused and displaced (it is closer to the star than the bar in [NII] or [SII]) and only certain ionized clumps are prominently seen. It appears that the velocity jumps observed by us in some localised regions around the bar are associated with the clumpy features seen in the [OIII] map by Pogge et al (1992). Also the HST images obtained in different lines [NII], [OIII], $H\alpha$ and [SII] (Hester,1991) corroborate with this.

The ionization structure found around the front is obvious since the ratios [NII]/$H\alpha$ and [SII]/$H\alpha$ are sensitive to the rapid change in the state of ionization across the HI-HII interface, whereas [OIII] emission arises in the fully ionized zone and therefore [OIII]/$H\beta$ ratio tracks the ionization structure within this zone, and emphasizes structures different from those found in [SII] maps.

In the electron density map presented by Pogge et al (1992) from the [SII] doublet ratio, the Orion bar ionization front appears as a density enhancement in which the density increases from 2000 cm^{-3} to 3200 cm^{-3} and then drops outward across the front. In the present work, we have obtained a velocity profile, for the first time, across the bar by taking a scan perpendicular to it as shown in Fig. 4.15. There is a rise in velocity of about 20 km/s at the bar position. The velocity from the direction of θ^1 Ori increases from 45 km/s to about 55 km/s across the bar and then falls back to 35 km/s outwards. A comparison of the velocity profile with the density profile (Pogge et al, 1992) shows that when the density is high, the velocity is relatively low and vice versa. This is in accordance with Rankine-Hugoniot jump conditions for flows across isothermal shock fronts, viz.

$$\rho_1 v_1 = \rho_o v_o$$

where ρ_o, ρ_1 and v_o, v_1 are the densities and velocities behind and in front of the shock front respectively. However, it should be noted that the density found from the [SII] line could be different from that found from [OIII] line as these ions occur at different regions. But the electron density derived from [SII] lines does not show much spatial variation. Furthermore, there seems to be a positional difference between the [SII] bar feature and [OIII] bar feature as can be inferred from Pogge et al (1992). However, the velocity profile across the bar obtained by us is quite broad as is the density profile of Pogge et al (1992).

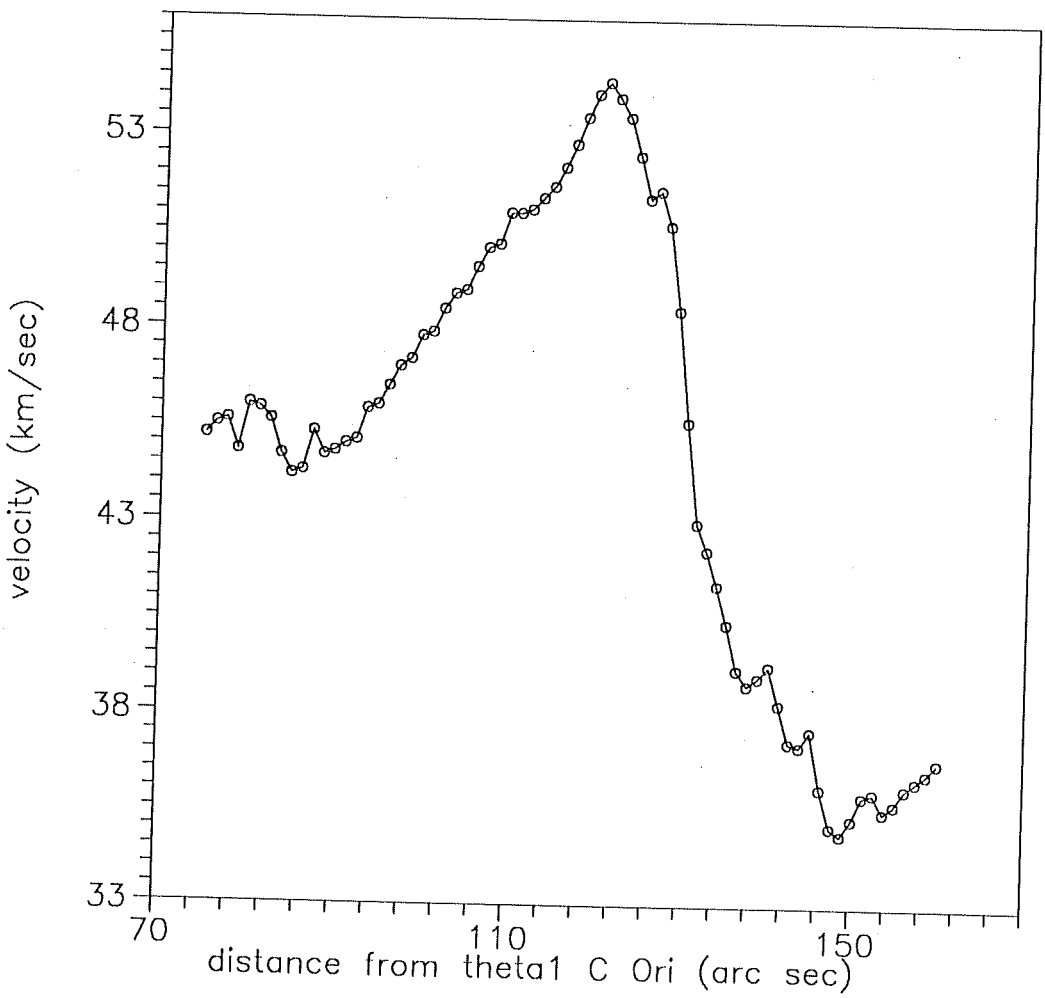

Figure 4.15: Velocity profile across the bar ionization front.

4.6.2 Width of the shock front

As discussed in section 1. 6, a shock wave precedes the expanding ionization front into the neutral cloud because of the supersonically expanding HI-HII interface. Our observations show a velocity jump across the front while the jump in electron density is reported by Pogge et al (1992) in the density profile obtained by them in the optical region and a temperature jump is reported in the CO maps (Loren, 1979). These observations suggest that the shock could most probably be a J type of shock (shock across which discontinuous jump in physical parameters like temperature, density and flow velocity takes place, Hollenbach et al, 1988). Also, there are observations (Johnson, 1983) indicating dissociation of molecules taking place along the shock which again emphasizes on the shock being a J type shock. The width of the shock front in a fully ionized gas is given as follows (Tidmann, 1958)

$$l = (m_H v_s^2/e^2)^2/690 n_e L \tag{4.4}$$

where m_H is the hydrogen mass, e is the electronic charge, v_s is the shock velocity, n_e is the density and L is the coulomb logarithm given as:

$$L = ln[\frac{3}{4(\pi n_e)^{1/2}}(kT/e^2)^{3/2}] \tag{4.5}$$

Taking the temperature in the ionized gas to be 10^4°K and a density of 3200 cm $^{-3}$, L is found to be $\sim$ 24. It is seen from eqn. 4.4 that the width is

Table 4.3: Theoretically calculated parameters of the shock front

angle (degress)	Actual absolute velocity(km/s)	Width of the front in (pc/arcsec)
89	1750	$1.1\times10^{-1}/(48.0)$
88	875	$690\times10^{-3}/(3.0)$
87	583	$1.35\times10^{-3}/(0.6)$
86	438	$4.33\times10^{-4}/(0.19)$
85	350	$1.76\times10^{-4}/(0.079)$

sensitive to shock velocity. We have calculated the actual shock velocity for five different angles (angle that the shock velocity vector makes with the line of sight) assuming that the bar is observed near edge-on (Elliot and Meaburn, 1984). With these values of shock velocities, the width of the shock front is calculated and the results are tabulated in Table. 4.3. The observed projected width is found to be about 35 arc secs from the density profile across the bar from Pogge et al (1992).

4.6.3 Ionization mechanism at the shock front

As discussed in section 1.5, there are basically three mechanisms by which ionization could take place in an HII region: (i) photoionization (ii) collisional ionization due to the compression by a shock wave and (iii) charge-exchange reactions. In order to distinguish between the ionization mechanisms, Baldwin et al (1981) have proposed a classification system based on the strengths

of the emission line ratios (using the available data). However, this method has certain drawbacks as was pointed by Pogge et al (1992) and the shock excited region cannot be isolated from the stellar photoionized region using this method alone, since the regions are all seen overlapping in projection. For example, Pogge et al (1992) have plotted the diagnostic line ratios (like [SII]/Hα vs [OIII]/Hβ) in a shock excited region of the nebula involving HH objects. According to Baldwin et al's (1981) method, it was expected that all these points should lie away from the general locus of HII region-like objects, which was not the case. Pogge et al have interpreted that this could be due to these regions being embedded in a high surface brightness photoionized nebula and therefore could not be decoupled easily with their data and it was concluded that, since HH objects are kinematically distinct with velocities more than 60 km/s (Canto et al, 1980), it should be possible to make the distinction between shock ionized and photoionized regions from kinematic studies.

Models of ionization fronts were generated by Mallik (1977) and it was shown that the temperature near the front can reach high values, resulting in an enhancement of the collisionally excited lines when compared to less temperature-sensitive hydrogen recombination lines. The signature of shock in an ionized gas is supposed to be a combination of a hot collisionally ionized region, with high values of [OIII] 4363/[OIII] (4959+5007) and a low excitation photoionized recombination region characterized by strong [OI] and [SII] lines (McKee, 1987). The shock emission spectra modelled by Shull et al

(as referred to in McKee, 1987) shows that the ratio [OIII] (4959+5007)/Hβ peaks (324) at a shock velocity of 130 km/s whereas the ratio [OI] 6300/Hβ and [SII]/Hβ peak (685 & 1200 respectively) at 30 km/s. Therefore by measuring the abundances of these ratios it should be possible to say whether the gas is collisionally ionized or photoionized.

The velocity (actual) around the bar ionization front is inferred to be more than 100 km/s from our observations (Table 4.3) considering that the front is making an angle nearly 85° with the line of sight.

On the basis of this we suggest that the O^{++} could have been produced by shock ionization, atleast, in part.

A schematic model for the Orion nebula

Based on the foregoing discussion of the results of the velocity field obtained by us and the other results, we present a schematic model for the structure of the Orion nebula shown in Fig. 4.16.

4.7 Turbulence

The third aspect of our studies on the velocity field structure in Orion involves charecterization of turbulent motions. As has been mentioned earlier, the presence of random fluctuations in radial velocities and the abnormal widths

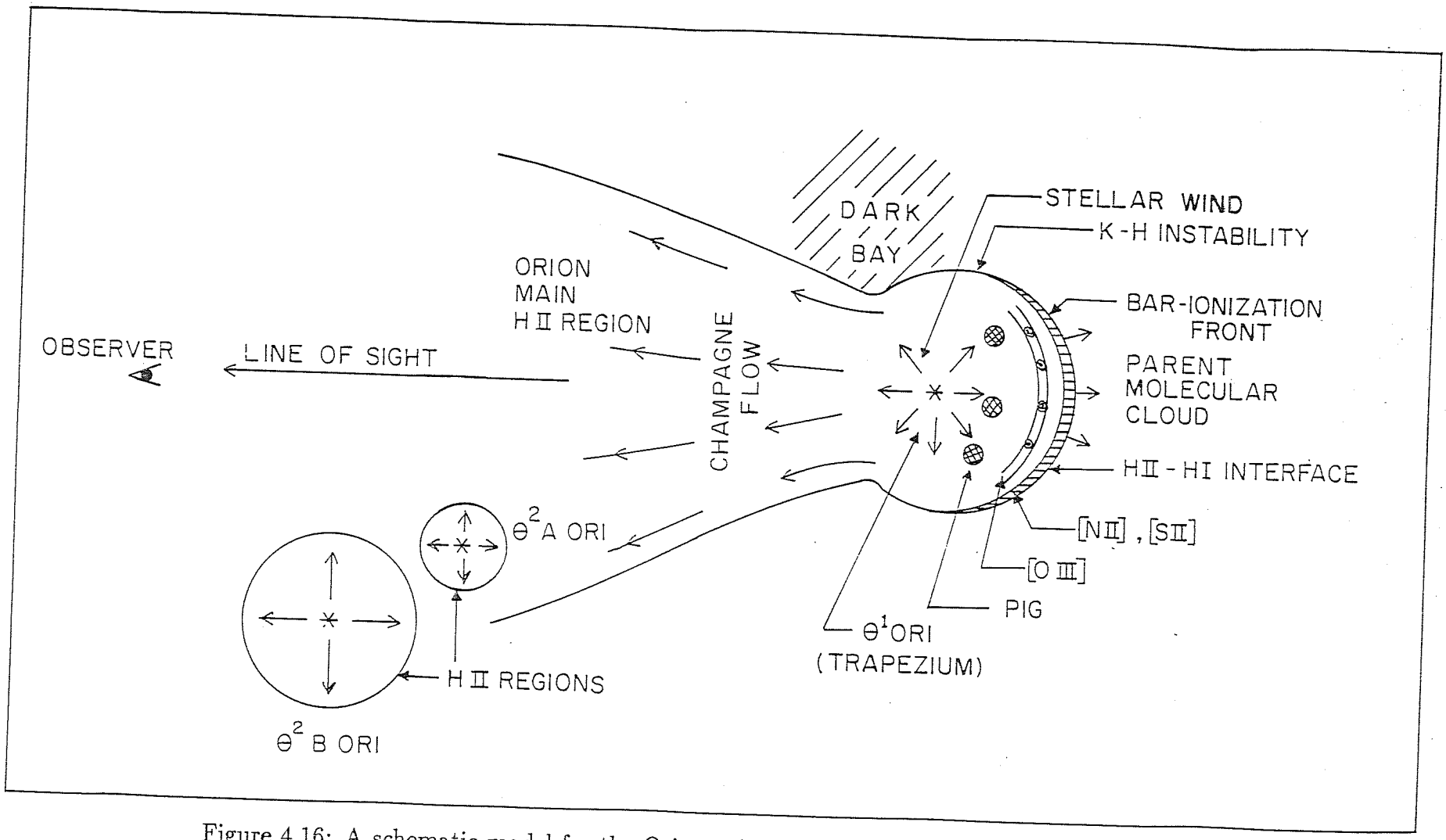

Figure 4.16: A schematic model for the Orion nebula based on the velocity field structure.

of emission lines has been established in the literature. The random motions in the fluid actually characterize the statistical order in the flow. Therefore, in order to study the random components we have made a statistical analysis from the large number of data points. Our study includes the analyses of the following: (i) Distribution of relative velocities and (ii)two point correlation function such as the Structure function.

4.7.1 Distribution of radial velocities

Turbulence being a stationary random phenomena, the distribution of radial velocity components, corrected for systematic flows, is assumed to follow a gaussian. In our data, we do not get absolute values of radial velocities but only the relative values. However, this would not matter as it would only change the 'dc' component. Therefore, histograms of relative radial velocities (uncorrected for systematic flows) in a window size of 4 arc sec against the number of points are generated and are shown in Figs. 4.17, 4.18 for the two components. One can see that the distribution follows fairly well a gaussian in the case of both the components. This probably shows that the random component of the radial velocities follows a gaussian distribution as assumed in the Kolmogorov theory. Our results are in corroboration with those of Castañeda's (1988). Since the distribution shows a gaussian nature even without accounting for the systematic mass flow, we may conclude that the effect of the latter is not very significant, atleast, in the present case.

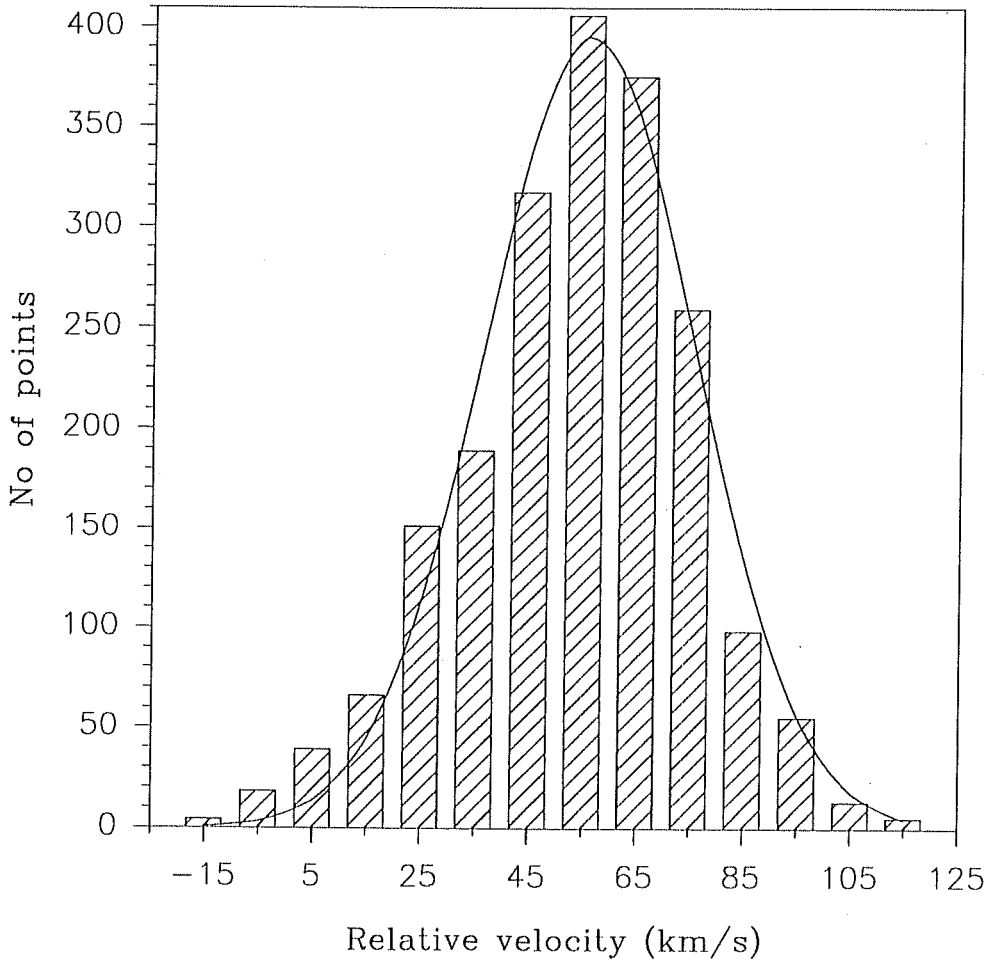

Figure 4.17: Histogram showing the velocity distribution for narrow component over the entire region of observations on Orion. The window size is 4 arc sec.

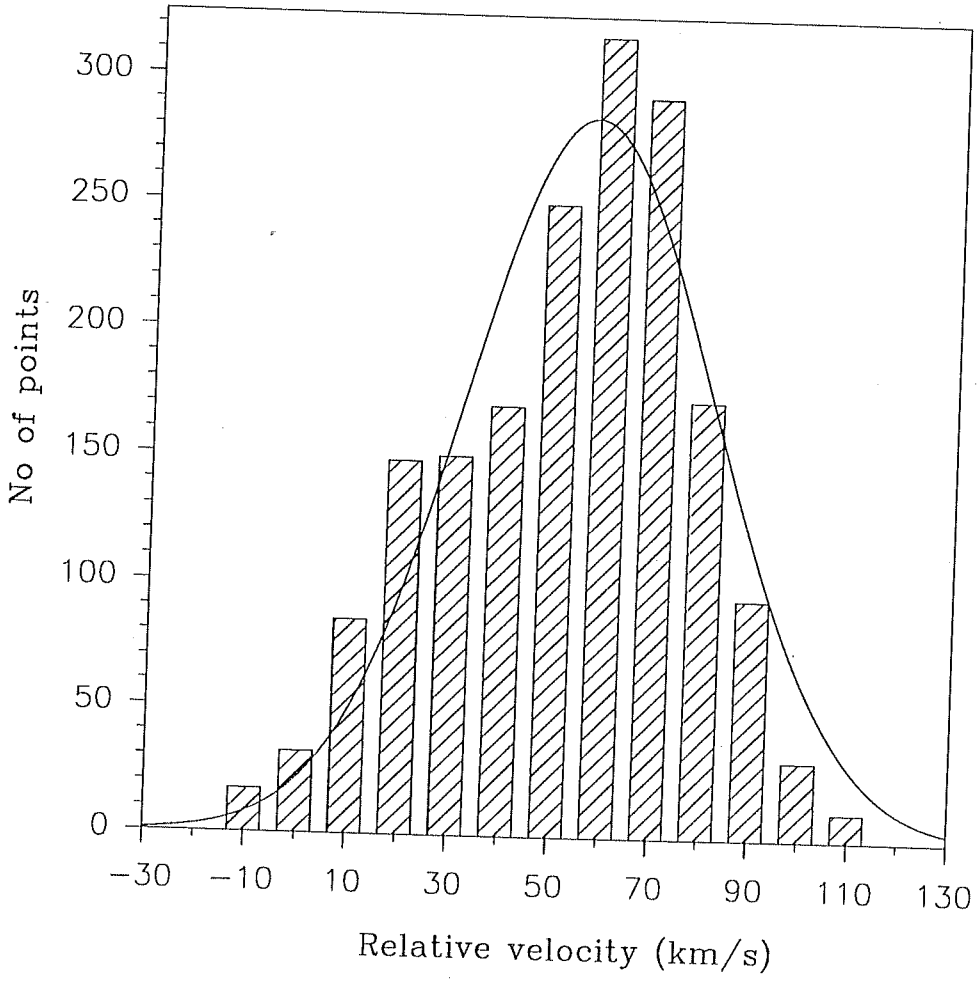

Figure 4.18: Histogram showing the velocity distribution for broad component over the entire region of observations on Orion. The window size is 4 arc sec.

4.7.2 Structure function

The averages and correlations of different physical quantities give a better way of understanding the behaviour of the fluid pattern (Scalo, 1984). The structure function is defined in order to make the statistical studies under the assumptions that the fluid is (i) isotropic, (ii) homogeneous and (iii) incompressible i.e., the density is constant (Kaplan, 1966) and free from any discontinuities like shock fronts etc. It is given by,

$$B(r) = < |v(r') - v(r'')|^2 >$$

where $r = r' - r''$ is the scale under investigation for velocity correlation and $v(r')$ and $v(r'')$ are the measured radial velocities at the points r' and r'', . This method was first used by von Hoerner (1951) and later, applied by Courtes(1955), Munch (1958), Louise and Monnet (1970), Scalo (1984), Roy and Joncas (1985), and very recently by Castañeda (1988) and O'Dell et al (1993). It was pointed out by Scalo (1984) that the structure function was a more appropriate method of analyzing the velocity fluctuations in HII regions, since it can characterize the correlation even in the presence of large scale spatial gradients. Since the calculation of the structure function involves the difference of velocity at two points, any number of points can be used to evaluate the function at a given distance which offers greater statistical accuracy. Its large absolute value makes it less sensitive to instrumental dispersion corrections (Castañeda, 1988). According to the standard model of Kolmogorov, $B(r) \propto r^{2/3}$. Therefore, the study of turbulence in gaseous

nebulae is reduced to the study of spatial fluctuations in the mean radial velocity along the line-of-sight. The structure function was computed by selecting all the possible combinations of pairs of points for the different sample sizes: $30'', 50'', 120'', 140'', 160''$. The minimum scale size was 4 arc sec as permitted by our spatial resolution. The structure function was evaluated in certain regions of interest which are discussed here.

Around θ^1 C Ori

The structure function was first evaluated in about 2 arc min area around θ^1 C Ori. Since the region selected is small, the conditions of the fluid being homogeneous and isotropic are likely to be satisfied as required by the Kolmogorov's theory. Any discontinuities and large scale gradients (such as that due to champagne flow) in velocities are subtracted from the radial velocities. A least square fit for the function representing a power law $B(r) = cr^n$ gives the value of the exponent $n = 0.998$ with correlation coefficient $=$ 0.978 for the first (narrow) velocity component (Fig. 4.19), for scale size of upto $100''$. The second (broad) velocity component also showed a similar behavior with $n = 1.23$ and correlation coefficient $=0.97$ (Fig. 4.20), for scale size of upto $100''$. Thus, the slope is found to be much larger than Kolmogorov's predictions. Around 120 arc sec from the Trapezium stars there is a sudden fall in the structure function. This hook is observed in all the earlier studies made on the nebulae. It seems to be the effect of the decrease in the number of points at larger separation and hence could be an

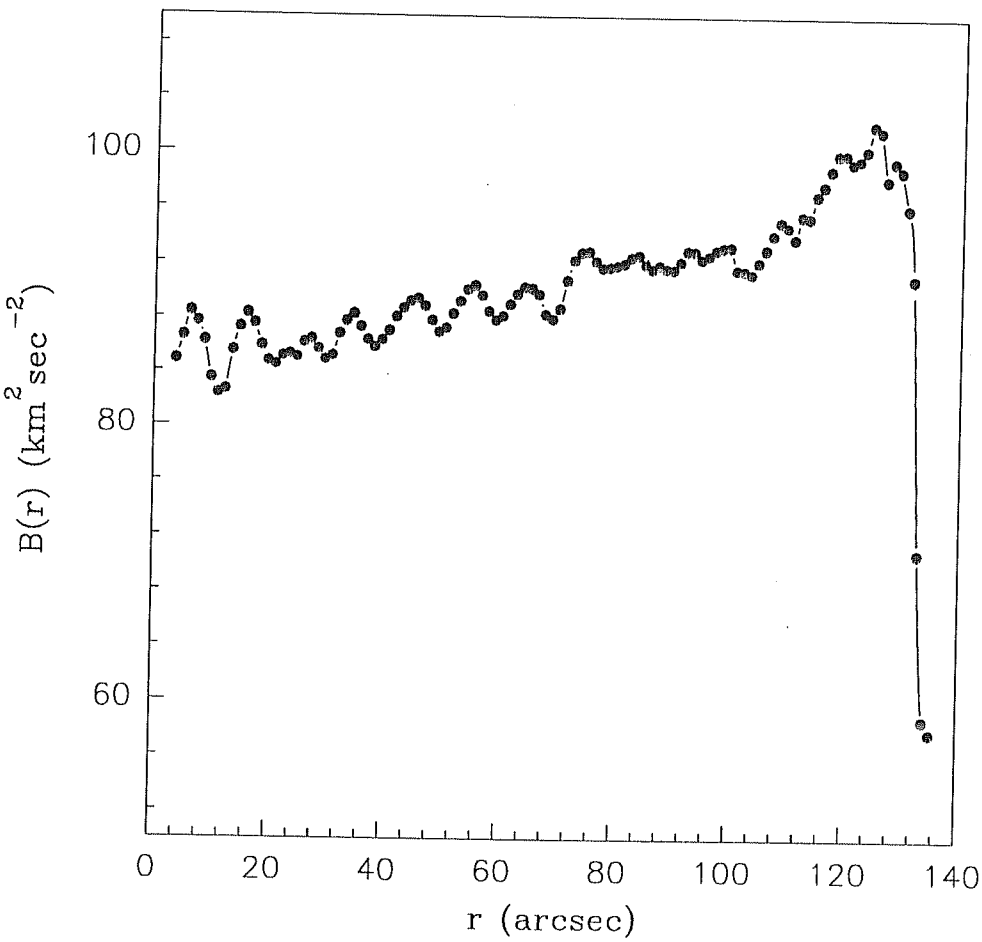

Figure 4.19: Structure function around 2 arc min of θ^1 C Ori for narrow component. The standard deviation in each data point corresponds to $\sim \pm 12$ km/s.

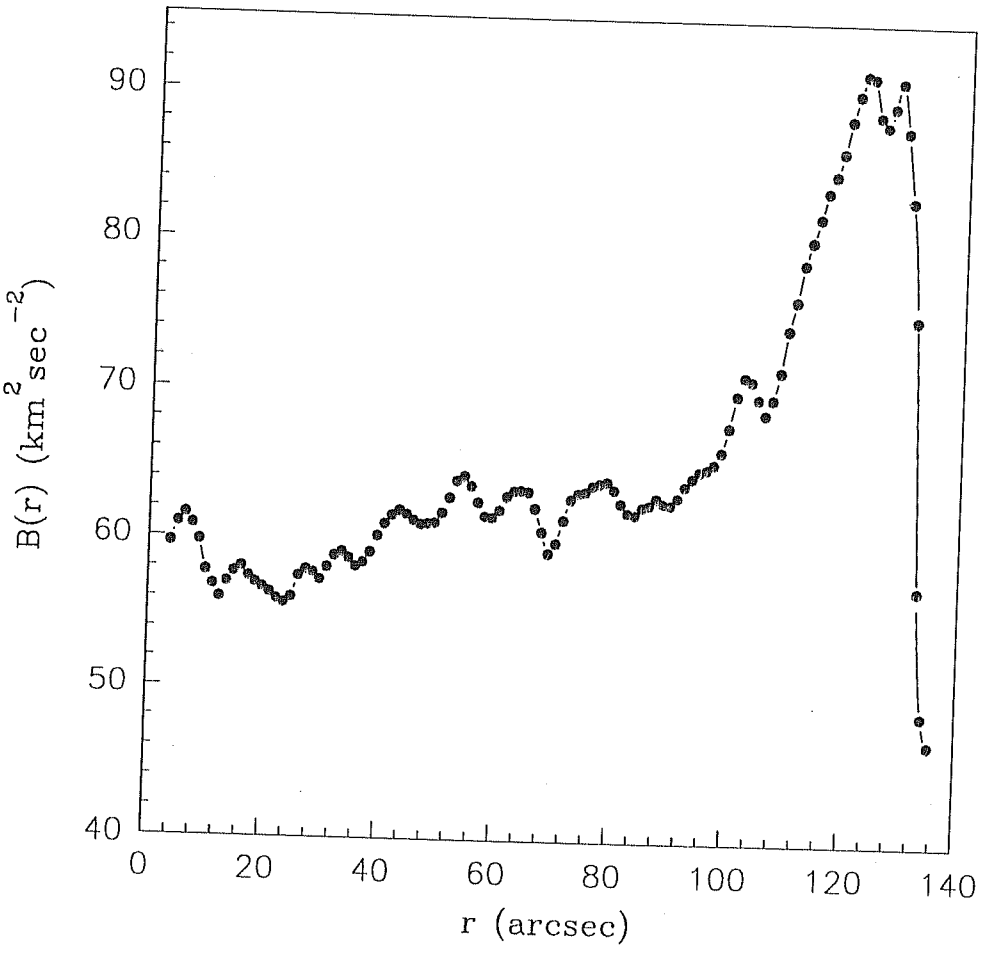

Figure 4.20: Structure function around 2 arc min of θ^1 C Ori for broad component. The standard deviation in each data point corresponds to $\sim \pm 12$ km/s.

artifact.

Around θ^2 A Ori

Structure function was computed for a region of about 120″ around $\theta^2 A$ Ori. Figs. 4.21 & 4.22 show the results obtained for the two components of the velocity field. One can find that there is an irregular behaviour for both the components. Earlier studies of Castañeda (1988) made around this region also showed a similar behavior. However, our data, even though lacks higher spatial resolution, are much more extended and more in number than those of Castañeda's.

Discussion

The most striking difference between the results of Castañeda's (1988) and the present results is in the index. While Castañeda obtains an index which is in line with Kolmogorov's theory, we get an index close to 1, quite in disagreement with the theory. While Castañeda has a better spatial resolution (1″) than ours (4″), our data encompasses the regions around θ^1 C Ori and θ^2 A Ori in a more uniform manner with more number of points than in Casteñeda's work. Further, our data has a velocity resolution of 6 km/s and velocity accuracy of 2 km/s while Castañeda's data has a velocity resolution of $\sim$ 1 km/s. One notices also that Castañeda proposes multiple slopes indicating that the energy is input at different spatial scales.

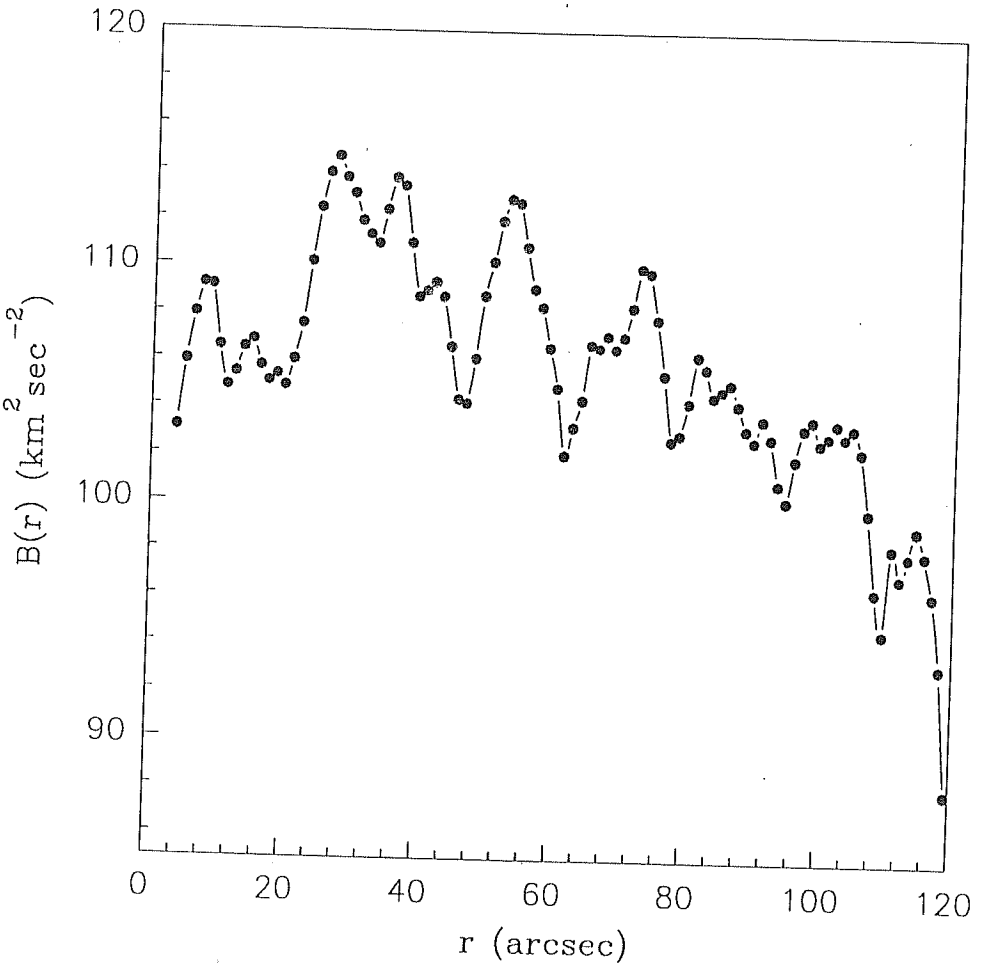

Figure 4.21: Structure function around 2 arc min of θ^2 A Ori for narrow component. The standard deviation in each data point corresponds to $\sim \pm 12$ km/s.

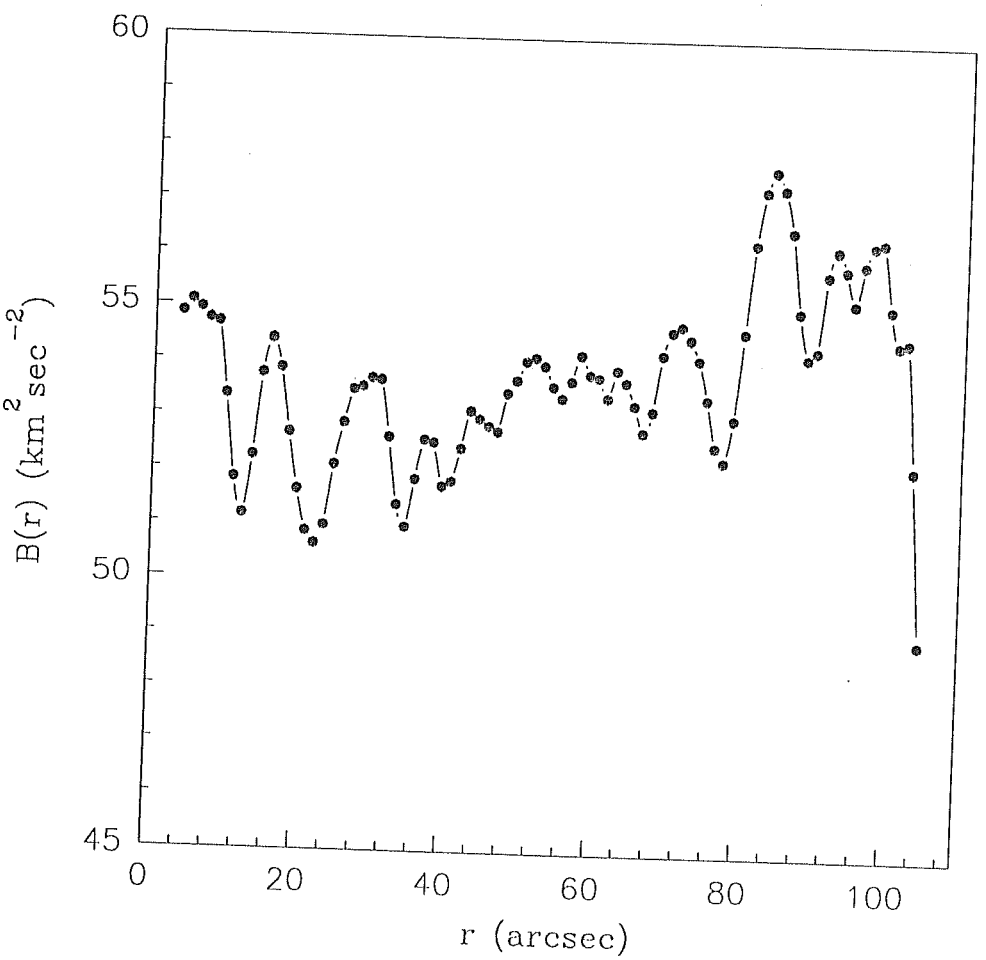

Figure 4.22: Structure function around 2 arc min of θ^2 A Ori for broad component. The standard deviation in each data point corresponds to $\sim \pm 12$ km/s.

In contrast our results lead to a single slope upto about 100″. The failure to satisfy Kolmogorov's law could probably be due to the departure from the physical conditions assumed in the theory of the turbulence. Since the conditions of isotropicity and homogeneity were approximately satisfied by considering a small region, it is possible that the condition of fluid incompressibility may not be satisfied. Similar results were reported by Joncas & Roy (1985) for the nebula $S142$ where it was proposed that compressibility in the fluid could act as a dissipation mechanism and could be responsible for the steeper slope than predicted by Kolmogorov's theory. It was suggested (Lighthill, 1955) that the influence of the compressibility could cause constant radiation of heat from the fluid in the form of sound waves which will subsequently transform into heat.

In order that the turbulence be maintained in the nebula, it requires a constant driving mechanism. It was pointed out that the Kelvin-Helmholtz (K-H) instabilities could be the energy source for turbulence in the HII regions (e.g., Roy and Joncas, 1985). Since the expansion of the ionized gas into the surrounding medium due to the champagne flow takes place with the development of a shock wave, there are possibilities of the growth of K-H instabilities in the Orion nebula as suggested by Blake (1972) and Norman et al (1982). When the shocked gas interacts with the interstellar medium, it gives rise to Rayleigh Taylor (R-T) and K-H instabilities. A R-T instability driven by buoyancy, develops over the front surface of a shock discontinuity whereas the K-H instability driven by shear, develops along the sides of a

shock discontinuity (Fig. 4.23) driven by the flow of the shocked medium over the surface. In a K-H instability, velocity shear is generated at the interface between two uniformly flowing layers of fluid (the expanding ionized matter in the shock and the compressed matter at the shock interface). The resultant mixing gives rise to vortices. The K-H waves arise towards the front and propagate back into the tail. After the waves have grown sufficiently, the shearing of the wave takes place which leads to vorticity. Intense small scale turbulence is generated between the vorticity leading to turbulent cascade process. In order to know whether K-H waves are a viable driving mechanism for turbulence, their growth time has to be found. The growth time of the waves in the absence of magnetic field in an incompressible fluid can be evaluated from the relation given by Blake (1972).

$$t = \left[\frac{k^2 \rho_1 \rho_2 v^2 \cos^2\theta \ \cos^2\phi}{(\rho_1 + \rho_2)^2} + \left(\frac{\rho_1 - \rho_2}{\rho_1 + \rho_2} \right) g k cos\,\theta \right]^{\frac{1}{2}} \qquad (4.6)$$

where ρ_1 and ρ_2 are, respectively, the densities of the intercloud medium and HII region; v is the velocity of the champagne flow; ϕ is the half-cone angle of the champagne flow and θ is the angle between the normal to the surface of the ionized gas flow and the normal to the cone axis; g is the acceleration of the flow and k is the wavenumber of the largest instability. Taking the densities to be 1250 cm^{-3} and 1600 cm $^{-3}$ for the inter-cloud and the ionized regions from Pogge et al (1992), and an average speed of 10 km/s from our observations and the maximum wavelength of 0.223 pc (from Fig. 4.19, the linear portion), $g = 8.65 \times 10^{-6}$ cm sec^{-2} and $\theta = 90°$, the growth time was evaluated. It was found that the first term in eqn. 4.6 becomes negligible

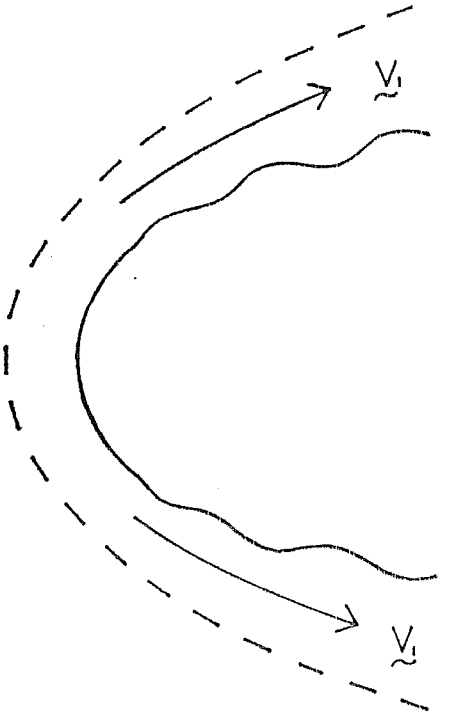

Figure 4.23: Kelvin-Helmholtz instability over the sides of a shock front. V_l denotes the flow speed (adapted from Blake, 1972).

compared to the second term and therefore is neglected. The time required for the growth of the instability was about 1.9×10^4 yrs which is less than the age of the nebula 10^6yr (Massey and Meaburn, 1993). Therefore it implies that the Orion nebula could be in a turbulent state in 1.9×10^4 yrs after the HII region has fully developed and the driving mechanism for turbulence could possibly be the K-H instability. However, it should be mentioned that the estimate was based on the assumption that the fluid is incompressible, while, in reality, it is compressible.

Chapter 5

VELOCITY FIELD STRUCTURE IN THE TRIFID NEBULA

5.1 Introduction

The Trifid nebula (NGC 6514, M20), said to be the photogenic example of a 'classical' galactic nebula, is situated in the Sagittarius arm (α (1950) = $17^h58^m9^s$ and δ (1950) = $23^o02'$). It measures about 15 arc min in diameter (Allen, 1973). It is supposed to be first observed by Le Gentil in 1747. It seemed to be a spherical nebula with a central exciting star in the photographs. Initially, due to the presence of three prominent dark lanes observed, the nebulosity was catalogued as four separate objects , the central bright spot (including the multiple stellar system) and the three luminuous lobes surrounding it (Sir William Herschel). Eventually, it was found to be

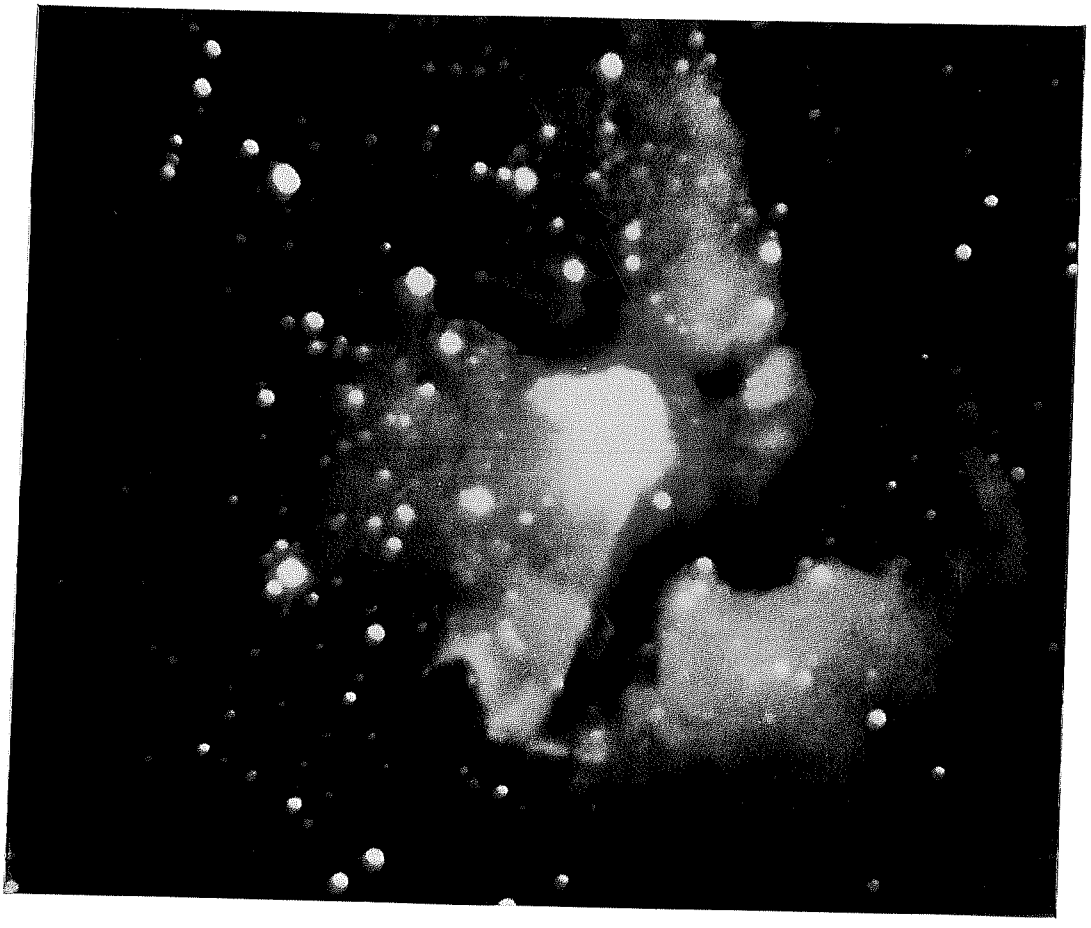

Figure 5.1: A photograph of Trifid nebula made by combining the blue, green, red, and near-infrared CCD images(Rudolph, 1988).

quiescent object. The symmetric flow was interpreted to be possibly due to the surrounding neutral shells with no open champagne flow situation as in the case of Orion nebula. The optical depth towards the central star in the nebula was found to be $\sim$ 1.5 at 4693 Å (Lynds et al, 1985) implying that all the extinction occurs within the nebula proper with the ratio of selective to total extinction $\sim$ 5.1 (similar to Orion) which is greater than the value found normally (3.0) in other nebulae. This shows that there is anomalous extinction in Trifid nebula.

5.3 Present studies

The velocity field across the Trifid nebula is studied by us over a much more extended region in order to have a more comprehensive picture than in the earlier observations and to have a comparative study with Orion nebula to put constraints on the models proposed for HII regions. An interferogram of Trifid nebula is obtained in [OIII] 5007 Å line with an integration time of 20 minutes. The field of view covered was 24 $'$. Each pixel corresponds to 4.6$''$ on the sky giving a spatial resolution of$\sim$ 9$''$. An optically contacted etalon having a FSR $\sim$ 1.25 Å (corresponds to 75 km/s at 5007 Å), with a velocity resolution of $\sim$ 7 km/s, was used. Our study provides the first wide field spectroscopic image of the nebula. The details of the observations and data analysis are discussed in chapter 3.

Line profiles were obtained for about 48 positions on the nebula. Firstly,

the proper centre of the interferogram is found. Since the signal to noise ratio is small in this case, photon counts were added in a sector of 10° and velocity values were obtained for about 48 positions. Eventhough the number of positions at which the velocity is obtained is not large, because of their symmetric distribution, reasonably good (though a little coarse) picture of the velocity flows can be constructed. The calibration interferogram was taken with cadmium source at 5086 Å. But it was found to be bad due to some sky contamination. Therefore, the radii of the standard fringes were obtained theoretically from equation (3.1) ,

$$R_s = f\sqrt{2(1 - n\lambda/2\mu t)} \tag{5.1}$$

The centre of the observed interferogram is matched to that of the theoretical one. The use of theoretical fringe radii will not contribute to any uncertainties in the relative radial velocities. Then the doppler shifted velocities were obtained as discussed in section 3.2

Each profile is found to be fitted well with a single gaussian with FWHM of about 20 ± 5 km/s. Fig. 5.2 shows a typical profile. An isovelocity contour map is generated from the data and is shown in Fig. 5.3. The main results obtained are discussed in the following section.

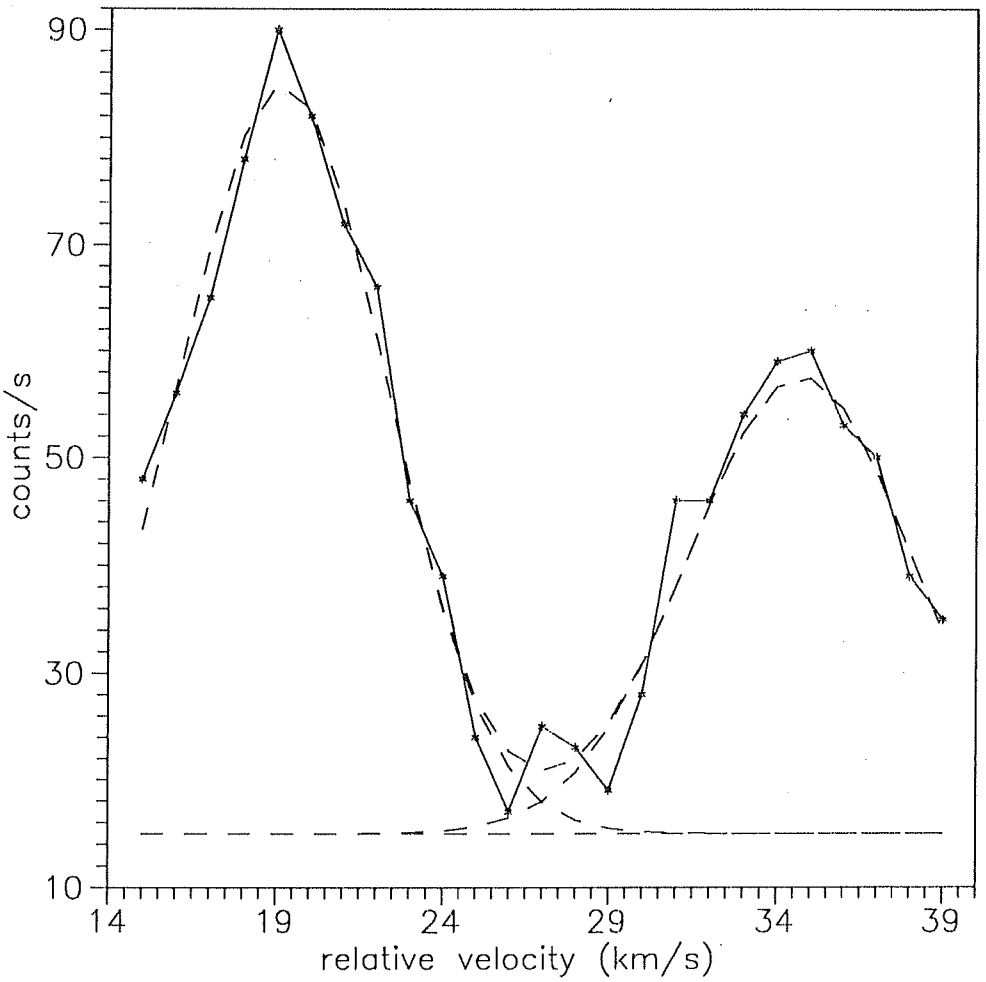

Figure 5.2: Typical line profile in [OIII] 5007 Å in Trifid nebula (solid line with asterisks). The dashed curve going through the asterisks is the composite gaussian fit with the individual gaussians shown by the small dashed curves. The dashed line at the bottom is the continuum level. The two peaks represent two adjacent fringes separated by a distance corresponding to 1 FSR.

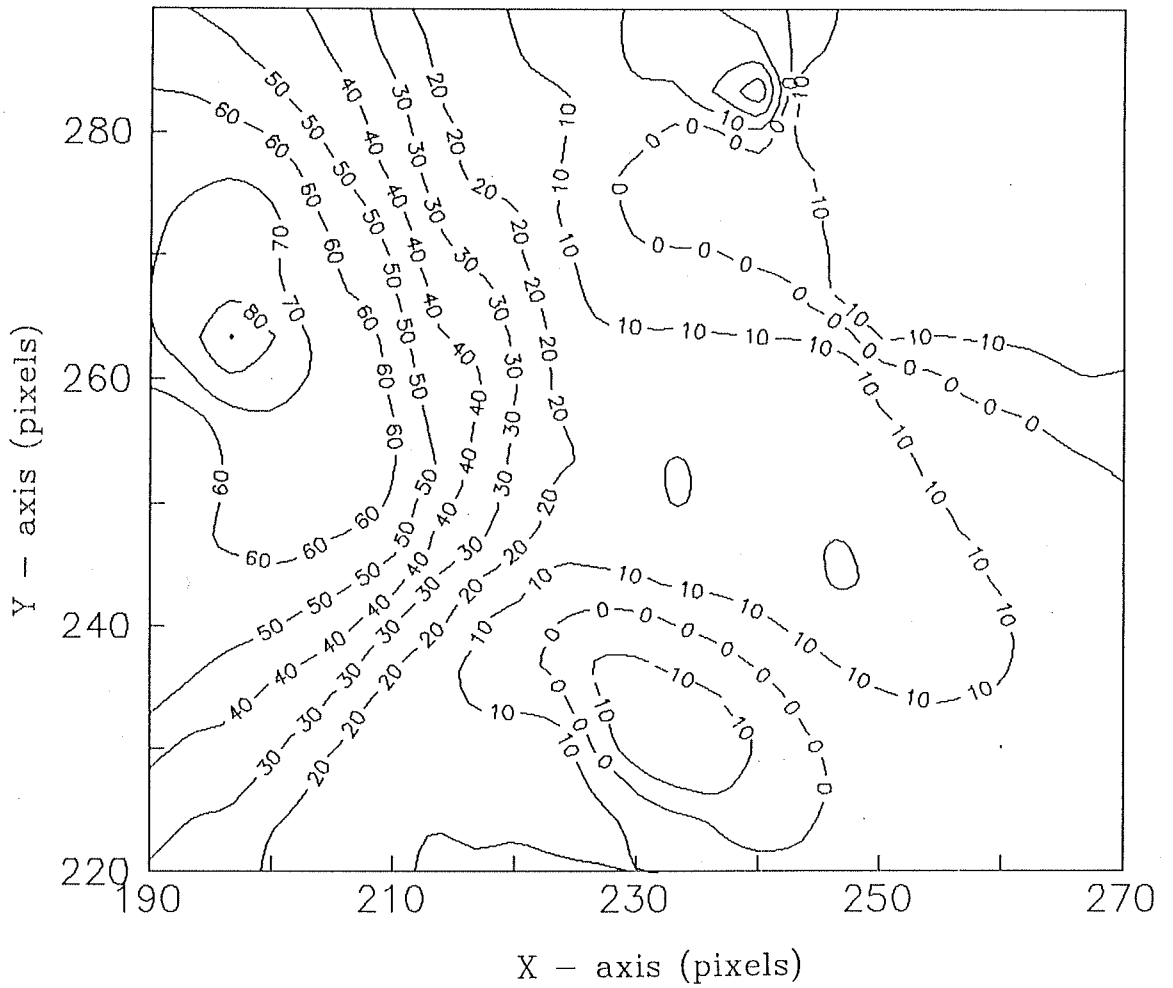

Figure 5.3: Iso-velocity contour map in [OIII] 5007 Å line in Trifid nebula. One pixel corresponds to about $\sim$ 4.6 $''$ on the sky.

5.4 General velocity field

5.4.1 About two arc minutes around the central star HD 164492

The radial velocities are found to be increasing from the centre rather symmetrically outwards implying a general expansion of HII region (Fig. 5.3). This indicates that there could possibly be a neutral shell surrounding the ionized region around the central star and therefore the flow is uniform in all directions. The star being a O type star, there should be associated stellar wind from the star and the shell could be driven by it. These observations are in corroboration with earlier observations of O'Dell et al (1987). There are no high velocity flows observed in this region indicating the absence of any jets or HH objects. The region seems to be quite quiescent.

Large scale red-shifted flow

There is a general red-shift in the radial velocities in the south west direction about 2 arc min from the central star HD 164492 with a velocity change of about 50 km/s (Fig. 5.3). Such a flow has so far not been reported, as the earlier kinematic observations were all confined to a small region surrounding the central star. This shows that the cloud is red-shifted along the line of sight, moving away from the observer. Since there are no other stellar sources in this region, the flow should possibly be associated with HD 164492. This

suggests that the red-shifted region represents a champagne-like flow going away from the observer.

5.4.2 Peculiar velocity flow

One more important finding of the present study is the discovery of a localized velocity flow with maximum relative velocities around 40 km/s from a position about 2.3 arc minutes south east of the star HD 164492. There seems to be an indication of splitting in the line profile at this position as shown in Fig. 5.4.

Studies in the past (Dyson, 1973a; Dyson, 1975) have established that there are neutral condensations or globules distributed across the nebula which are being ionized by the Lyman continuum photons from the hot stars called partially ionized globule (PIGs). Further the stellar wind when passing around these globules leads to the formation of bow shocks (Dyson, 1975). A bow shock feature, adjoining a condensation of bright emission, is seen in the photograph shown in Fig. 5.1. However, in the case of Trifid, we find these condensations to be, in general, quite irregular and very extended. Our velocity contour map shows a rather symmetric localized flow with a relatively red-shifted velocity of a maximum of 40 km/s around the condensation. On the other hand, the bow-shaped feature seems to have relatively blue-shifted velocities. The line splitting, if true, should then indicate the expansion of the partially ionized condensation. From our observations it appears that

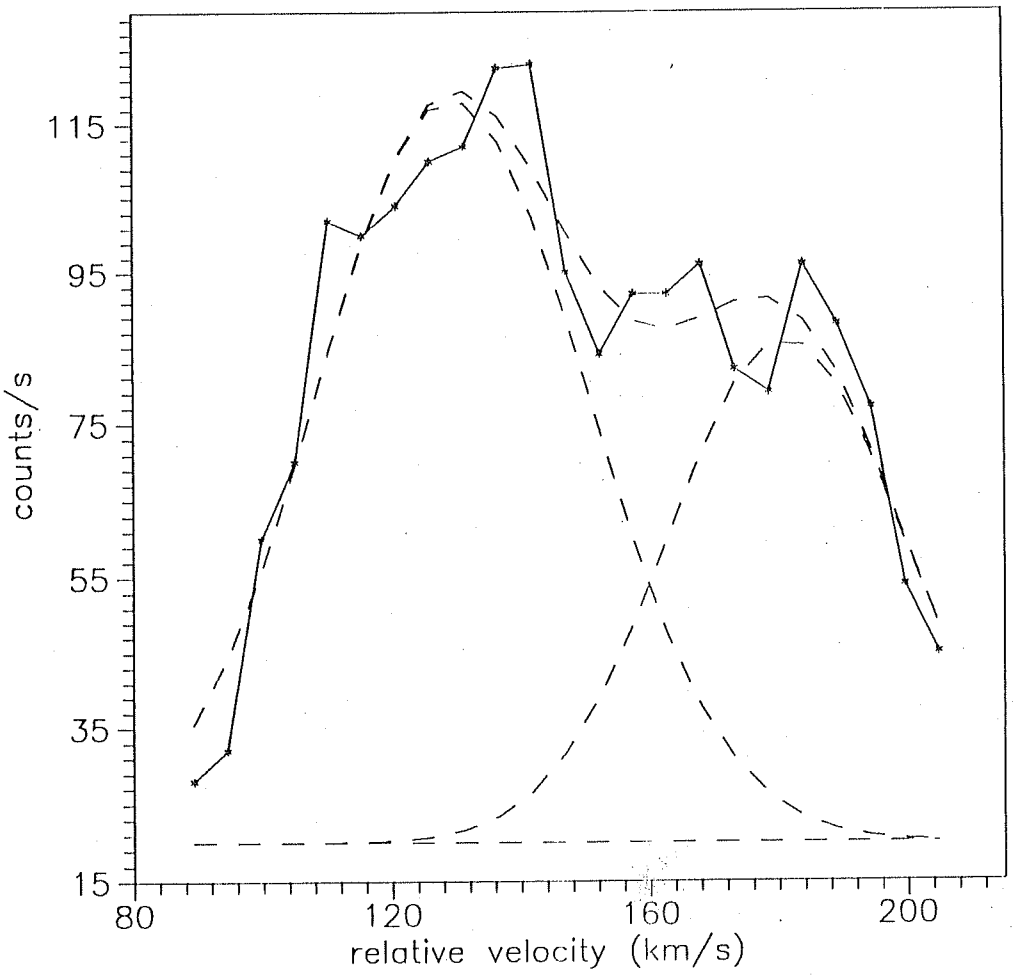

Figure 5.4: Profile across a feature 2.3 arc min SE of HD 164492 showing splitting in the line (solid line with asterisks). The dashed curve going through the asterisks is the composite gaussian fit with the individual gaussians shown by the small dashed curves. The dashed line at the bottom is the continuum level.

the HII region is surrounded by neutral clouds of complex structure.

5.5 Comparison of the velocity field structures of the Trifid and the Orion nebulae

A close scrutiny of the velocity fields of the Orion and the Trifid nebulae shows the following differences. (i) The line profiles in the case of Trifid nebula, in general, do not show two velocity components. This could probably be due to the fact that there is no interaction of the stellar winds giving rise to multiple velocity components along the line of sight as observed in the Orion nebula.

(ii) The general velocity flow pattern within 2 arc min of the central star in Trifid does not seem to follow the champagne flow proposed for the Orion HII region. In Orion nebula, the molecular cloud is situated behind the main ionizing stars (Trapezium), which obstructs the flow in that direction, but the Trifid nebula geometry does not show the presence of molecular cloud behind the star cluster HN40 and therefore the flow seems to be uniform in all directions. However, our observations on Trifid do show a red-shifted flow south west of the central star indicative of the champagne flow partly masked by the dust lane.

Chapter 6

SUMMARY AND CONCLUSIONS

The present chapter gives the summary of the work done towards the thesis as presented in the foregoing chapters. At the end, we discuss some aspects on the work to be carried out in future.

The thesis basically comprises of two parts: I. Instrumentation II. Observations, results and discussion.

6.1 The Instrumentation

An imaging Fabry-Perot spectrometer (IFPS) is designed and constructed for the studies on kinematics of extended astronomical objects like HII regions, Planetary Nebulae and spiral galaxies. The IFPS employs a two dimensional imaging sensor called Imaging Photon Detector (IPD). This is the first time

that such a detector is being used in the spectroscopic studies of astronomical objects. Also, this is the only instrument of its kind developed in India for the purpose of astronomical spectroscopy and one of the few in the world over. The instrument is designed to be used on the 1.2m telescope at Gurushikhar, Mt.Abu and on the 2.3m telescope at Kavalur, in South India. Also, a smaller version is designed for use on Celestron- 14 inch telescope at Mt.Abu. Present studies are made on the C-14 telescope with the smaller version. The IFPS is now being used successfully on the 2.3m telescope at Kavalur.

6.2 Observations and results on the kinematics of HII regions

6.2.1 Orion Nebula

The velocity field studies were made on the nearest HII region, the Orion Nebula, in [OIII] 5007 Å line. Line profiles were generated for about 2000 positions in a region $10.5' \times 10.5'$ on the nebula. Three type of studies were made on the data obtained: (i)general velocity flow (ii) high velocity flow and (iii)random or turbulent motions.

General velocity flow

The velocity field structure in the [OIII] 5007 Å line is obtained across different features (viz. 'bar' ionization front, dark 'bay'). The profiles showed an asymmetric or broad-winged shape and could be resolved in general into two gaussian components: The main results obtained after the analysis of the emission line profiles were as follows. (i) a narrow component with FWHM of around 20± 3 km/sec and (ii) a broad component with FWHM of around 50± 3 km/sec The two components could be interpreted as follows: The ionized gas from behind the trapezium is obstructed from flowing towards the molecular cloud and therefore the flow is directed towards the core region resulting in the interaction with the gas and neutral condensations present there which could give rise to secondary flows. These results are in general agreement with those of earlier results where line splitting (Wilson et al, 1959; Deharvang, 1979; Casteńada (1988)) in [OIII] 5007 Å line has been reported.

The iso-velocity contour map generated for both the components showed a decrease in the relative radial velocities from the Trapezium stars and are found to be blue-shifted from the centre outwards. This is in agreement with the champagne flow model suggested for the Orion cloud, according to which the ionized material is rushing towards the observer due to the pressure gradient established at the HI-HII interface.

Model Profile

A model emission line profile is constructed assuming a champagne flow and compared with the observed profile. The method involves calculating integrated sum of the radiation emitted by ions moving with different velocities along the line of sight with the assumption that thermal motions, turbulent motions and gradients in the velocity are the main source of line broadening. Assuming a temperature of 10^{4° K, the thermal broadening (FWHM) for [OIII] 5007 Å line was $\sim$ 5.3 km/s. The line profile was generated for a position on the nebula approximately $2'$ away from θ^1 Ori. The field of view considered for generating the line profile is $4''$ (corresponding to 2 pixels on our detector) and a velocity gradient of 1.73 km/s/pc was also assumed (from theoretical work of Yorke, 1986). Using a turbulent velocity of 9 km/s we find a reasonably good agreement between the generated profile and the narrow component of the observed profile.

Dark bay

The radial velocity was found to be low with no high velocity flow regions indicating that there is obstructing material to the expanding gas in this region.

Regions of high velocity flow

There are certain high velocity flows (~50 km/s) superimposed on the main flow observed in the narrow component. These high velocity flows are found to be either in the ionized regions near the stellar sources or in the molecular cloud regions. The mechanism proposed to explain these flows are either radiation pressure driven stellar winds or jets generated during the formation phase of Young Stellar Objects. The velocity map is compared with the density, temperature and intensity maps at optical as well as other wavelength regions (Infrared and radio) in order to look for the complimentary features and establish some correspondence. Some of the positions in the molecular cloud region do not seem to match with any of the peculiar features discovered before (viz. knots, jets and Harbig-Haro objects). A possibility is that these could be due to the shock waves generated by embedded outflows from young stellar objects or by supernova explosions or alternatively, it can be explained as due to the interaction of the ionized gas expanding from adjacent partially ionized globules.

Orion bar ionization front

Velocity profile was generated for the first time across the Orion 'bar' ionization front. A comparison with density profile (due to Pogge et al,1992) was made and Rankine-Hugoniot jump condition of mass flow across isothermal

shock fronts is verified, according to which,

$$\rho_o v_o = \rho_1 v_1 \tag{6.1}$$

i.e., when velocity is high, density is low and vice versa. The high velocity flows are found only in certain clumps along the bar. This is in agreement with [OIII] map (Pogge et al, 1992) showing that the bar ionization front is found to be diffuse in [OIII] 5007 Å line in contrast to the sharp feature found in the bar in [NII], [SII] and [OII] lines. This is obvious from the fact that the doubly ionized oxygen arises in fully ionized zone (Ionization potential = 35.11 eV) whereas the singly ionized species, being sensitive to the sudden changes in the ionization, occur at the HI-HII interface.

Ionization mechanism

The actual velocity obtained by us around the bar ionization front is estimated to be more than 100 km/sec, indicating that O^{++} is produced by shock ionization (at least in part).

Turbulence

In order to study the random components in the flow, a statistical analysis is made from the large number of data points. A correlation function called structure function B(r) is used for the study of the fluctuations in the velocities. The standard Kolmogorov's law states that $B(r) \propto r^{2/3}$. But our

analysis showed that the structure function $B(r) \propto r$; for a region about 100 arc seconds around θ^1 C Ori for both the narrow and the broad components. Thus, there is a deviation from the standard model of Kolmogorov. We interpret that this deviation is caused due to the presence of compressibily in the fluid (i.e., violation of one of the assumptions in Kolmogorov's model). The champagne flow of the material due to the expansion of the HII region indicates the possibility of the development of the Kelvin-Helmholtz instabilities (Blake 1972; Norman et al, 1982) in the cloud. The growth time of Kelvin-Helmholtz instabilities is found to be 1.9×10^4 yrs which is found to be less than the estimated age of the nebula ($\sim 10^6$ yrs). From this, we infer that Kelvin-Helmholtz instabilities could be the driving mechanism for turbulence in the Orion nebula.

The structure function around θ^2 Ori is found to be irregular in the case of narrow as well as broad components.

6.2.2 Trifid nebula

Velocity field studies were made for about 48 positions on the nebula in [OIII] 5007 Å line. The isovelocity map showed a picture of general expansion of the nebula in a region 2 arc minutes around HD 164492 with no high velocity flows. This indicates symmetric flow in velocities with no density gradients in this region as was observed in the case of Orion nebula. A general red-shift in the radial velocities is observed in the south west direction with a velocity

change of 50 km/s. This indicates that the cloud is moving away from the observer. It is proposed that the red-shift corresponds to a champagne flow partly obscured by dust lanes. There is a symmetric localised flow with a red-shift velocity of 40 km/s observed about 2.3 arc minutes southwest of the central hot star HD 164492 corresponding to a bow shock feature adjoining a condensation. This could be explained in terms of Dyson's model (Dyson, 1975) where the ionized gas from the surface of a globule interacts with the stellar wind from the hot star resulting in the formation of bow shock. There is also a splitting in the line profile indicating the expansion of the partially ionized condensation.

6.3 Scope for future work

There are now high resolution images obtained by Hubble space telescope providing us with all finer details of the Orion nebula. Study of the velocity field structure across these features is required in order to understand the physical processes responsible for such structures. Such a study is required especially in lines arising from low-excitation ions, like [SII], [NII] and the neutral species such as [OI]. Therefore, we plan to study the kinematics of not only the Orion but also that of other diffuse nebulae, viz. Rosette, Lagoon etc. Further, in the case of Trifid, only a single interferogram was obtained, therefore a complete velocity map is required to be generated by scanning the etalon in one FSR and generating the velocity profile at each pixel position.

Apart from studies on the velocity field in the shocked regions, HH objects and neutral condensations, we plan to study the velocity field around the photodissociation regions (PDRs) using appropriate emission lines (eg., [OI] 6300 Å). This will help in understanding of the processes involved in the interaction of the ionized gas with the molecular cloud region.

REFERENCES

Abt, H.,1983 (as quoted in Lynds et al, 1985).

Allen, C.W.,1973, Astrophysical Quantities, Athlone Press, London.

Aitken, D.K., Roche, P.F., Spenser, P.M., & Jones, B., 1979, A&A, **76**, 60.

Anandarao, B.G., & Suhasini, S. Rao , 1985, Bull. Astron. Soc. India, **14**, 25.

Atherton P.D., 1981, Opt. Engg., **20**, 806.

Atherton P.D., Reay, N.K., & Hicks, T.R., 1981, MNRAS, **200**, 806.

Atherton P.D., Taylor, K., Pike, C.D., Harmer, C.F.W., Parker, N.M., & Hook, R.N., 1982, MNRAS, **201**, 661.

Banerjee, D.P.K., 1990, Ph.D thesis, Gujarat University, India.

Baldwin, J.A., Phillips, M.M., & Terlevich, R., 1981, PASP,**93**, 5.

Balick, B., Gammon, R.H., & Hjellming, R.M., 1974, PASP, **86**, 616.

Balick, B., Gull, T.R., & Smith, M.G., 1980, PASP, **92**, 22.

Bally, J., Langer, W. D., Wilson, R. W., Stark, A.A., & Pound, M.W., 1991, in 'Fragmentation of Molecular clouds and star formation', eds. E. Falgarone et al, p. 11.

Barker, T., 1984, ApJ, **284**, 589.

Becklin, E.E, Beckwith, S., Gatlay, I., Mathews, K., Neugebauer, G., Sarazin, C.& Werner, M.W., 1976, ApJ, **207**, 770.

Beckwith, S., Neugebauer, G., & Becklin, E.E., 1978, ApJ, **223**, 464.

Bertout, C., & Yorke, H.W., 1978, in 'Protostars and Planets', U. Arizona Press, Tucson, p.648.

Blake, G.M., 1972, MNRAS, **156**, 67.

Bland, J., & Tully, R.B., 1989, AJ, **98**, 723.

Blitz, L., & Shu, F.H., 1980, ApJ, **238**, 148.

Bohlin, R.C.,& Savage, B.D., 1981, ApJ, **249**,109.

Boksenberg, A., 1972, 'Auxilliary Instrumentation for Large Telescopes', Proceedings of CERN conference, Geneva, p. 205.

Born, H., & Wolf, E., 1959, 'Principles of Optics', Pergamon Press, New York.

Boulesteix, J., Georgelin, Y.P., Marcelin, M., & Monnet, G., 1983, Proceedings of the SPIE conference, Instrumentation in Astronomy, Vol.445, p.37.

Breger, M., Gehrz,R.D., & Hackwell, J.A., 1981, ApJ, **248**, 963.

Bregman, L.J. Allamandola, Tielens, A.G.G.M., Geballe, T.R., & Witteborn, F.C., 1989, ApJ, **344**, 791

Buisson, H., Fabry, C., & Bourget, H., 1914, ApJ, **40**,241.

Buscomb,W., 1963, Mt. Stromlo Mimeographs, No.7.

Campbell, W. W., & Moore J. H., 1918, Pub. Lick. Obs, vol.13.

Canto, J., Goudis, C., Johnson, P.G., & Meaburn, J. A&A, **85**, 128.

Castaneda, H.O., 1988, ApJS, **67**, 93.

Chaisson, E.J., Scientific American, 1978, **239**, 122.

Chandrasekhar, S., 1949, ApJ, **110**, 329.

Clayton, C. A., Ivchenko, V. N., Meaburn, J., & Walsh, J. R., 1985, MNRAS, **216**, 761.

Courtes, G., 1955, in 'Gas dynamics of cosmic clouds', eds. J. M. Burgers & H. C. van de Hulst, North Holland, Amsterdam, p.131.

Courtes, G., 1960, Ann.Astrophys, **23**, 115.

Deharveng, L., 1973, A&A, **29**, 341.

Dopita, M.A., Dyson, J.E., & Meaburn, J., 1974, Ap&SS., **28**, 61.

Dopita, M. A., Gibbons A. H., & Meaburn J., 1973, A&A, **22**, 33.

Dyson, J.E., 1968a, ApSS., **1**, 388.

Dyson, J.E., 1968b, ApSS.,**2**, 461.

Dyson, J.E., 1973, A&A, **23**, 381.

Dyson, J.E., 1975, ApSS, **35**, 299.

Elliot, K.H.& Meaburn, J., 1974, ApSS, **28**, 351.

Fabry, C., & Perot, A., 1899, Ann.Chem.Phys(7), **16**, 115.

Fazio, G.G., Kleinman, D.E., Noyes, R.W., Wright, E.L., Zeilik II, M., Low, F.J., 1974, ApJ, **192**, L23.

Fischel, D., & Feibelman ,W.A., 1973., ApJ, **180**, 801.

Foukal, P, 1969, ApSS., **4**, 127.

Fountain, W. F., Gary, G. A., & O'Dell, C. R., 1979, ApJ, **229**,971.

Gautier, T.N., III, Fink, U., Treffers, R.R. & Larson, H.P., 1976, ApJ, **207**, L129.

Geballe, T.R., Tielens, A.G.G.M., Allamandola, L.J., Moorhouse, A., &

Brand, P.W.J.L., 1989, ApJ, **341**, 278.

Genzel, R., & Stutzki, J., 1989, AARA, **27**, 41.

Goudis, G., Hippelein, H.H., Munch, G., 1983, A&A, **39**, 117.

Goudis, C., Hippelein, H.H., Meaburn, J., & Song Sathaporn, R., 1984, A&A, **137**, 275.

Hanel, A., 1987, A&A, **176**, 347.

Haro, G., 1952, ApJ, **115**, 572.

Haro, G., 1953, ApJ, **117**, 73.

Hayashi, M., Hasegawa, T., Gatley, I., Garden, R., & Kaifu, N., 1985, MNRAS, **215**, 315.

Herbig, G. H., 1948, Ph. D. Thesis, University of California.

Herbig, G. H.,1950, ApJ, **111**, 11.

Herbig, G. H.,1951, ApJ, **113**, 697.

Herbig, G. H.,1952, J. R. Astron. Soc. Can, **46**, 222.

Hernandez, G., 1986, 'Fabry-Perot Interferometers', Cambridge University Press, Cambridge.

Hester, J.J., et al., 1991, ApJ, **369**, L75.

Hippelein, H., & Munch, G., 1978, A&A, **68**, L7.

von Hoerner, S., 1951, Zs. Ap., **30**, 17.

Hollenbach, D. J., 1988, 'Infrared spectroscopy in astronomy'.

Hollenbach, D.J., & Shull, J.M., 1977, ApJ, **216**, 419.

Israel, F.P., 1978, A&A, **70**, 769.

Jacquinot, P., 1954, J.Opt.Soc.Am., **44**, 761.

Jenkins, C.R., 1987, MNRAS, **226**, 341.

Johnston, K.S., Palmer, P., Nilson, T.L., & Bieging, J.H., 1983, ApJ, **271**, L89.

Joncas, G. & Roy, J.-R., 1986, ApJ, **307**, 649.

Jones R.V. & Richards J.C.S., 1973, J. Phys. E. (Sci. Instrum.), **6**, 589.

Kahn, F.D., 1964, Trans. IAU.

Kahn, F.D., 1969, Physica, **41**, 172.

Kahn, J., 1977, ApJ, **216**, 713.

Kaler,J.B., 1967, ApJ, **148**, 925.

Kaplan, S.A., 1966, 'Interstellar Gas Dynamics', Pergamon, Oxford.

Kaplan, S.A., & Pikelner, S.B., 1970, 'The Interstellar Medium', Harvard University Press, Cambridge.

Kennicutt,R.C., & Kent,S.M., 1983, A.J., **88**, 1094.

Kitchin, C.R., 1991, 'Astrophysical Techniques', Adam Hilger, New York.

Kolmogorov, A.N, 1941, C.R Acad.sci.SSSR, **30**, 301.

Kristian, J. & Blouke, M., 1982, Scientific American, **247**, 48.

Kutner, M., & Thaddeus, P., 1971, ApJ, **168**, L67.

Kutner, M., Thaddeus, P., Jefferts, K.B., Penzias, A. A. & Wilson, R.W., 1971, ApJ, **164**, l49.

Kwan, J., & Scoville, N., 1976, ApJ, **210**, L39.

Lampton, M., 1981, Scientific American, **245**, No.5, 46 (MCP).

Lampton, M., & Carson, C. W., 1979, Rev. Sci. Instrum., **50**, 1093.

Larson, R.B., 1972, MNRAS, **157**, 121.

Larson, R.B., 1973, ARAA, **11**, 219.

Larson, R.B., 1981, MNRAS, **194**, 809.

Lighthill, M.J., 1955, in 'Gas dynamics of cosmic clouds', eds. Burgers J. M. & van de Hulst, H. C., North-Holland, Amsterdam, p.121.

Loren, B., Robert, 1979, ApJ, **234**, 1207.

Louise, R., & Monnet, G., 1970, A&A, **8**, 486.

Lynds, B.T., Blaise, J.C. & O'Neil,Jr. E.J., 1985, ApJ, **288**, 164.

Mackay, C.D., 1986, ARAA, **24**, 255.

Mallik, D.C.V., 1975, ApJ, **197**, 355.

Massey, R.M. & Meaburn J., 1993, MNRAS, **262**, 48p.

Mathews, W.G., & O'Dell, C.R., 1969, ARAA, **7**, 67.

Mathis, J.S., 1972, ApJ, **176**, 651.

Mckee, C.F, 1987, 'Spectroscopy of Astrophysical plasmas' Eds. Dalgarno, A., & Layzer, D., Cambridge University Press, Cambridge.

Meaburn, J., 1971, ApSS, **13**, 110.

Meaburn, J., 1976, 'Detection and spectrometry of faint light', D.Reidel, Dordrecht.

Meaburn, 1977, in 'Topics in Interstellar Matter', ed. H. van Woerden D. Reidel, Dordrecht, p. 81.

Meaburn, J., 1981, MNRAS, **196**, 19.

Meaburn, J., 1984, MNRAS, **211**, 521.

Monnet, G., 1971, A&A, **12**, 379.

Mufson, S. L., Fountain, W. F., Gary, G. A., Howard III, W. E., O'Dell, C. R., and Wolff, M. T., 1981, ApJ, **248**, 992.

Munch, G., 1958, Rev.Mod.Phys., **30**, no.3, 1035.

Munch. G., & Taylor, K., 1974, ApJ, **192**, L93.

Munch, G., & Hippelein, H., 1982, in 'Symposium on the Orion nebula to honour Henry Draper', eds. A.E. Glassgold, P.J. Huggins and E. L. Shuckin, Ann. NY Acad. Sci., **395**, p.170.

Norman, M.L., Smare, L., Winkler, K.-H. A., & Smith, D.H., 1982, A&A, **113**, 285.

O'Dell, C.R., 1986, ApJ, **304**, 767.

O'Dell, C.R. & Castaneda, H.O., 1987, ApJ, **317**, 686.

O'Dell, C.R., & Wen, Z., 1992, ApJ, **387**, 229.

O'Dell, C.R., Wen, Z., & Hu, X., 1993, ApJ, **408**.

O'Dell, C.R., Hubbard, W.B., & Peimbert, M., 1966, ApJ, **143**, 743.

O'Dell, C.R., Townsley, L.K & Castaneda, H.O., 1987, ApJ, **317**, 676.

Omodaka, T., Hayashi, M., Hasegawa T., & Gatley J., 1987, in 'Star forming regions', eds. M. Peimbert and J.Jugaku, D.Reidel, Dordrecht, p.150.

Osterbrock, D.E., 1974, 'Astrophysics of gaseous nebulae', Freeman, San Francisco.

Palmer, P., Zuckerman, B., Penfield, H., Lilley, A.E., & Mezger, P.G., 1967, Nature, **215**, 40.

Pallister, W.S., Perkins, H.G., Scarrott, S.M., Bingham R.G., & Pilkington, J.D.H., 1977, MNRAS, **178**, 93.

Pankonin, V., Walmsley, C.M., & Harwit, M., 1979, A&A, **75**, 34.

Peimbert, M., 1982, 'Symposium on the Orion nebula to honour Henry Draper', eds. A.E. Glassgold, P.J. Huggins and E. L. Shuckin, Ann. NY Acad. Sci., **395**.

Peimbert,M, & Torres-Peimbert, S., 1977, MNRAS, **197**, 217.

Pikel'ner, S.B., & Shain, G.A., 1954, Izv. Krymsk. Astrofiz. obs., **11**, 22.

Pogge, R.W., Owen, J.M. & Atwood, B., 1992, ApJ, **399**, 147.

Pottasch.S.R., 1969, in 'Interstellar Gas Dynamics', ed. H.J. Habing, **39**, 272.

Raju, K.P., Debi Prasad, C., Desai, J. N. & Mishra, L., 1993, ApSS, **204**, 205.

Roche, P.F., Aitken, D.K., & Smith, C.H., 1989, MNRAS, **236**, 485.

Roessler, F.L., 1974, in 'Methods of Experimental Physics', ed. N. Carleton, Academic press, Newyork., **12 A**, p.531.

Rosseland, 1929, Mon. Not. **89**, 49.

Roy, J.-R., & Joncas, G., 1985, ApJ, **288**, 142.

Rudolf, E.S., 1988, Sky & Telescope, , 144.

Scalo, J.M., 1984, ApJ, **277**, 577.

Schwartz, R.D., 1975, ApJ, **195**, 631.

Schwartz, R.D., 1983, ARAS, **21**, 209.

Schwartz, R.D., and Dopita, M.A., 1980, ApJ, **236**, 543.

Scoville, N.Z., Hall, D.N.B., Kleinmann, S.G., & Ridgway, S.T., 1982, ApJ, **253**, 136.

Sellgren, K., & Tokunaga, A.T., 1990, ApJ, **349**, 120.

Shull, J.M., & Mckee, C.F., 1979, ApJ, **227**, 131.

Shu, F.H., 1976, 'The Physical Universe, An Introduction to Astronomy', University Science Books, California, Color plate 6.

Smith, M.G., & Weedman, D.W., 1970, ApJ, **160**, 65.

Snow, T.P., & Morton, D.C., 1976, ApJS, **32**, 429.

Spitzer, L., 178, 'Physical Processes in the Interstellar Medium', Wiley, New York.

Sorrell, W.H., 1992, MNRAS, **255**, 594.

Stacey, G.J., Jaffe, D.T., Geis, N., Genzel, R., Harris, A.I., Pogtilsch, A., Stutzki, J. & Townes, C.H., 1993, ApJ, **404**, 219.

Sugitani, K., Fukui, Y., Ocawa, H. & Kawabata K., 1986, ApJ, **303**, 667.

Taylor, K., & Munch, G., 1978, A&A, **70**, 359.

Tenorio-Tagle, G., 1979. A&A, **71**, 59.

Tenorio-Tagle, G., 1982, 'Regions of Recent Star Formation', eds. R.S. Roger & P.E. Dewdney, D. Reidel, Dordrecht, p.1.

Thronson, H.A. et al, 1986, AJ, **91**, 1350.

Tidman, D.A., 1958, Phys. Rev., **111**, 1439.

Tsuchiya,Y., Inuzuka,E., Kurono,T., & Hosoda M., 1985, Advances in 'Electronics and Electron Physics', **64A**, 21.

Tully, R.B., 1974, ApJS, **27**, 415.

Vaughan, J.M., The Fabry-Perot Interferometer, Adam Hilger, 1989.

de Vaucouleurs, G., & Pence, W.D., 1980, ApJ, **242**, 18.

van der Werf, P.P., & Goss, W.M., 1989, A&A, **224**, 209.

Werner, M.W., Gatley, T., Harper, D.A., Becklin, E.E., Loewenstein, R.F., Telesco, C.M. & Thronson, H.A., 1976, ApJ, **420**, L04.

Wilson, O. C., Munch G., Flatter E. M., Coffen M. F., 1959, ApJS, **14**, 199.

Woodward, P.R., 1978, ARAA, **16**, 555.

Young, 1974, in 'Methods of Experimental Physics', ed. N. Carleton, Academic press, Newyork., **12 A**, p.531.

Yorke, H.W., 1985, in 'The Birth and Infancy of Stars', Les Houches Summer School, eds. A. Lucas et al, North-Holland, Amsterdam, p. 823.

Yorke, H.W., & Krungel, E., 1977, A&A, **54**, 183.

Yorke, H.W., Tenorio-Tagle, G., Bodenheimer, P., 1983, A&A, **127**, 313.

Zuckerman, B., 1973, ApJ, **183**, 863.